

Implantable Nanofluidic Membrane and Smart Electronic System for Drug Release Control

*Original*

Implantable Nanofluidic Membrane and Smart Electronic System for Drug Release Control / Silvestri, Antonia. - (2021 Jul 12), pp. 1-182.

*Availability:*

This version is available at: 11583/2918000 since: 2021-08-17T15:32:04Z

*Publisher:*

Politecnico di Torino

*Published*

DOI:

*Terms of use:*

Altro tipo di accesso

This article is made available under terms and conditions as specified in the corresponding bibliographic description in the repository

*Publisher copyright*

(Article begins on next page)



**ScuDo**  
Scuola di Dottorato ~ Doctoral School  
WHAT YOU ARE, TAKES YOU FAR



Doctoral Dissertation  
Doctoral Program in Electrical, Electronics and  
Communication Engineering (32<sup>nd</sup> Cycle)

# **Implantable Nanofluidic Membrane and Smart Electronic System for Drug Release Control**

By  
**Antonia Silvestri**

\* \* \* \* \*

## **Supervisors**

Prof. Danilo Demarchi, Supervisor  
Prof. Alessandro Grattoni, Co-Supervisor

## **Doctoral Examination Committee:**

Prof. Fiorella Altruda, Referee, Università di Torino  
Prof. Sabrina Conoci, Referee, Università di Messina  
Prof. Bruna Corradetti, Referee, Houston Methodist Research Institute  
Prof. Vito De Feo, Referee, University of Essex  
Prof. Guido Pagana, Referee, Istituto Superiore Mario Boella

Politecnico di Torino  
2021

---

# Declaration

I hereby declare that, the contents and organisation of this dissertation constitute my own original work and does not compromise in any way the rights of third parties, including those relating to the security of personal data.

.....  
Antonia Silvestri  
Turin, 2021

\* This dissertation is presented in partial fulfilment of the requirements for Ph.D. degree in the Graduate School of Politecnico di Torino (ScuDo).

---

---

*These dissertation, research and study are dedicated  
to my beloved family and friends.*

---

---

# Acknowledgment

It has been a long and amazing journey, and I would like to express my appreciation to all the people that shared part of this path with me. It would be impossible to mention everybody in this section, therefore I'll give space to some of the main contributors to my success: to all the others, your contribution was equally important, and I will have the chance to express my genuine gratitude.

I would like to sincerely thank Professor Danilo Demarchi, for giving me the possibility to do this remarkable experience. As my supervisor and scientific mentor, he was always available to show me the best path to improve my academic knowledge: his support was vital to the pursuit of my goals.

I would like to express my gratitude to Professor Alessandro Grattoni: the chance to work in his highly talented laboratory and be part of a team with high-quality researchers at the Methodist Hospital Research Institute (HMRI) has been an invaluable step in my professional career. His supervision inspired me to continuously improve myself, without losing focus on my daily work.

I would also like to thank Dr. Paolo Motto Ros for the incredible patience he demonstrated since the first day we worked together. He has always been open to listen to new ideas and suggestions, leading me toward good decisions. Similarly goes for Professor Giancarlo Canavese for his kind availability, patience, and constructive feedback on my latest academic work. I would then like to appreciate the contribution of Professor Xuewu Liu for instruments training, and together with Dr. Daniel Fine, for the collaboration to fabricate the nanochannel membranes. My gratitude also goes to Giacomo Bruno, Antons Sizovs, Nico Di Trani, and Corrine Chua, for the considerable teamwork and support on this project, as well as all the members of the MiNES group and Grattoni's laboratory.

I would like to acknowledge the support provided by Professor Sabrina Grassini, who gave me a place in her electrochemical laboratory and, together with

Professor Maurizio Martina, for being exceptional advisors for the IEEE groups; Professor Gianluca Piccini and Professor Mariagrazia Graziano for their advices and for being a constant source of inspiration in the field of research; Dr. Jianhua (James) Gu and Dr. Huie Wang for the incredible patience demonstrated during the SEM, EDX, and AFM microscopy training, and all the fruitful discussion about scientific phenomena and their implications; Dr. Enrica De Rosa and Dr. Sara De Nizzero for the instruments training; Prof. Chang Long, for the inspired mentoring and FIB-SEM instrumentation training; and Dr. Donald, for the access at the Microelectronics Research Center and the JJ. Pickle Research Center.

Furthermore, in these challenging years, several are the people that I found by my side: Beatrice Miccoli, an esteemed colleague, researcher, and great supporter; Abduwali Tohti, with whom I shared great discussions about science and the meaning of life; Bruna Corradetti for the constant inspiration she gave me by being one of the best examples of a great and tireless scientist. To all of them, I feel the need to express my sincere gratitude.

Moreover, my dear acknowledgement to Yuri, Simone Carmine, Maurizio, Giovanni, Leonardo, Vincenzo, Umberto, members of the IEEE Student Branch committee, and to Rossana, Leila, Kristjane, and Nancy, members of the Women In Engineering IEEE Student Branch committee of Politecnico di Torino, with whom I shared and diffuse the STEM culture.

To my friends Rita, Mahi, Vittoria, Gianluca, Marjorie, Tugba, Livio, Luca, and Simo for supporting me during the bad and the good times. My deepest gratitude goes to Barbara M., for giving me the support and the strength to achieve my goal.

Last but not least, I feel the need to express a heartfelt thank you to Maria and Benito, my beloved parents, who have supported me along this journey, and to Marinella, Valentina, Francesco, and City S., always standing beside me in the most important moments.

Sincerely, thanks to all.

---

# Abstract

The work presented in this dissertation is the result of the theoretical and experimental research conducted in the field of nanomedicine and personalized health care for the jointed academic program between the Politecnico di Torino, Turin, Italy, and the Methodist Hospital Research Institute (HMRI), Houston, Texas.

The dissertation is focused on the design and development of a silicon nanofluidic membrane for ultra-low power electrostatic control of drugs and analyte elution remotely controllable by wireless communication in the field of the Nanomedicine and Personalized Health-Care. More specifically, the study is focused on tightly controlling the diffusion regimes of charged molecules through nanochannels at the nanoscale by using an electrostatic electric field. Taking advantages from their nanometric dimension, therapeutics flowing through nanochannels can be manipulated by acting on some aspects of the drug delivery system, such as dimensions and polarity of the nanochannels, and the ionic strength of the solution, among others. The significant nanotechnological advantage of the fluidic membrane resides in the independent linear flow of the drug from the concentration gradient originated between the reservoir hosting the molecules and the external regions. In this work, the development of the amorphous silicon carbide (a-SiC) coated solid-state nanofluidic membrane that achieved reproducible and tunable control of the drug release via electrostatic gating was discussed. Firstly, the nanofluidic design and fabrication were illustrated and investigated utilizing visual examination, such as Focus Ion Beam Microscopy, and Scanning Electron Microscopy Investigation, and mechanical investigation, such as nitrogen gas test measurements. Then, a study for the evaluation of the corrosion rate of the a-SiC membrane in the simulated implantation condition to simulate body-fluid

interaction was discussed. Electrical performances were investigated with an electrochemical analysis using two different electrolyte solutions in various concentrations, i.e., potassium chloride (KCl) and phosphate buffer saline (PBS). Then, the modulation of the release rate of five medical relevant molecules are presented is reported. The results demonstrated that it is possible to effectively control the rate of the molecules release by the application of an electric field. Those results lead to the design of an electronic board that can remotely control the charged therapeutics via Bluetooth Low Energy. This new platform will enable the real-time remote control over released dosage of the therapeutics, leading to a new platform for personalized medicine.

Keywords: Drug Delivery Nanofluidic Membrane, Nano-Electrofluidics, Silicon Nanochannel Membrane, Remote Control for Personalized Medicine, Chronotherapy.



---

# Contents

Acknowledgment .....	iii
Abstract.....	v
Contents .....	vii
List of Figures .....	xi
List of Tables .....	xiv
1. Introduction.....	1
2. Nanotechnology, nanomedicine, personalized medicine, and controlled drug delivery system .....	6
Abstract.....	6
2.1 Introduction .....	7
2.2 Implantable Drug Delivery Systems .....	8
2.3 Constant release and controlled release implantable devices .....	9
2.4 Silicon Gated Nanochannel Membrane for Drug Delivery System .....	11
2.5 Transport Phenomena in Nanochannels .....	15
2.6 Concentration polarization phenomenon.....	20
3. Design and mechanical characterization of the nanofluidic membrane .....	23
Abstract.....	23
3.1 Introduction .....	24
3.1.1 Processes used to fabricate the nanofluidic membrane.....	26
3.1.2 Materials used to fabricate the nanofluidic membrane .....	38
3.2 Materials and Methods .....	41
3.2.1 Process fabrication steps of the nanofluidic membrane.....	41
3.2.2 Focused ion beam (FIB), scanning electron microscope (SEM) imaging, energy dispersive X-ray spectroscopy (EDX) and ellipsometry .....	48
3.2.3 The gas testing system .....	48
3.3 Results .....	49

3.3.1 Nanofluidic membrane .....	49
3.3.2 EDX, and Ellipsometry Measurements .....	51
3.4 Conclusion .....	52
4. In-Vitro Degradation Study .....	54
Abstract.....	54
4.1 Introduction .....	55
4.1.1 Scanning Electron Microscopy .....	55
4.1.2 Energy Dispersive X-ray Spectroscopy .....	57
4.1.3 FIB Focus Ion Beam .....	58
4.1.4 Atomic Force Microscopy .....	59
4.1.5 Spectroscopic Ellipsometry .....	60
4.2 Materials and Methods .....	60
4.2.1 Membrane degradation .....	60
4.2.2 Spectroscopic Ellipsometry .....	61
4.2.3 SEM, and EDX .....	61
4.3 Results .....	62
4.4 Conclusion .....	66
5. Electrochemical characterization of the nanofluidic membrane as homogeneous IFET nanochannels .....	67
Abstract.....	67
5.1 Introduction .....	68
5.1.1 Physical theory of conductivity in amorphous material .....	68
5.1.2 Electrical properties of the amorphous/crystalline heterojunction .....	72
5.2 Materials and Methods .....	72
5.2.1 Electrolytic solutions .....	72
5.2.2 Setup for electrochemical measurements .....	72
5.2.3 Nanofluidic membrane .....	73
5.2.4 Planar gate electrode fabrication.....	74
5.2.5 Electrode connection.....	75
5.2.6 Conductance, current-voltage (I-V) curves, and leakage current ...	75
5.2.7 SEM, AFM, and Ellipsometry .....	76
5.2.8 EIS .....	76
5.3 Results and Discussion .....	77

5.3.1. Nanofluidic membrane .....	77
5.3.2 EDL modulation: theoretical background and operation mode .....	78
5.3.3 Ionic conductance at the floating gate .....	80
5.3.4 I-V characteristics and leakage current.....	81
5.3.5 Power consumption in KCl.....	87
5.3.6 Leakage current in PBS .....	88
5.3.7 Power Consumption and Electrostatic gating energy efficiency in PBS .....	90
5.3.8 Leakage current and Cyclic voltammetry .....	90
5.3.9 EIS Investigation on polysilicon electrode using a blank device ...	92
5.3.10 Ellipsometry and AFM .....	92
5.4 Conclusion .....	101
6. In-vitro release of drugs .....	103
Abstract.....	103
6.1 Introduction .....	104
6.1.1 Ultraviolet-visible (UV-Vis) Spectroscopy .....	104
6.2 Materials and Methods .....	105
6.2.2 In vitro release fixture.....	105
6.2.3 In vitro release modulation .....	106
6.2.4 Statistical analysis.....	107
6.3 Results .....	108
6.3.1 In vitro release of Alexa Fluor 647 .....	108
6.3.2 In vitro release modulation of polystyrene sulfonate.....	109
6.3.3 In vitro release modulation of DNA salt.....	110
6.3.4 Performance of release modulation through electrostatic gating..	111
6.3.5 In vitro control release of methotrexate .....	114
6.3.6 In vitro controlled release of quantum dots .....	115
6.4 Conclusion.....	116
7. Design of the Printed Circuit Board for drug release control .....	117
Abstract.....	117
7.1 Introduction to wireless communication .....	118
7.1.1 Radio Frequency Communication .....	118
7.1.2 Power .....	119

7.2 Drug Delivery Device.....	120
7.3 Electronic Printed Circuit Board Design .....	123
8. Conclusion and Future Perspectives .....	137
9. References.....	140
10. List of publications .....	163
11. Appendix.....	164
12. Article Permission Reprinting .....	164

---

# List of Figures

Figure 2. 1: Release profile concentration in plasma.....	11
Figure 2. 2: Schematic of the electric double layer and relative model.....	13
Figure 2. 3: Effect of the distribution of surface potential.....	15
Figure 2. 4: Schematic of a cross-section of a silica nanochannel in a solution....	16
Figure 2. 5: Velocity profile associated with the electrophoretic transport.....	17
Figure 2. 6: Schematic illustrating the concentration polarization. ....	21
Figure 3. 1: General photolithographic process.....	28
Figure 3. 2: 2D model of semiconductors.....	37
Figure 3. 3: A typical polysilicon CVD system.....	38
Figure 3. 4: Possible configuration of the amorphous silicon carbide network. ...	41
Figure 3. 5: Fabrication process schematics. ....	43
Figure 3. 6: Final wafer featuring 120 nanofluidic membranes. ....	44
Figure 3. 7: Nitrogen Gas Test.....	49
Figure 3. 8: Nanofluidic membrane. ....	50
Figure 3. 9: EDX measurement relative to one membrane.....	51
Figure 3. 10: Variable Angle Spectroscopic Ellipsometric Data.....	52
Figure 4. 1: Teardrop generated by the collision of the incident electron beam and the specimen surface. ....	56
Figure 4. 2: Atomic model displaying the shells K, L, and M.....	57
Figure 4. 3: Ellipsometric measurement principle.....	60
Figure 4. 5: Nanofluidic membrane degradation. ....	63
Figure 5. 1: Electronic density of states in amorphous silicon carbide. ....	69
Figure 5. 2: Conduction mechanism associated to the hopping transport. ....	70
Figure 5. 3: Schematic reporting the density of state, the abrupt conduction mechanism, the band tail hopping .....	71

Figure 5. 4: Assembled system setup to perform electrochemical measurements.	73
Figure 5. 5: Image of the silicon nanofluidic membrane. ....	78
Figure 5. 6: Measurements set for I-V characteristics. ....	79
Figure 5. 7: Floating gate ionic conductance. ....	80
Figure 5. 8: Ionic current $I_{DS}$ when gate potential $V_{GS}$ and transmembrane potential $V_{DS}$ are applied. ....	83
Figure 5. 9: I-V ( $I_{DS}$ vs $V_{DS}$ ) ionic transfer characteristics and leakage current ( $I_{GS}$ vs $V_{GS}$ ) characteristics ....	86
Figure 5. 10: Normalized conductance ....	87
Figure 5. 11: Gate leakage current. ....	88
Figure 5. 12: Leakage current and cyclic voltammetry in PBS. ....	91
Figure 5. 13: Ellipsometric and AFM measurements. ....	93
Figure 5. 14: Blank setup measurements. ....	94
Figure 5. 15: Comparison between the fitted values for a-SiC and SiO <sub>2</sub> . ....	96
Figure 5. 16: C-V and G-V data plots. ....	99
Figure 5. 17: Flat band potential and density of states evaluation. ....	100
Figure 6. 1: Rendering of the custom device used for in-vitro release modulation. ....	105
Figure 6. 2: Modulated release of Alexa Fluor 647. ....	109
Figure 6. 3: Modulated release of Poly(sodium 4-styrenesulfonate) and DNA. ....	111
Figure 6. 4: Statistical analysis of release modulation. ....	112
Figure 6. 5: Electrostatically controlled release of methotrexate. ....	114
Figure 6. 6: Electrostatically controlled release of quantum dots. ....	115
Figure 7. 1: Implant components, printed circuit board (PCB) and applied polarization potentials. ....	122
Figure 7. 2: Rendering of the implantable capsule. ....	123
Figure 7. 3: Schematic circuit of the printed circuit board. ....	125
Figure 7. 4: Bluetooth Low Energy Microcontroller Pin Diagram. ....	126
Figure 7. 5: Schematic circuit of MCU and VDDR network. ....	127

## List of Figures ---

Figure 7. 6: Schematic diagram of the electric circuit for the RF communication antenna. ....	129
Figure 7. 7: Radiation diagram of the ceramic antenna for XY, ZX, and YZ plane. ....	129
Figure 7. 8: Schematic of the electronic circuit for the generation of the polarization potential. ....	130
Figure 7. 9: Layers of the PCB .....	131
Figure 7. 10: Manufacturing rules and constraints used for design and development of the PCB.....	132
Figure 7. 11: Manufacturing rules used for the design of the PCB. ....	133
Figure 7. 12: Cross-section of the Board Layer Stack. ....	134
Figure 7. 13: Report of the rule validation generated by Altium® Designer. ....	134
Figure 7. 14: 3D rendering of the Printed Circuit Board. ....	135

---

# List of Tables

Table 3. 1: The process flow for the nanofluidic membrane. ....	47
---	----



---

# Chapter 1

## Introduction

The objective of the thesis was to develop and assess a silicon nanofluidic implantable nanofluidic device and electronic control for tunable drug delivery.

This thesis is organized into five main chapters. Chapter 2 presents an overview on the nanofluidic membrane for nanomedicine and personalized medicine for chronic diseases is presented. Chapter 3 describes the fabrication methods using the photolithographic process. In Chapter 4 the degradation of the nanofluidic membrane is described. In Chapter 5 the electrochemical characterization of the nanofluidic membrane is presented. In chapter 6, the release of charged molecules as proof of concept is illustrated. In Chapter 7 the electronic board control for remote Bluetooth communication is presented. A more detailed outline of each chapter is presented here below.

In Chapter 2, a general background of the nanofluidic implantable devices is provided. Explanation of the electrical double layer is reported. The general mechanism of transport phenomena in the nanochannels such as electrophoresis, electroosmosis, streaming potentials, and concentration polarization are introduced to explain the electrokinetics of the electrostatic gated silicon nanofluidic membrane.

A detailed description of the lithographic fabrication process is provided in Chapter 3. The solid-state nanofluidic membrane is obtained by performing photolithographic processes used in standard microelectronics to fabricate Micro-

and Nano-ElectroMechanical Systems (MEMS and NEMS). The SOI wafer used to obtain the two layers of the nanofluidic membrane underwent processes such as etching, oxidation, low-pressure chemical vapor deposition, and plasma-enhanced chemical vapor deposition. The final obtained membranes provided with a buried electrode featured 278600 nanochannels.

In Chapter 4, the inertness of the nanofluidic membrane was tested in vitro by performing a study in simulated physiological conditions, in three different scenarios: 1) using phosphate buffer saline added with sodium fluoride at 37 °C and 2) in accelerated conditions at 77 °C, and 3) using phosphate buffer saline added with sodium fluoride and bovine serum albumin. Final results showed no evidence of degradation across all tested conditions.

In Chapter 5, nanofluidic properties about ionic transport in the nanochannels, leakage currents and power consumption of the membrane, and physical properties of the buried polysilicon electrode are illustrated. The investigation was conducted in different concentrations of potassium chloride solution and phosphate buffer saline. Results showed that the nanofluidic membrane could act as an ionic field-effect transistor IFET. By manipulating the electrical double layer of the nanofluidic channels, the ionic conductance was modified accordingly to the polarity of the applied potentials, leading to a reduction in an enhancement of the transport of charged species in the channels.

Chapter 6 provide a proof of concept of the in-vitro control release rate of five medical relevant charged molecules: a small fluorophore (Alexa Fluor 647), a large polymer poly(sodium 4-styrenesulfonate), a medically relevant agent (DNA), multi-functional nanoparticles with applicability from bio-labeling to targeted drug delivery (quantum dots), and a first-line therapeutic approach for rheumatoid arthritis (methotrexate). Results showed that the transport modulation via electrostatic gating achieved efficient and reliable effects. Depending on the weight of the charged molecules, the aqueous solution used for the experiment, and the dimensions of the nanochannels, the release rate showed significant reduction.

In Chapter 7, the design of an electronic board for remote control for Bluetooth communication is presented with the final implantable drug delivery platform. The printed circuit board designed exhibits a final dimension of 20 mm x 12 mm x 0.425 mm. Further, future works for possible improvements to provide a closed-loop drug delivery system are illustrated.

I confirm that the work submitted is my own, except where work which has formed part of jointly-authored publications has been included. My contribution and those of the other authors to this work have been explicitly indicated below. I confirm that appropriate credit has been given within this thesis where reference has been made to the work of others.

The work presented in this dissertation is based on the patent “*Gated Nanofluidic Valve for Active and Passive Electrosteric Control of Molecular Transport and Methods of Fabrication*,” U.S. Provisional Pat. Ser. No. 62/961,437, filled by Dr. Alessandro Grattoni in Jan. 15 (2020).

Chapters 2, 3, 4, 5 and 6 contain parts of the results that have been published in the manuscripts titled “*Electrostatically gated nanofluidic membrane for ultra-low power controlled drug delivery*”, authored by Nicola Di Trani\*, **Antonia Silvestri**\* (Ph.D. candidate), Antons Sivoz, Yu Wang, Donald R. Erm, Danilo Demarchi (supervisor), Xuewu Liu and Alessandro Grattoni (co-supervisor), (\*equal contribution, co-first authorship), *Lab Chip* **2020**, *20*, 1562–1576, doi:10.1039/D0LC00121J, and “*Silicon Nanofluidic membrane for Electrostatic Control of Drugs and Analytes Elution*”, authored by Nicola Di Trani, **Antonia Silvestri**, Yu Wang, Danilo Demarchi, Xuewu Liu and Alessandro Grattoni, *Pharmaceutics* **2020**, *12*, 679, doi:10.3390/pharmaceutics12070679.

As co-first author in the Lab on a Chip publication, I carried out: conceptualization, data curation, methodology, formal analysis, investigation and visualization.

Other authors have contributed as detailed: Nicola Di Trani: conceptualization, data curation, formal analysis, investigation, software, visualization, and writing original draft. Antons Sizovs: conceptualization, supervision and validation. Yu Wang: methodology and investigation. Donald R. Erm: methodology and

investigation. Danilo Demarchi: validation. Xuewu Liu: conceptualization, methodology, investigation. Alessandro Grattoni: conceptualization, funding acquisition, project administration, writing original draft and validation.

As co-author in the Pharmaceutics publications, I carried out: conceptualization, formal analysis, investigation, methodology.

Other authors have contributed as detailed: Nicola Di Trani: conceptualization, data curation, formal analysis, investigation, methodology, software, visualization, writing original draft; Xuewu Liu: conceptualization, funding acquisition, methodology, resources, validation, Alessandro Grattoni: conceptualization, funding acquisition, project administration, resources, supervision, validation, writing – review and editing. Yu Wang: investigation, methodology, Danilo Demarchi: supervision, validation

The work described in this Chapter 5 is reedited parts of the manuscript submitted for consideration for publication in *Membranes* titles “*Silicon carbide gated nanofluidic membrane for active control of electrokinetic ionic transport*”, and authored by **Antonia Silvestri**, Nicola Di Trani, Giancarlo Canavese, Paolo Motto Ros, Leonardo Iannucci, Sabrina Grassini, Yu Wang, Xuewu Liu, Yu Wang, Danilo Demarchi and Alessandro Grattoni. This manuscript has been submitted to *Membranes*.

As first author in the *Membranes* publication, I carried out: Conceptualization, Methodology, Software, Formal Analysis, Investigation, Data Curation, Writing Original Draft, Writing Review and Editing; Visualization.

Other authors have contributed as detailed: Nicola Di Trani: Conceptualization, Data Curation, Visualization; Giancarlo Canavese: Conceptualization, Validation, Supervision; Paolo Motto Ros: Validation; Leonardo Iannucci: Methodology, Software; Sabrina Grassini: Resources; Yu Wang: Investigation; Xuewu Liu: Experimental Design, Funding Acquisition; Danilo Demarchi: Conceptualization, Validation, Resources, Supervision; Alessandro Grattoni: Conceptualization, Validation, Resources, Supervision, Project Administration, Experimental Design, Funding Acquisition.

Chapters 7 contain parts of the results that have been published in the manuscripts titled “*Remotely controlled nanofluidic implantable platform for tunable drug delivery*”, authored by Nicola Di Trani, **Antonia Silvestri**, Giacomo Bruno, Thomas Geninatti, Corrine Ying Xuan Chua, April Gilbert, Giulia Rizzo, Carly S. Filgueira, Danilo Demarchi, and Alessandro Grattoni, *Lab Chip* **2019**, 19, 2192–2204, doi:10.1039/c9lc00394k.

As co-author in the Lab on a Chip publication, I carried out: formal analysis, visualization, and writing – original draft.

Other authors have contributed as detailed: Nicola Di Trani: conceptualization, data curation, formal analysis, investigation, software, visualization, and writing original draft; Giacomo Bruno: conceptualization, data curation, investigation, and software; Thomas Geninatti: conceptualization, data curation, and investigation. Corrine Ying Xuan Chua: validation and writing – original draft. April Gilbert: investigation; Giulia Rizzo: investigation; Carly S. Filgueira: conceptualization and formal analysis; Danilo Demarchi: conceptualization. Alessandro Grattoni: conceptualization, funding acquisition, project administration, and validation.

---

## **Chapter 2**

# **Nanotechnology, nanomedicine, personalized medicine, and controlled drug delivery system**

### **Abstract**

Nanomedicine and nano delivery systems represent a new evolving science that takes advantage of nanotechnology. The nanometric scale is used as a tool to diagnose and deliver drugs and therapeutics to specifically targeted sites in a fine controlled fashion. The recent advancements in nanotechnology in nanomedicine lead to several critical applications for numerous diseases such as chemotherapy, immunotherapy, and biological detections. In this chapter, the application of nanotechnology to nanomedicine with a focus on nanofluidics is presented to provide the fundamental working principles of nanofluidic membranes for drug delivery.

## 2.1 Introduction

With the advent of increasingly advanced technological processes, new and unique materials, and improvement in manufacturing processes, nanotechnology is drawing ever greater attention to itself, spreading in many different fields, such as solid-electronics with high precision nano quantum computers, as well as medicine with personalized health care[1,2].

To be classified as nanotechnology, a device needs to feature at least one dimension as nanometric and consequently smaller than a few hundred nanometers[3]. Thus, the properties arising at the nanoscale are very different from those observables at the macroscale, generating the unique properties[4] governing the nanometric nature[5]. In fact, at nanoscale regime, conventional equations and rules are dramatically different. In fact, at this nanoscale, close forces interaction, such as Wan der Walls forces, are hundreds of times more relevant than the macroscopic forces such as gravity or pressure. Consequently, the interaction between forces requires quantum mechanics to be explained and fully characterized. Interaction between molecules, however, has been investigated as a unique and novel phenomenon, with properties and rules that enable nanotechnology, especially when nanomedicine is considered, to be a powerful, alternative, and new approach to solve problems actually still unsolved.

The first approach to control and manipulation of single atoms was performed forty years ago by the arrival of the scanning tunneling microscope (STM) [6]. With this new instrument, the movement of molecules that formed ultra-precise patterns in a single atom thick substrate was possible. Thanks to this, the discovery and the further development of many molecules, such as quantum dots, among many others, were possible. The introduction to the imaging and analysis of the nanometric scale allowed nanotechnology to be introduced more and more in everyday life.

Materials can influence the nanoscale rules in several fields. Examples are the industry of semiconductors and optoelectronics. In fact, after 1980 and the burst of nanotechnology, many areas such as aerospace, chemical industry, energy sectors,

and many others start to invest in research to investigate and fully characterize the unique properties of the nanoscale world significantly.

The breakthrough of nanotechnology profoundly changed medicine and gave birth to an entirely novel field called nanomedicine. In fact, the numerous properties of the nanoscale can draw a completely new approach in therapeutics administration, especially in chronic diseases and oncology therapies[7,8].

In nanomedicine, the target drug delivery represents a crucial aspect. Nowadays, medical institutions like the National Institute of Health (NIH) widely support research and discovery in this field. In fact, nanotechnology represents one of the critical academic research that is gradually moving to translational clinical studies and commercial proceeds.

## **2.2 Implantable Drug Delivery Systems**

The implantable drug delivery systems have recently gained considerable attention due to their potential role as substitutive of a non-adherence regime from the patients[9]. They are primarily based on microdevices and nanodevices, usually micro- and nano-electromechanical system technologies employed in the biological field, such as BioMEMS and BioNEMS. Those systems allow the development of micro- and nano-devices dedicated to diagnosing, monitoring, and treating a wide range of acute and chronic diseases[10,11].

The manufacturing fabrication technique used for the BioMEMS and the BioNEMS is derived from the solid-state microelectronics techniques. The specific application of implantable devices required the BioMEMS and BioNEMS to be fabricated with biocompatible materials that generate a low inflammatory response from the immune system of the patient[12]. Luckily, many materials that are used in the microelectronics industry are biocompatible. In fact, materials like silicon nitride, silicon dioxide, and silicon carbide are widely used to fabricate integrated circuits at the microscale[13].



The most used material in solid-state microelectronics is silicon. Its properties such as mechanical robustness, easily chemical versatility and biocompatibility[14–17] candidates the silicon among the ideal material for biomedical applications[1]. In fact, many devices for implantable delivery of drugs are realized by taking advantage of the numerous silicon properties. Examples of MEMS devices range from sensory application [18], to nanofluidic membranes [19], from infusion micropumps, micromixers and valves[20] to microneedles[21]. The photolithographic process required to realize those types of devices assures the reproducibility of the devices, as well as a noticeable uniformity[22].

In the last decade, implantable delivery systems for drug administration at a desired time and dose or rate by using nanopores, nanoslots, and nanochannels structures have become more and more common. The possibility of fabricating nanostructure with silicon usage allows the realization of a very precise, reproducible, scalable, and accurate nanodevice[23,24]. Generally, nanopores and nanochannels structures in drug delivery permit the administration of therapeutics based on the needs of the patient at a constant release rate, avoiding burst administration and reducing the adverse effects[25,26]. As notable examples, nanofluidics devices have been developed for the prevention and treatment of diseases such as HIV[27,28], cardiovascular diseases[29], muscle wasting[30], hormone deficiencies[31,32], obesity and metabolic syndrome[33,34], and cancer[35,36] among others.

## **2.3 Constant release and controlled release implantable devices**

The current administration of therapeutics is based on the widely used approach “one-size-fits-all” paradigm where treatment and prevention are designed around conventional disease archetypes. Those are represented by systemic administration of oral, local, and intravenous therapeutics. The general and common disadvantageous aspect of those treatment regimens is the high initial dosage provided right after the administration of the therapeutics, which is associate with

a rapid increase of the drugs in the bloodstream that can cause a toxic reaction and multiple side effects. After the initial burst, the presence of the administrated drug in the blood plasma exponentially decays (Figure 2.1A) as the effect of the clearance is implemented by internal organs such as the liver and kidney. The therapeutic windows where the drug administration is effective and not toxic results to be inadequate. The consequence of this phenomenon can lead to the inefficacy and ineffectiveness of the administrated treatment[32]. Additionally, these drug administration modalities suffer from poor patient adherence to treatment[37,38], which limit the efficacy of the medication.

To overcome these fluctuations, it is possible to use technologies to provide a long-term sustained zero-order release of therapeutics. In fact, in this case, the fluctuation of the administrated therapeutics in the bloodstream is reduced, keeping the therapeutic window in the optimal range (Figure 2.1B).

Many devices based on nanofluidic technologies were developed in the last decades to be employed as drug delivery systems[19,39]. Among them, nanofluidic membranes were firstly used in the release of interferon-alpha[40]. Other uses as drug delivery contemplate the release of glucose and immune isolation of pancreatic islets of Langerhans in biocompatible capsule[17,41,42]. Another example of nanofluidics membranes commercially available for personalized medicine is based on micro-drug reservoirs, each one sealed with a gold lamina already implanted in humans[43], or micro implants for ophthalmology applications[44].

An essential aspect to be considered is the need to control the administrated drug by dosage and time[45,46]. In fact, some diseases require an administration of therapeutics based on the circadian cycle, such as hypertension and rheumatoid arthritis[47]. The need to develop such personalized care and precision medicine required control over the release of therapeutics to allow the stoppage to adhere to the needed chronotherapeutic regime[48]. To release of drugs in chronotherapy is illustrated in Figure 2.1C. The control over the release rate can be achieved in different manners, and among many, the remote control can offer a comprehensive advantage in terms of telemedicine[49,50]. In fact, this can avoid the need for the patient to undergo hospital visits. A recent approach is represented by the

radiofrequency and the Bluetooth Low Energy system due to its simple implementation and security features of the system. Additionally, it is possible to build a network of sensors (implanted or worn) that can provide feedback to personalize tailoring of the dosage of the drug to be released[51–53].

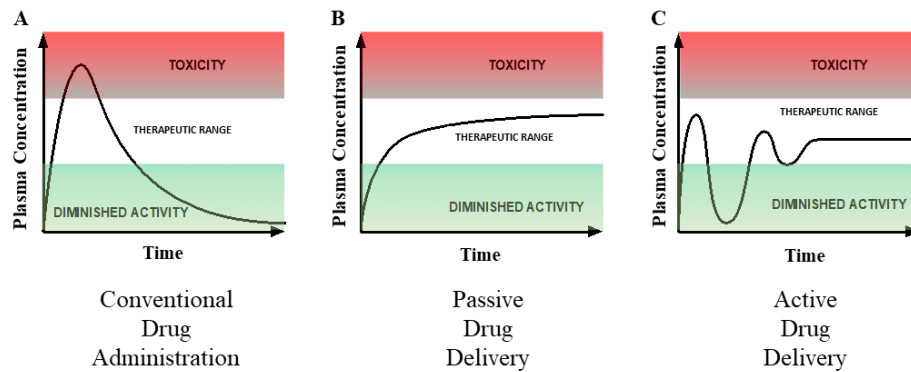


**Figure 2. 1:** Release profile concentration in plasma. Administration in case of A) conventional drug delivery, B) zero-order sustained drug release, and C) controlled drug delivery administration.

## 2.4 Silicon Gated Nanochannel Membrane for Drug Delivery System

Silicon nanofluidic membranes are nanofluidic devices based on nanochannels technology. The nanochannels offer unique nanometric properties to interact with charged species and molecules thanks to their dimensions[54–56]. When in contact with aqueous media, solid surfaces express electric charge due to the ionized surface group or the adsorbed ions. The charged surface actively interacts with ions and charged particles in the solutions by influencing their distributions in the solution[57]. In particular, the ions exhibiting opposite charge to that expressed by the surface, also named counter-ions, are electrostatically attracted to the surface. In contrast, the ones expressing a similar charge to that of the surface, also called co-ions, are repelled. The combination of the electrostatic attraction and the thermal movement of the ions lead to the formation of a thin layer on the charged surface called the electrical double layer (EDL)[58,59].

This thin layer consists of immobile layer formed by counter-ions that neutralize the expressed surface charge, and a mobile layer formed by counter-ions and co-ions are free to diffuse near solid-liquid interface.

To describe the EDL, numerous models were proposed. The Helmholtz model describe the EDL as an overlap of two charged layers located at a fixed distance. Another model developed by Gouy-Chapman describe the EDL as a shield composed by diffused ions which the most external ones are free to move in the solution. Afterwards, a combination of those two models was proposed in the Gouy-Chapman-Stern model. In this case, the EDL present an overlap on two layers, called compact layer and diffuse layer. The compact layer is constituted of solvent molecules and ions immobile and adsorbed to the surface material/solution interface, while the diffuse layer is composed by mobile molecules and ions carrying net charge in the solution. The GCS-EDL model is reported in Figure 2.2.

The shielding ions in the fluid generated an inner layer called Stern layer, further divided in the inner Helmholtz layer and the outer Helmholtz layer, and overlap to it there is the diffuse layer composed by solvated ions. The thickness of the inner Helmholtz layer is strictly dependent on the finite size of the ions, since the center of ions can only attract on the surface by their hydrated radius. The potential expressed by the charged surface, reported in Figure 2.2 as red line, represent the electrokinetic potential, also known as Zeta potential, at solid-liquid interface. It establishes the number of counter-ions involved in the formation of the EDL following the principle of the electroneutrality to balance the charge on the solid surface. It has to be considered that some counter-ions could be thermally energized by random thermal motion of ions present in the solution and they could achieve enough kinetic energy to escape from the EDL.

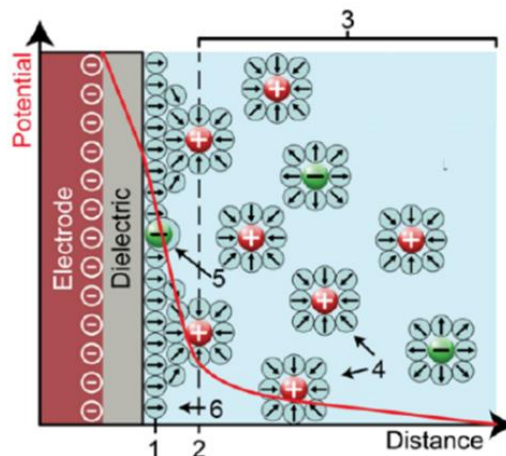


**Figure 2. 2:** Schematic of the electric double layer and relative model. (1) Inner Helmholtz plane; (2) Outer Helmholtz plane; (3) Diffuse layer; (4) Solvated ion; (5) Specifically adsorbed ion; (6) Molecules of the electrolyte solvent.

The parameter governing the distribution of the charges in the diffuse layer is the Debye length. In fact, the Debye length is responsible for screening the surface potential, or equivalently, the surface charge of the material. Mathematically, the Debye length for a 1:1 electrolyte can be expressed as

$$\lambda_D = \sqrt{\frac{\epsilon_0 \epsilon_r kT}{2z^2 q F C_0}} \quad (2.1)$$

where  $C_0$  represents the bulk concentration,  $\epsilon$  is the dielectric constant ( $\epsilon = \epsilon_0 \epsilon_r$  where  $\epsilon_0$  is the permittivity of vacuum and  $\epsilon_r$  is the relative dielectric constant of the medium),  $k_B$  is the Boltzmann constant,  $T$  is the temperature,  $e$  is the electron charge and  $N_A$  is the Avogadro's number. In particular, for a symmetric electrolyte aqueous solution where the concentration of positive and negative electrolyte is equal, at  $T = 300$  K the Debye length can be simplified as

$$\lambda_D = \frac{9.61}{z\sqrt{c_b}} \quad (2.2)$$

with  $\lambda_D$  expressed in nm, and the bulk concentration  $C_0$  is expressed in mM. The equation highlights that  $\lambda_D$  is only dependent on the properties of the aqueous solutions and not on any other characteristics such as surface charge or surface potential.

In a nanochannel device, the diffuse layer does not decay to electroneutrality as it would happen in an unconstrained volume, and by manipulating the surface charge of the surface, it is possible to extend the thickness of the EDL, leading in the overlapping of the diffuse layer.

Typical values of  $\lambda_D$  in aqueous solution are comprised between 1 nm and 100 nm and they are defined by the concentration of the ionic solution. Based on the smallest dimension of the nanochannel, that typically is indicated with height ( $h$ ), it is possible to encounter two scenarios: a high ionic concentration exhibiting a Debye length smaller than the height of the nanochannels,  $\lambda_D \ll h$ , or a low ionic concentration exhibiting a Debye length bigger than the height of the nanochannel  $\lambda_D \gg h$ . In the first case, the bulk solution in the channel is the same of the solution outside of the nanochannels, typically in a reservoir. This is due to the fact that the potential decay to zero very rapidly and its value is kept zero in the majority of the bulk solution. In the second case, the potential distribution in the nanochannels is altered by the counter ions that accumulated on the charged surface. Figure 2.3 reports the two described cases. When the nanochannel exhibits a surfaces charge  $\sigma_s$  for all his confinement sides, it is possible to state that the average ion concentration  $n_{ch}$  inside the nanochannels is given by  $n_{ch} = 2|\sigma_s|(qh)$ , where  $q$  represents the electronic charge and  $h$  represent the nanochannel height. As consequence, the surface charge influences the conductance in the nanochannels, since a positive  $\sigma_s$  enhances the present of anions, while a negative  $\sigma_s$  recalls cations in the nanochannels. This is at the basis of the exclusion-enrichment phenomenon[60] that can be observed only in nanochannels due to their capability to interact with particles featuring nanometric size.

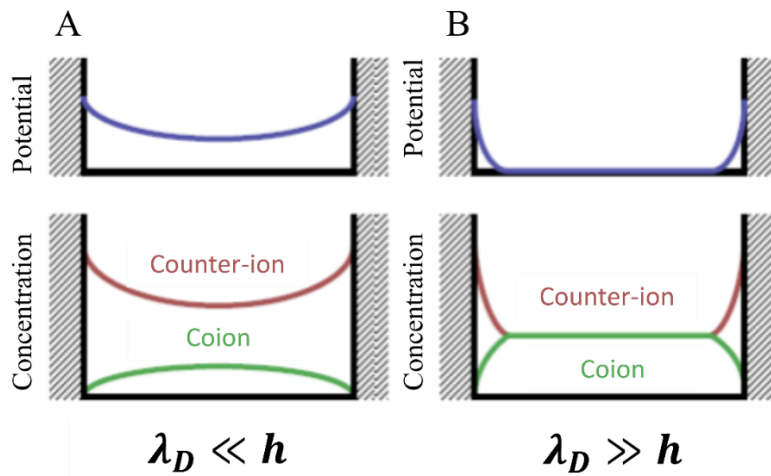


**Figure 2. 3:** Effect of the distribution of surface potential on the ionic charge distribution in channels exhibiting different dimension. A) in case of microchannel or in presence of ionic concentration exhibiting  $\lambda_D \ll h$ , the distribution of charges in the channel is not influenced by the surface potential. B) in case of ionic concentration exhibiting  $\lambda_D \gg h$ , the surface potential is raised in the bulk of the channel. Consequently, the effect of enrichment-exclusion can be observed.

## 2.5 Transport Phenomena in Nanochannels

Transport phenomena in nanochannels can be ascribed to four main categories [61,62]:

- Electrophoresis
- Electroosmosis
- Streaming potential, and
- Sedimentation potential.

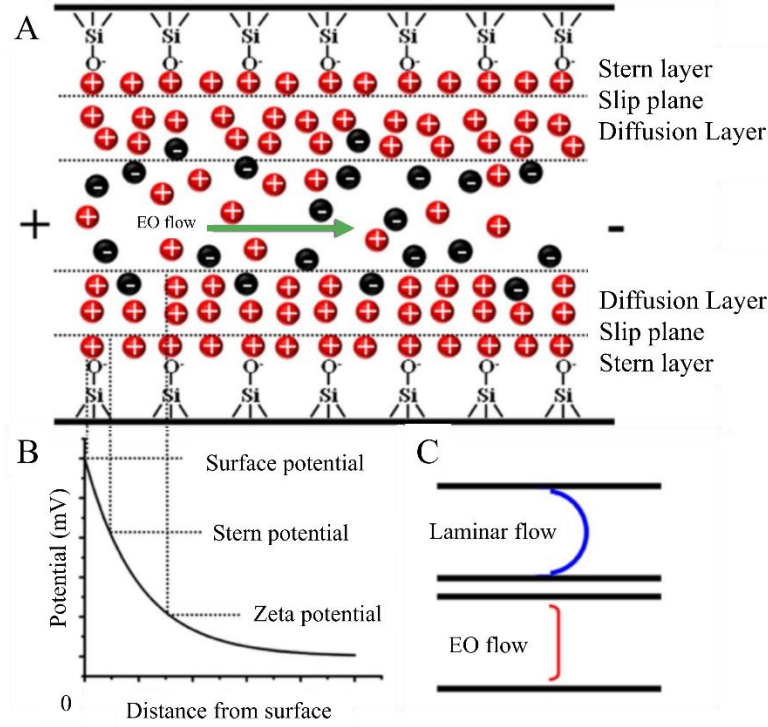


**Figure 2. 4:** Schematic of a cross-section of a silica nanochannel in a solution. A) Illustration of the EDL and the electroosmotic transport. B) Potential profiles associated with the different layers of the EDL. C) Velocity profiles of the laminar flow and the electroosmotic flow in the presence of an EDL overlapping. i.e., the height of nanochannels is smaller than the EDL.

**Electrophoresis.** Electrophoresis is the phenomenon that generates a movement through a channel of charged species and molecules by the application of an electric field. The electric field imposes to the particle to move under the effect of the velocity

$$v_{EP} = -\left(\frac{\varepsilon_0 \varepsilon_r}{\eta}\right) \zeta_{species} E \quad (2.3)$$

where  $\varepsilon_0$  represents the vacuum permittivity,  $\varepsilon_r$  represents the relative permittivity of the solution,  $\zeta_{species}$  represents the zeta potential of the considered particles,  $\eta$  represents the viscosity of the solution, and  $E$  denotes the applied electric field.



**Electroosmosis.** Electroosmosis is the phenomenon that governs the movement of charged species and molecules in the nanochannels by the application of an electric field. In this case, the transport mechanism is driven by the Coulomb forces of the electric field. Similarly to the previously described case, the velocity generated can be calculated as a drift velocity

$$v_E = -\left(\frac{\varepsilon_0 \varepsilon_r}{\eta}\right) \zeta_{surface} E \quad (2.4)$$

where  $\varepsilon_0$  represents the vacuum permittivity,  $\varepsilon_r$  represents the relative permittivity of the solution,  $\zeta_{surface}$  represents the zeta potential of the considered particles,  $\eta$  represents the viscosity of the solution, and  $E$  denotes the applied electric field.

Velocity profiles characterizing the electroosmosis and the electrophoresis are different. In the case of the electrophoretic flow, the velocity profile is approximately constant from one wall to the other wall, comprising the nanochannel bulk, as shown in Figure 2.4C. Instead, the velocity profile describing the electrophoretic flow is non-linear, and it exhibits the maximum velocity at the center of the nanochannel. Additionally, in the case of electroosmotic flow, the velocity is considered to differ from zero at the nanochannel wall. This phenomenon is associated with the fluidic molecular transport in the bulk of the nanochannel that generated a movement of the charged particles forming the EDL. Figure 2.5 illustrates the velocity profile of the electrophoretic flow is reported.

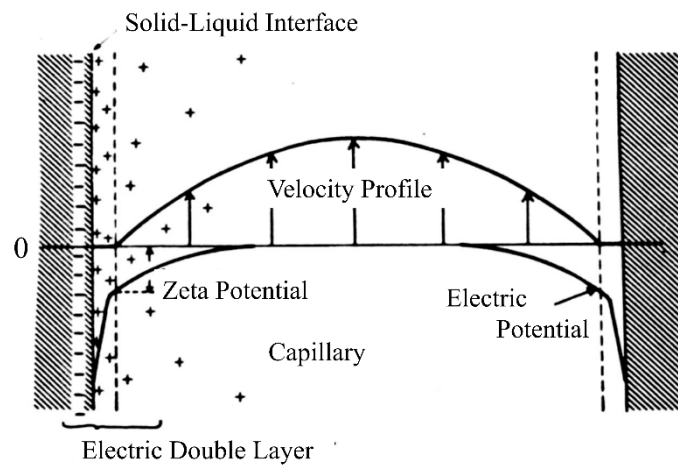


**Figure 2. 5:** Velocity profile associated with the electrophoretic transport.

**Streaming potential.** The streaming potential and the sedimentation potential are two techniques that rely on pressure-driven transport. In fact, they require the application of pressure through micromechanical systems such as pumps or valves. The methods needed to generate those movements are not very practical compared to using a couple of electrodes to generate an electric field and, consequently, electroosmotic and electrophoretic transport.

Electroosmosis and electrophoresis phenomena mainly depend on two parameters: the ionic concentration of the solution and the electric field applied between two electrodes at the inlet and the outlet of the nanochannel. By adjusting those two parameters, it is possible to generate one type of molecular transport or the other. In particular, the electroosmotic flux can be produced applying an electric field (higher than 200 V/cm), while to generate the electrophoresis, a lower electric field is required (usually greater than 3 V/cm). Further, the electroosmosis can be observed for low ionic concentrations, which exhibit molarity comprised in the range of nM – mM. At the same time, electrophoresis requires a higher ionic concentration in the order of M[63,64].

It is essential to point out that using a high electric field could lead to the phenomenon of electrolysis at the electrode surface. For this reason, the electrophoretic flux may represent a more suitable technique to induce molecular transport. Additionally, the pressure gradients are lower than those generated via electroosmosis since they are not produced by the fluid movement in the nanochannel bulk [46,65]. However, the adoption of the type of transport mechanism depends on the final application of the nanofluidic device.

To describe the electric potential generated by the ionic concentration, the Poisson equation can be used

$$\varepsilon_0 \varepsilon_r \nabla^2 \psi = -\rho \quad (2.5)$$

where  $\rho$  represents the free charge density in the solution (C/m<sup>3</sup>).  $\rho$  can be evaluated using the equation 2.6

$$\rho = \sum_{i=1}^N z_i n_i e \quad (2.6)$$

where  $z_i$  represents the valence of the  $i^{\text{th}}$  species,  $n_i$  the concentration of the  $i^{\text{th}}$  of the ionic solution, and  $N$  the number of the different ionic species. Substituting the equation 2.6 in equation 2.5, the Poisson potential becomes

$$\nabla^2 \psi = -\frac{1}{\epsilon_0 \epsilon_r} \sum_{i=1}^N z_i n_i e = -\frac{\sigma}{\epsilon_0 \epsilon_r} \quad (2.7)$$

where  $\sigma = \sum_{i=1}^N z_i n_i e$  represents the surface charge density on the nanochannel wall.

The movement of the particles in the fluid inside the nanochannels can be described by the Navier-Stokes equations for incompressible fluid. Additionally, the collision of the particles as an effect of the electric field forces can be considered using the electromechanical-force-density equation, and the combination of those originate a system accounting for the momentum and continuity equation[66]:

$$\nabla \cdot \vec{u} = 0 \quad (2.8)$$

$$\frac{\partial \vec{u}}{\partial x} + \rho \vec{u} \cdot \nabla \vec{u} = -\nabla \rho + \mu \nabla^2 \vec{u} + \vec{f} \quad (2.9)$$

where  $\vec{f}$  represents the electric force. Considering the significantly small Reynold number in this case of micro-nanochannels, the viscosity forces are significantly more prominent than the convective forces, which can be avoided. For this reason, equation 2.9 can be rewritten as

$$0 = -\nabla \rho + \mu \nabla^2 \vec{u} + \vec{f}. \quad (2.10)$$

To represent the electrokinetic flow, the  $\vec{f}$  can be expressed

$$\vec{f} = \rho \vec{E} = -\sum_{i=1}^N (z_i n_i e) \nabla \psi. \quad (2.11)$$

The Nernst-Planck equation represents a combination of the electrokinetic phenomena, i.e., diffusion, convection, and electromigration, and the transient phenomena associated with convection is described with the equation

$$\frac{\partial c_i}{\partial t} = \nabla \cdot \left( D_i \nabla c_i + \frac{D_i e z_i \nabla \psi}{k_B T} c_i - \vec{u} c_i \right) \quad (2.12)$$

where  $c_i$  represent the molar concentration of the  $i^{\text{th}}$  species,  $D_i$  the coefficient of the diffusivity, and  $\vec{u}$  the axial velocity. By conveying equation 2.12 with the Poisson equation, the Plank-Nernst-Poisson equation is obtained. The solution to this equation cannot be easily identified, also in the case of basic or classical structure as the cylindrical configuration. In the nanoscale environment, it is possible to simplify the Poisson-Nernst-Plank equation by discounting the convection expression. The steady-state Poisson-Nernst Plank equation can be rewritten as

$$0 = \nabla \cdot \left( D_i \nabla c_i + \frac{D_i e z_i \nabla \psi}{k_B T} c_i \right) \quad (2.13)$$

Alternative form of the Poisson-Nernst-Plank equation consider the number concentration  $n_i = N_A c_i$ , where  $N_A$  represents the Avogadro's number.

## 2.6 Concentration polarization phenomenon

The joint of the nanochannel with the microchannel under an applied electric field can generate a specific phenomenon known as concentration polarization. The concentration polarization[67,68] is generated when the ionic solution present in the nanochannel exhibits an ionic depletion[69,70]. This phenomenon is observable when the characteristic Debye length  $\lambda_D$  of the solution is more significant than half the nanochannel height[71]. Under this effect, it is possible to observe that the ions and the counter-ions occupy two different regions of the nanochannels.

The Debye length can be evaluated as

$$\lambda_D = \sqrt{\frac{\varepsilon_0 \varepsilon_r kT}{2C_\infty e^2 N_A}} \quad (2.14)$$

where the  $C_\infty$  represents the ionic concentration in the bulk of the nanochannel.

In Figure 2.6 is reported the concentration polarization phenomenon obtained as a consequence of the application of the electric field at the anode and cathode electrodes.

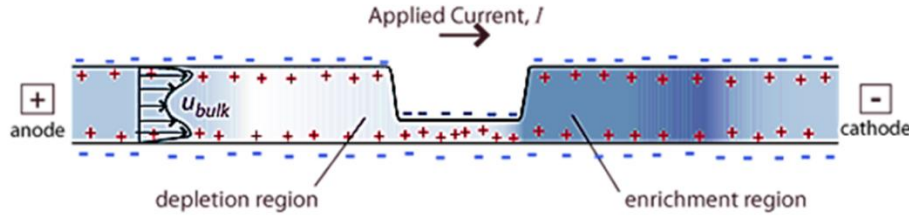


**Figure 2. 6:** Schematic illustrating the concentration polarization phenomenon.

The overlapping of the EDL causes the access of the counter ions and the repulsion of the coins in the nanochannels. At the same time, at the anode electrode, there is a considerable concentration of ions at the cathode electrode, while there is a small number of ions at the anode electrode. As a result, there is a generation of a concentration gradient in the device that leads to the increased electrokinetic response, specifically in the depletion region. It exhibits a nonlinear behavior, definable using second-order phenomena, such as second-order electroosmosis and microvortices.

The second-order electroosmosis is one kind of electroosmosis at non-equilibrium, where the velocity of the fluid is  $\propto E^2$ , while in equilibrium, the electroosmosis exhibit a velocity linearly dependent on  $E$ , where  $E$  represents the electric field. Additionally, low values of potential applied at the electrodes generate a linear ohmic dependence of the ionic current in the nanochannel. When the potential is increased, the higher values of the potential generate a higher ionic

current leading to a higher concentration of the ion at the anode zone close to the nanochannel. In contrast, the cathode zone experiences the depletion of ions until their presence is negligible. At this point, the ionic current tends to a limiting value that cannot be increased further.

---

## **Chapter 3**

# **Design and mechanical characterization of the nanofluidic membrane**

### **Abstract**

Silicon solid-state nanofluidic membrane is developed using photolithographic techniques widely used for VLSI systems and microprocessors, among many electronic devices. In fact, photolithography resembles a set of tools for the manufacturing of the nanochannel devices for drug delivery considered the required precision, accuracy, throughput, and reliability necessary for many clinically relevant dosing regimens. Additionally to those favorable aspects, many materials compatible with silicon manufacturing have been demonstrated to be highly biocompatible. In this chapter, the fabrication processes of the nanofluidic membrane are illustrated in details.

### 3.1 Introduction

Nanofluidic membrane is a nanofluidic device that can be fabricated as a MEMS by using micromachining process and or photolithographic processes. MEMS devices features sizes generally comprised between 100 nm and 10 mm, Generally, they rely on the fabrication techniques widely used for microelectronic. Those are batch processes that allow the fabrications of several device units at the same time with high reproducibility. Despite those processes are expensive, the batch production of a large number of devices at the same time permits a low cost per each device.

Several advantages can be achieved when we microfabrication processes are applied to the fabrication of MEMS devices, specifically on the electrical properties of the films and the precise control of the dimension of the final MEMS device. In fact, precise doping profile in fabrication of to form different junctions for electrical conduction is achievable with high precision. Moreover, many materials compatible with silicon manufacturing have been demonstrated to be highly biocompatible[72,73].

To control the precise dimensions of the device, microelectronics fabrications techniques can craft a 3-dimensional structure from a 2-dimensional top view of the device. This approach is called planar processing and it is the most highly developed in fabrication technologies. It relies on lithographic pattern transfer, and it is suitable for high-volume, low-cost manufacturing production.

Generally, a microfabrication process flow is organized on 3 main steps: i) deposition or growth of a material film characterized with specific mechanical and electrical properties, ii) a lithographic step to transfer the desired patterns to the underlying substrate or film, and iii) a selective removal of the films through physical or chemical processes. Additionally, some few other processes can be considered: iv) a planarization step to level the wafer, flattening the surface by reducing the roughness and the height differences across the wafer, v) doping step, used to control and modify the electrical properties and/or film thickness, vi) bonding step to connect the wafers and substrates to other substrates.



An important aspect in designing the process flow is the materials used in the fabrications process. Traditionally, silicon and polysilicon are the materials vastly used in microfabrication processes. Historically, silicon was widely employed due to its mechanical assets and its excellent electrical properties. However, other materials discovered over time were use since they offered remarkable advantages compared to silicon. The Young's module and the tensile yield strength of the silicon are comparable to the metals and stainless still. While exhibiting similar properties to the silicon, the polysilicon possesses a tightly packed grains structure. This represents a crucial aspect for electrical and mechanical properties of the films, since the mechanical and thermal stress can generate variations of the material properties and morphology, causing even failure.

Another material in microfabrication is silicon dioxide, widely used as electrical insulator or masks in sacrificial processes during device fabrication. In fact, in its amorphous form, the  $\text{SiO}_2$  is often used to insulate glass substrates in MEMS and NEMS application. Due to its biocompatible features, it is used in BioMEMS devices, where insulating devices optically transparent are desired[74,75]. In its crystalline form generally known as quartz,  $\text{SiO}_2$  exhibits piezoelectric properties convenient for sensing and actuation applications[76,77]. In fact, due to the low losses exhibited at high frequencies, crystalline  $\text{SiO}_2$  is used for RF MEMS applications[78,79].

Additional dielectric silicon based massively used is the Silicon Nitride  $\text{Si}_3\text{N}_4$ , since its chemical stability makes it a suitable candidate for mask layering during microfabrication etching process. Contrary to  $\text{SiO}_2$  that can deposited or grown on silicon substrate,  $\text{Si}_3\text{N}_4$  can be deposited at a very slow growth rate. This property permits to achieve a low internal stress in the grown films that increments the mechanical stability.

Initially introduced to operate at high temperature, Silicon Carbide ( $\text{SiC}$ ) represents valid alternative material to previous ones. It exhibits a large Young's modulus and chemical inertness, qualities that make it an ideal candidates to fabricate structural layer for device functioning in harsh[80,81] and/or biological environments. Specifically, in this last case,  $\text{SiC}$  was demonstrated to increase stress resistance of the coated substrate, and to be a valid alternative as sensing application for biological environments [82–84].

Other materials presenting piezoelectric properties are lead zirconate titanate (PZT) employed for actuation and sensing purposes given by its mechanical deformation obtained as a consequence of an application of the electric field[85–87]. Other piezoelectric materials are zinc oxide (ZnO) and aluminium nitride (AlN) [88,89]. Additionally, a wide range of metals are also used in microfabrication. In fact, aluminium, gold, titanium and nickel have been widely utilized as structural materials [90,91].

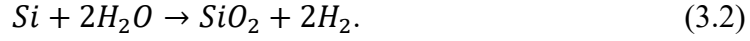
### 3.1.1 Processes used to fabricate the nanofluidic membrane

**Growth and Deposition of Films.** In a MEMS device, a key parameter is represented by thin layers and films. The fabrication of those films, i.e., metal, dielectric, or semiconductor, can be achieved by growth on a starting substrate material or by deposition employing specific processes. The method for fabricating the thin film depends on the application. In fact, several factors related to the microfabrication processes that strongly influence the properties of the final films. In fact, mechanical properties (i.e. stress within the grain modulus), electrical properties (i.e. electrical conductance), thermal properties (i.e. thermal conductivity), optical properties (i.e. reflectivity), quality (i.e. amount of defects in the film), thickness uniformity across the wafer, chemical and ferromagnetic properties, deposition/growth rate and processes costs.

**Thermal Oxidation.** The thermal oxidation process is employed to grow silicon dioxide film on silicon or polysilicon substrate. SiO<sub>2</sub> film obtained through the thermal oxidation demonstrated to be easily controlled in term of thickness and fabrication. In fact, silicon reacts to oxygen at high temperature with a rate-controlled oxidation process that occurs in the oxide or at the interface following this reaction in case of *dry oxidation*:



Instead, in case of *wet oxidation*, the oxygen element is obtained by vapor generation, and the reaction can be described as



In fact, this process does not require control of flow transport of reactants. Additionally, the variations of grown silicon dioxide thickness from the edge to the center of the wafer are negligible. Quality of oxide can be controlled by supplying the only two gases needed for the reaction (oxygen and hydrogen) from condensed liquid tanks to reduce the amount of contaminating impurities.

The thickness of the grown film can be evaluated by considering the kinetics of the oxidation of silicon described by the Deal-Grove model [92–96]:

$$t = \frac{x_{ox}}{B/A} + \frac{x_{ox}^2}{B} \quad (3.3)$$

where  $t$  represents the oxidation time,  $x_{ox}$  represents the oxide thickness, and  $B/A$  and  $B$  represent linear and parabolic rate constants, respectively. This model states that reaction rate is initially limited by the availability of reaction sites of the substrate surface. Due to this requirement, the process slow down as the thickness of the oxide film increases. The wet oxidation that involves water molecules can provide a growth rate higher than the dry oxidation since the oxygen molecules forming the water  $H_2O$  are smaller than the single element  $O_2$ . For this reason, they can penetrate and diffuse through the film, reaching silicon reaction sites.

Mathematically, this can be described with linear kinetics

$$x_{ox} = \frac{B}{A} t \quad (3.4)$$

and the thickness of the oxide in a “diffusion-limited” process can be estimated as

$$x_{ox} = \sqrt{Bt} \quad (3.5)$$

The dependency of the oxidation reaction upon the temperature requires a precise control thermal condition of the furnace for the development of the growth

of the film. The formation of the oxide subsequent to the diffusion of oxygen into the oxide layer to reach the substrate surface has a remarkable consequence. Since the reaction sites involved in the process are directly placed into the crystalline silicon, the oxidation is completely free from impurities that could be present at the surface.

**Photolithography.** The photolithography represents one of the most important steps in microfabrication of solid-state devices. It is appropriate in transferring the desired pattern onto planar surfaces and substrate.

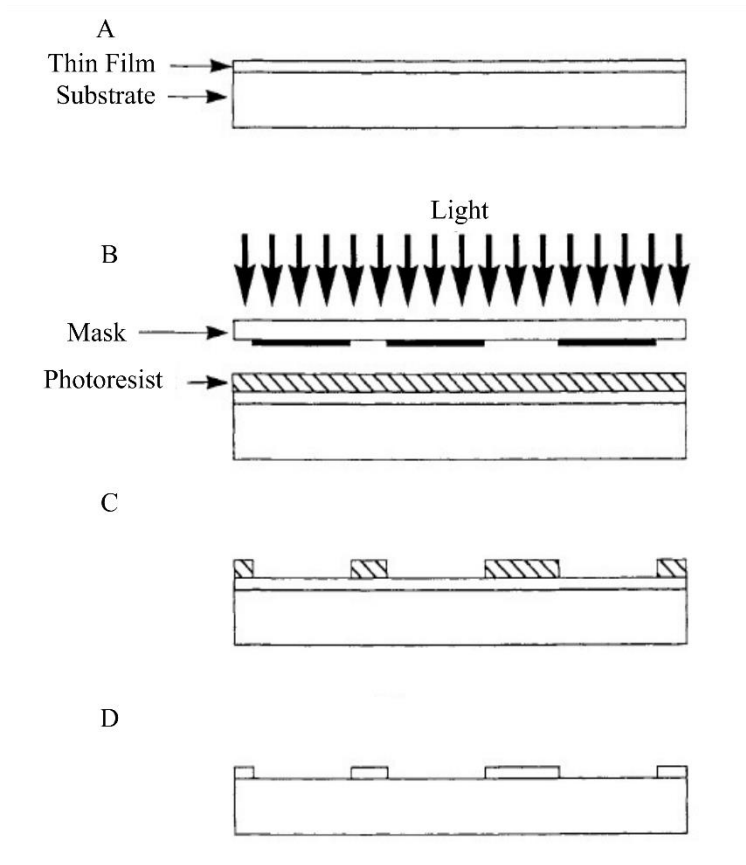


**Figure 3. 1:** General photolithographic process. (A) Planar substrate coated with photoresist. (B) Photoresist exposed to the light through a mask. (C) Elimination of exposed area is removed in a developer. (D) Elimination of unwanted area preserving the wanted area protected by the photoresist using an etching process.

It is composed by few repeated steps used to fabricate both electrical and mechanical devices. They are described in the following.

1. Prebake of the wafer called “singe” for few minutes at a temperature  $T \geq 200\text{ }^{\circ}\text{C}$ . This step is important for the complete removal of the excess of water that could be present on the surface and could prevent the further adhesion of the photoresist.
2. Application of the adhesion promoter on the planar surface. A widely used promoter for  $\text{SiO}_2$  planar surfaces is the hexamethyldisilazane (HMDS).
3. To avoid any difference in height, the surface with the applied adhesion promoter is subjected to spin coating with a speed that slowly increases until several hundreds of rpm are reached. The final thickness of the adhesion promoter is generally about few micrometers, and can be finely controlled and reproduced by acting on the rotation rate and the viscosity of the promoter.
4. A soft bake step is following to promote adhesion of the photoresist on the surface. The typical tools to perform the soft bake step are convection oven at  $900\text{ }^{\circ}\text{C}$  for 30 min, infrared oven for 3 to 4 min, hotplates for 1 minutes, or microwave oven for only few seconds.
5. The following step aligns the pattern projected the pattern sketched in the mask onto the surface with specific markers. In case of first alignment, the marker to be referred are placed on the substrate. Alternatively, if a high accuracy is required, the alignment marks can be etched in the substrate. Further alignment of the masks can be performed by mean of those etched marks. the exposure can be executed in a whole-wafer exposure system, or alternatively, in a stepper system. In the first system, the dimension of the pattern exhibits the same dimension of the substrate, and the mask is placed in proximity of the wafer. If the mask is directly in contact with the substrate, the system is called “proximity aligners”. This type of system allows the transfer of the pattern in only one step. On the contrary, in the case of the stepper system, a repeated procedure of is performed on a small area of the wafer at time, and subsequently steps are required to expose the whole wafer. Generally, the pattern sketched in a glass substrate called reticle refers to a single die. This type of system is able to achieve a higher precision compared to the whole-wafer system due to small area involved

in the process per times. The full wafer is patterned by opportunely moving the reticle over the substrate area.

In some cases of micromachined devices, where the patterns must be transferred on bot side of the wafer, there is the need to employ an additional alignment tools to align two masks at time. Alternatively, it is possible to perform the exposure one side at time.

The exposure process involves an intense light that modify the resist by enhancing or reducing its solubility. In fact, after the exposure, the wafer is immersed in a solution called developer that is in charge to remove part of the resist. In particular, if the exposed resist immersed in the developer molten, then the resist is called positive. Since the remaining part of the resist are associated to dark area on the mask, the mask is called positive.

6. The exposed wafer develops the resist by immersion in adequate solution. In case of positive resist, the commonly used developers are alkaline solution such as NaOH, and KOH. The removal of the soluble resist does not involve the unexposed area, since the solubility achieved by the positive resist is thousand times higher than the unexposed resist.
7. A development inspection is performed after the development step, to check for any defect due to masks unalignments, incomplete development of the resist, or inappropriate exposure time.
8. A step of hard bake is required to remove any remaining solvents and water from the surface. Temperatures are typically comprised between 150 °C and 1800 °C. The process can be performed in a convection oven and it takes almost 1 hour to be accomplished.
9. The baked wafer can be etched. The etching procedure is responsible to remove the area of the substrate not protected by the photoresist.
10. A etch inspection is performed to check the process was successful accomplished. In case the wafer exhibits unetched area, the it can be etched again, until the etching is successfully developed.
11. After the etch, the removal of the resist is performed during the stripped step. This process can be executed a wet procedure employing solvents such as acetone, trichloroethane, and alcohol, or even oxygen plasma and a combination of sulfuric acid with peroxide.

12. A final inspection process is performed using a microscope to confirm the total elimination of the photoresist.

Once the photolithographic process is ended, the wafer can be exposed to further microfabrication processes.

**Mask.** In photolithography, the information regarding the pattern to be microfabricated onto the substrate is carried by the mask. The mask is produced by photolithographic processes itself, which consist in exposing a resist film deposited on the mask plate. The techniques be used to create the mask are the direct reduction camera, the flashing tools, and the electron-beam exposure. In the direct reduction camera, the artwork to be reproduced onto the mask is scaled in size through a system of lenses assembled in a camera directly onto the reticle. Then, the reticle is reproduced on the whole area of the mask using a likewise stepper step used for the wafer in photolithography. In case of flashing, the pattern to reproduce onto the mask is achieved by flashing the light through small rectangles. By moving the mask with the help of a precision x-y stage, the mask is built up. In the third case, the exposure is performed by mean of the e-beam tools. Typically, those tools are scanning electron microscopes that features a high precision scanner that works with high-speed beam blanker. Those instruments possess a high precision stage too, to move the expose the area of the mask following a x-y direction.

Subsequently, the patterned mask is exposed and developed, similarly to the case of the photolithographic process. Then, the developed pattern of the mask is reproduced onto a metal layer, usually a chrome layer, through wet or plasma etching.

**Etching.** A fundamental step in microfabrication is represented by the etching process, often performed after the photolithographic step. The need to selectively remove a target material from the masking layer is crucial in the design of the device. Etchant materials, the etch types, and consequently the etch rate can be properly chosen to obtain the desired etched profiles. The masking materials generally to etch crystalline or polycrystalline silicon are silicon dioxide and silicon nitride, as well as metals, often employed in dry etching.

Based on the direction performed, the process can be classified as *isotropic*, if there is no directional preference, or *anisotropic*, if the etching is performed at different etching rate for a specific substrate. Furthermore, the etching profile can be classified as wet etching when executed in liquid media, or dry etching, when involving gaseous media [97–100].

The wet etching is based on chemical reaction occurring during the immersion of the substrate in an etchant media. This process presents some difficulties in controlling the etching rate of the sample. Additionally, it could involve impurities that contaminate the immersed sample. A wet etchant commonly used in microfabrication are alkali solution such as potassium hydroxide (KOH). It is often used due to his ability to perform anisotropic etching along single crystal silicon substrates. In fact, it etches 400 times faster the plane (100) of the silicon wafer compared to the plane (111) [98]. Another anisotropic etchant is tetramethyl ammonium hydroxide (TMAH), that feature a higher selectivity against silicon dioxide and silicon nitride compared to KOH. An isotropic etchant widely used is hydrofluoric acid (HF) in its pure or diluted form to remove sacrificial oxide layer given its remarkable selectivity to silicon.

**Reactive Ion Etching.** The vapor etching is a process that provide very low control over the rate etching, and this aspect hampers its employment in patterning of structure. For this reason, often microfabrication process relies on wet etching.

The reactive ion etching or RIE is a one of the etching processes performed using a vapor phase, where ions are generated from gaseous etchant. In fact, to avoid the lack of control over the etching rate, and to provide anisotropy to the gas phase, the etchant molecules present in the gas are electrically charged, generating ions. After, the ions are accelerated toward the wafer, and this step performs the anisotropic selectivity in a favorite direction through to the trajectory path depicted by the acceleration.

Ionization can be accomplished via usage of plasma or external electric field, that promote the collision of the energized free electrons in the chamber and the etchant molecules. The RIE process is usually performed at pressure chamber comprised in the range 5 mTorr to 500 mTorr [101]. Low value of pressure in the range of 5 to 20 mTorr can guarantee further directional anisotropic etching. In fact,



in this case, the large free mean path of the ions can favorite the collision with the substrate, and reduce molecular collisions. Under this condition of low pressure, the etching rate can reach the considerable value of 0.1  $\mu\text{m}/\text{min}$  or even less.

To further enhance etching rate, it is possible to add a magnetic field that mainly acts on ions and electrons in the plasma by directing them to follow a circular path. Due to the elongated traveled pathway, the electrons increase their probability to hit inactivated molecules and generate more energized electrons. This process obtained by application of a coil applied to the confined plasma volume is referred as *inductively coupled plasma* or ICP. The advantages achievable using this type of process are the considerable produced free radicals at the low pressure as 1mTorr, as well as the low RF power required. Additionally, the RIE ICP demonstrated to produce less damages during the directional acceleration, for this reason is less aggressive compared to the simple RIE.

**Deep Reactive Ion Etching.** Silicon can be etched by fluorine radicals generated by gases as  $\text{XeF}_2$ , and the accelerated ions toward the substratum. The RIE process can perform a vertical substrate etching that can reach a depth of 2 – 3  $\mu\text{m}$ . If the trench to be etched exceed this size, the etching attainable by RIE worsen as the depth increase. For this reason, substrate with thickness of hundreds of microns is etched by performing one of the two deep reactive ion etching (DRIE) techniques. One DRIE process is the Bosh process. The Bosh process is based on cyclic repetitive steps that alternate deposition and etching. After removal of  $\text{SF}_6$  from the chamber, a first step of deposition is performed by pumping  $\text{C}_4\text{F}_8$  that deposits over the substrate as  $\text{CF}_2$  due to bond breaking occurring in the chamber. At this point, the  $\text{CF}_2$  is removed by RIE etching, including the sidewalls of the trench. These subsequent steps are performed until the desired depth is reached. Each step can be rapid as few seconds or fractions, as well as longer as tens of seconds. Operating pressure ranges between 10 to 50 mTorr, and it is possible to reach etch rates comprised in a discrete wide range of 0.5 to 4  $\mu\text{m}/\text{min}$ . One important consequence of the Bosh etching is the roughness of the surface that usually is tens of nanometer. This type of process is particularly indicated for silicon substrate that exhibits high aspect ratio and depth [102].

The other DRIE process is the cryogenic process. In this case, the etching is performed in cold environment that favors the anisotropic etching through the directional bombardment of the ions. In fact, this type of process presents a better-defined etched profile exhibiting reduced surface roughness and no scallop-like features compared to the Bosch process [103,104]. Usually, the working temperatures are comprised in the range -170 °C to -100 °C.

***Chemical Vapor Deposition.*** The chemical vapor deposition or CVD is a procedure of deposition of materials that involved reactants in form of gases. The CVD is usually used to deposit films of polysilicon, dielectrics insulators, i.e., SiO<sub>2</sub> and some metals, i.e., tungsten. The chemical reactions occur at elevated temperature in the gas stream during the “gas-phase nucleation”. Subsequently, the formed particles create a robust film during the “deposition-phase”.

Generally, the CVD is performed at low pressure, and it is referred as low-pressure CVD (LPCVD). Typical values of pressure are comprised in the range 0.15 and 2 Torr. Very similarly to the oxidation process, the equipment for the CVD requires a furnace in which the chemical reactions can take place in a thermal controlled environment. Additionally, the tube demand to be sealed and evacuated, as well toxic and pyrophoric exhaust stream gases necessitate to be specifically handled. The equipment is specifically designed to finely control the rate deposition limited by the transport of the mass reactant in the gases. In fact, the equipment is provided with precision mass flow controller to precisely gauge the amount of reactant gases in the furnace chamber. Since the CVD does not involve a reaction rate limited process as happens in the case of oxidation, the temperature demand to be monitored with few degrees.

Polycrystalline silicon can be deposited via CVD by using the silane gas SiH<sub>4</sub>, that separates into silicon Si and hydrogen H gases. Despite the fact that deposition of polysilicon can be performed at low temperature such as 400 °C, a better robust film can be obtained at slightly higher temperature as 600 – 700 °C. In fact, in this last case the residual stress of the film can be negligible ensuring higher performance in microsystems that embed elements enduring considerable mechanical stress [105,106].

Other material that can be deposited are  $\text{SiO}_2$ , from reaction of silane and oxidant, such as oxygen or  $\text{N}_2\text{O}$ . Silicon nitride  $\text{Si}_3\text{N}_4$  is similarly deposited by considering as precursors ammonia gas  $\text{NH}_3$  and silane  $\text{SiH}_4$ . In this case,  $\text{Si}_3\text{N}_4$  require the high temperature 800 – 900 °C to be deposited, since the residual stress in the deposited material can be determined by the ratio of the gases in the furnace. If the proportion between the reactant is not well controlled, the film may comprise substantial amount of hydrogen, resulting in a not stoichiometric material.

The CVD permits the fabrication of doped films by addition of dopant gases. An example is represented by the phosphosilicate glass, obtained by introducing phosphine gas  $\text{PH}_3$  into the reactant stream flow during the deposition process of  $\text{SiO}_2$ .

***Plasma Enhanced Chemical Vapor Deposition.*** The plasma enhanced chemical vapor deposition or PECVD, is another deposition process driven by the glow discharge generated by the collisions of electrons and independent from temperature.

The RF plasma generator requires only few hundred Watts to produce a fractional ionization energy for the glow discharge of  $\sim 10^{-5}$ . In these conditions, the electrons are provided with enough eV to break atomic bonds and to ionize the molecules in the gases when they collide. For this reason, the process can be performed at ambient temperature, and the heat produced by the process is limited by the coupling of the low ionization fraction and the low background pressure, despite the plasma can present a noticeable electron temperature of 20000 K.

This process deposition is generally employed for silicon nitride  $\text{Si}_3\text{N}_4$  and silicon carbide  $\text{SiC}$ . The ultimate film incorporates a higher rate of hydrogen, and this phenomenon is responsible for a higher etching rate in comparison with other deposition processes. Another important aspect is the significant deposition rate that can reach the order of microns per minute. Thus, the film may present considerable stress, that could threaten to the robustness. This can be controlled by modifying the frequency used to generate the plasma. Often, the adhesion of the deposited film is enhanced by performing PECVD process at 300 °C or more.

**Doping.** The extensive employment of semiconductors in microelectronics is due to their electrical properties and the ease way with which can be modified. By introducing a restrained quantity of impurities to those materials, it is possible to achieve controllable and reproducible desired electrical characteristics. Such impurities are called dopants and can be introduced in the materials during the process called doping.

Considering a two-dimensional model of pure silicon crystal reported in Figure 3.2A, each atom shares with its neighbor the external electrons in a covalent bond, which are relatively firmly bound to their locations at low temperature. As a consequence, the semiconducting material act as an electrical insulator. An increase of temperature can provide enough energy to the external electrons to allow them to escape from those bonds, reducing the resistivity of the material. Nevertheless, the resistivity of the pure semiconductors is constant over a wide range of working temperature that covers the interval comprised between -40 °C to 140 °C.

During the doping process, a silicon atom is substituted with an atom owning an extra electron in the external shell, this electron is unrestrainedly bonded with its neighbor, and it is able to hop to the close silicon atoms, as reported in Figure 3.2B. The semiconductor that has been provided with extra electrons is defined as *n-type semiconductor*. The silicon atom can be also replaced by an atom that misses an electron, as shown in Figure 3.2C. In this case, the electron hops from the silicon to its neighbor material. Since the silicon has lost its electrons, it exhibits a positive charge due to its ionization. The hopping of the electrons can be associated to the movement of a mobile positive charge, that is also known as hole. The semiconductor that exhibits extra holes is defined as *p-type semiconductor*. Considering the period table, the n-type dopants are element of the V group such as phosphorous and arsenic, while the p-type dopants belong to the III group such as boron and aluminium.

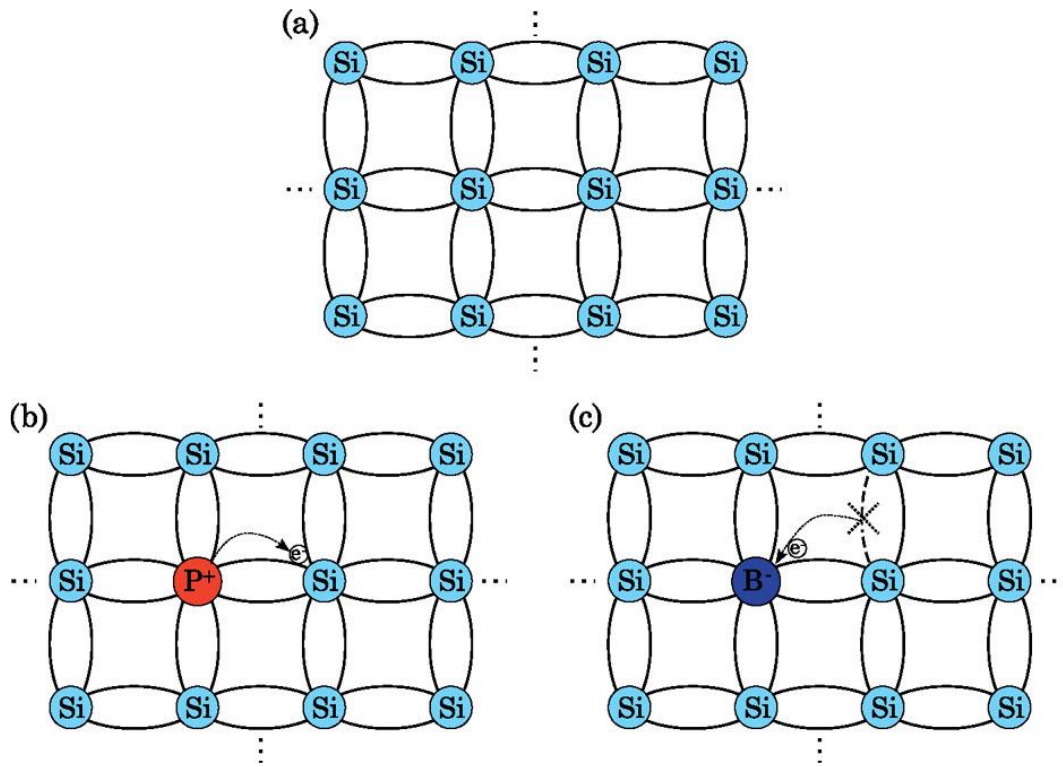


**Figure 3. 2:** 2D model of semiconductors. A) undoped silicon crystal semiconductor; B) n-type semiconductor doped with phosphorous, and C) p-type semiconductor doped with boron.

The process of doping can be performed through diffusion or through rapid thermal annealing systems. The diffusion process [94,96,107] can be performed inside a furnace, where the dopant are inserted in the chamber via gaseous compounds at a temperature that ranges from 800 °C to 1200 °C. The pressure of the chamber and the time for the doping process represent the two variables responsible for the level and the depth of the doping in the substrate. To prevent the doping, it is possible to coat the area that must remain undoped with masking film, such as  $\text{SiO}_2$  or  $\text{Si}_3\text{N}_4$ . This technique ensures a precise and reproducible doping profile. If there is not urgency for a definite and exact level and depth of doping, it is possible to perform the rapid thermal annealing doping technique. This technique requires that the area to be doped is covered with a paste containing the impurities, which are transferred to the substrate.

The diffusion is an isotropic process, which has as a consequence, that the doping depth and level can vary. Specifically, the dopants atoms diffuse laterally under the dark area of the mask, compromising the electrical performances of the doped area.

To avoid this event, alternative doping processes are based ion implantation similar to RIE process. The accelerated dopant atoms hit the substrate and penetrate. The penetration depth is established by their momentum and the crystalline structure. For this reason, the doping depth can be controlled by tilting the substrate. By varying the quantity of ions and the time of the process, it is possible to control the doping level.

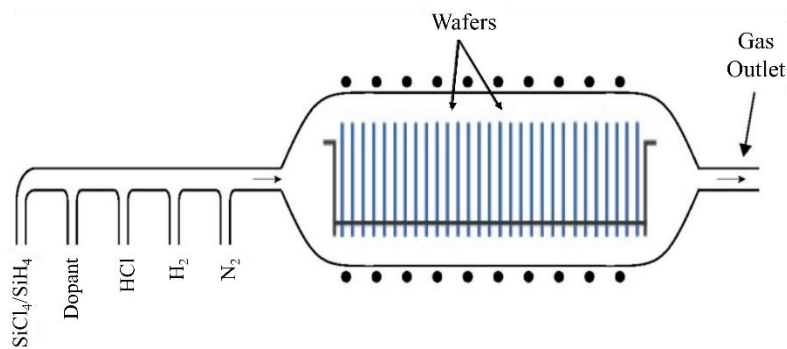


**Figure 3. 3:** A typical polysilicon CVD system. The furnace features the gas inlets and the heater elements around the chamber.

### 3.1.2 Materials used to fabricate the nanofluidic membrane

**Silicon-On-Insulator Wafer.** MEMS devices are often fabricated on both sides of the substrate, and during the final steps, the two sides are connected by removing a sacrificial layer through an etching procedure. The silicon on insulator wafer is a layered structure comprising two conductive layers separated by an insulating layer of  $\text{SiO}_2$ . The conductive layers are the crystalline device layer exhibiting a thickness of few micrometers and handle layer exhibiting a thickness of hundreds of micrometers, while the insulator layer called buried oxide layer exhibits a thickness of few micrometers. The employment of this type of structure can facilitate the process flow to fabricate a micromachined device, since the three-layered structure allow a fabrication process executable simultaneously on both conductive layers, without any interaction prevented by the insulator. When the process is completed,

the conductive layers are connected by removing the SiO<sub>2</sub> through etching procedure.

***Polycrystalline Silicon Phosphorous Doped.*** The polycrystalline silicon, also known as polysilicon, represent one of the most important material in microelectronics and microfabrication due to its capability to easily modulate its electrical properties, creating highly conductive silicide. Additionally, the polysilicon presents other valuable properties:

- mechanical properties demonstrated by the structure of the polysilicon are comparable to those exhibited by the single crystal silicon
- deposited by CVD deposition processes, it showed a good coverage;
- exhibited a high melting point temperature;
- demonstrated to form a high-quality oxide;
- it is compatible with HF.

Its selective deposition process permits the production of high-quality junctions, fill shallows and trenches, and create electrical contact by saliciding. In MOS devices, the employment of poly-Si facilitated the miniaturization of the structure, favoriting the multilayer interconnects, the drain and source contacts, the self-alignment of the gate over the body, and creating dielectric isolation.

Fabrication process for polysilicon material can include doping, etching, oxidation. Usually, the polysilicon is obtained upon standard hydrogenated amorphous silicon material, and it exhibits ah higher carrier mobility compared to the single crystalline silicon. The carrier mobility can be further increased by performing a doping procedure, and the resistivity of the material and the lifetime of the minority lifetime can be reproducibly modified.

The polysilicon grown by CVD process exhibited many advantages[108]. Among others, it is possible to consider

- uniformity in thickness and resistivity within the bulk material;
- reduced auto-doping issues caused by the chamber as a consequence of the low pressure and the low temperature used for the deposition process;

- reduction of the cost of the production, because of the simultaneously several wafers processed;
- control over the density of defects in consequence of performing the deposition in a longitudinal furnace. The vertical position of the wafer favors the falling of the particulates.

The deposition of the polysilicon is achieved by doping dilution gas of  $\text{PH}_3$  introduced in the deposition chamber.

***Amorphous Silicon Carbide.*** The silicon carbide is a silicon-based compound which presents polysilicon and amorphous form. Polycrystalline silicon carbide, for example the ceramics, demonstrated properties suitable for high-temperature and stress applications, as well as abrasive resistant application. Instead, in its amorphous phase, silicon carbide is used in microelectronics and in silicon heterostructures[109–111], as well as to coat substrate materials against corrosion[112] and abrasion[113] phenomena, and etching processes[114]. Additionally, it is widely used in medical field, as biocompatible material, for biomolecular applications[115] and medical devices[116].

Amorphous materials exhibit a very complex physical network. In case the amorphous material is a compound, as amorphous silicon carbide, the complexity increases. Regarding this aspect, several studies[117–120] demonstrated that the structural and electrical properties of the tetrahedral alloy strongly depends on the precursor gases. The fabrication process establishes the content of the hydrogen and the ratio carbon/silicon in the deposited material. In case the compound fabricated by PECVD, a-SiC is obtained by deposition of Si from  $\text{SiH}_4$  and ethane  $\text{CH}_4$ .

Due to the different dimension of their radius, the carbon and the silicon create an amorphous disordered network that is expected to be even more disordered compared to the amorphous silicon. In fact, since the covalent radius of the silicon atom is 117 pm while the covalent radius of the carbon is 77 pm[117], the ratio between carbon/silicon radius is 0.66, resulting in an highly disordered network. In Figure 3.4 is represented a possible disordered network that highlight the difference between radius of carbon and radius of silicon.



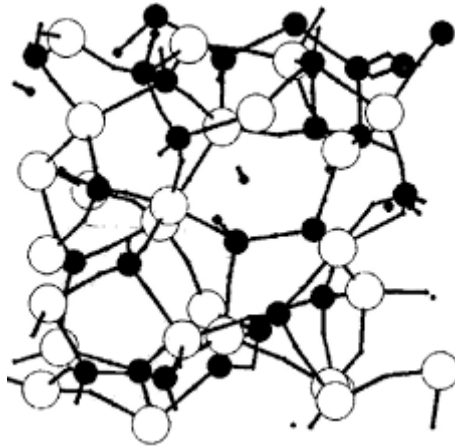


**Figure 3. 4:** Possible configuration of the amorphous silicon carbide network. The illustration highlights the difference between the radius of silicon (white dot) and the carbon (black dot).

If the deposition process is executed at temperatures minor than 600 °C, the incorporation of hydrogen element in the network of the a-SiC can be significant. As consequence, the thermal stability of the material is enhanced since the C-H bonds exhibit higher stability that the Si-H ones. Furthermore, based on the electronegativity exhibited by carbon and silicon, the carbon can hydrogens more easily than silicon. Therefore, the bonds between Si and H can be reinforced when the Si bonds to C.

## 3.2 Materials and Methods

### 3.2.1 Process fabrication steps of the nanofluidic membrane

The Nanofluidic Membranes employed in this study were fabricated starting from a 4-inch p-doped silicon-on-insulator (SOI) substrate with a device layer (10  $\mu\text{m}$ ), a buried oxide layer (1  $\mu\text{m}$ ), and a handle wafer (400  $\mu\text{m}$ ; Ultrasil Corporation, Hayward, CA).

The nanofluidic device was processed modifying a previously reported fabrication protocol[22] . It is the combination of photolithography and Reactive Ion Etching (RIE). The fabrication steps are illustrated in Figure 1. First, a 600 nm thermal oxide was deposited on the surface of the SOI wafer to act as a mask layer

for photolithography (Figure 3.5A). Arrays of template nanoslits (500 nm width by 6  $\mu\text{m}$  length) were patterned on the device layer by using standard photolithography on a contact aligner (KARL SUSS MA6) NR9-500P photoresist (Futurrex, Franklin, NJ) for the nanochannels (device layer). After transferring the pattern into the oxide mask layer by reactive ion etching (RIE), nanoslit (nanochannels) patterns were etched through the 10  $\mu\text{m}$  device layer via deep RIE (DRIE) on an ICP deep silicon etcher (PlasmaTherm, VERSALINE®) for 120 cycles, and stopped at the middle oxide of the SOI (Figure 3.5B). Each cycle includes polymer deposition for 2 s ( $\text{C}_4\text{F}_8$  150 sccm, Ar 30 sccm, pressure 25 mTorr, and Bias RF 10V), polymer removal from bottom of trench for 1.5 s ( $\text{SF}_6$  50, Ar 30 sccm, pressure 20 mTorr, and Bias RF 300V), and silicon etch for 0.75 s ( $\text{SF}_6$  50, Ar 30 sccm, pressure 25 mTorr, and Bias RF 10V). ICP RF power was 5000 Watts for all these steps. Backside macrochannels on the other side of the SOI, the handle wafer was patterned using double side alignment on the aligner (KARL SUSS MA6) and Megaposit SPR 220-4.5 photoresist for the macrochannels (handle layer). The layout of the handle wafer was designed with a high density of hexagonally arranged circular microchannels to provide mechanical stability.

Inductively Coupled Plasma (ICP) deep silicon etching was used to etch through the 400  $\mu\text{m}$  handle wafer, stopping at the buried oxide layer (Figure 3.5C). Backside macrochannels were etched about 500 cycles. For the backside etch, it includes polymer deposition for 2.5 s ( $\text{C}_4\text{F}_8$  75 sccm, Ar 30 sccm, pressure 25 mTorr, and Bias RF 10V), polymer removal from bottom of trench for 1.5 s ( $\text{SF}_6$  150 sccm, Ar 30 sccm, pressure 20 mTorr, and Bias RF 250V), and silicon etch for 3 s ( $\text{SF}_6$  300 sccm, Ar 30 sccm, pressure 25 mTorr, and Bias RF 10V). ICP RF power was 4000 Watts for all these steps. The wafer was Piranha cleaned after DRIE to remove the polymer build up on the sidewalls of nanoslits and macrochannels. Then, the 1  $\mu\text{m}$  middle buried  $\text{SiO}_2$  layer of the SOI was removed in a buffered oxide etchant (BOE) solution for 10 minutes to connect the nanoslits and macrochannel mesh (Figure 3.5D). The resulting nanoslits have a height of 770 nm. Following, a wet thermal oxidation was performed at 1055  $^\circ\text{C}$  in ultra-high-purity (UHP) water vapor for 11 min, resulting in a high temperature oxide (HTO)  $\text{SiO}_2$  formation that shrinks the nanochannel height to 580 nm (Figure 3.5E). To form the gate electrodes, phosphorus doped polysilicon (poly-Si) was deposited (121 nm thickness) via low-

pressure chemical vapor deposition (LPCVD; Figure 3.5F). The whole wafer structure was coated with a 64 nm SiC dielectric layer via plasma-enhanced chemical vapor deposition PECVD (Figure 3.5G). To expose the highly doped poly-Si, two contacts pads ( $\sim 1 \text{ mm}^2$ ) were created at the edge of the membranes by selective removal of SiC by fluorine-based RIE. The process is described in details in Table 3.1.

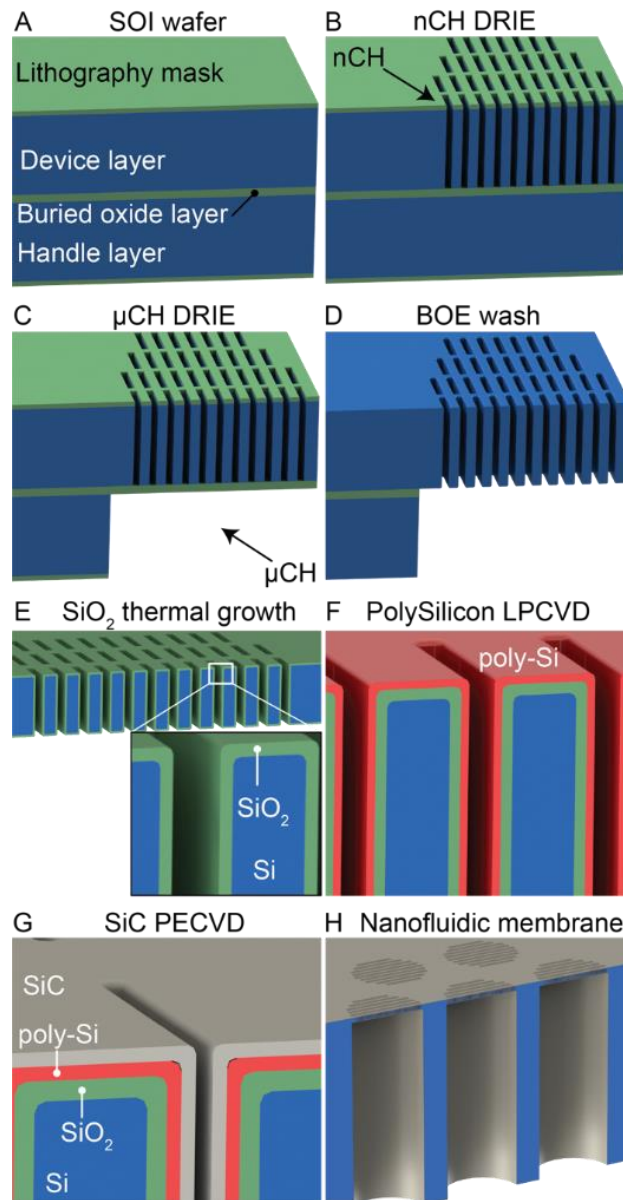


**Figure 3. 5:** Fabrication process schematics. A) Silicon-On-Insulator (SOI) wafer with lithography mask B) Deep reactive ion etching (DRIE) for nanochannel (nCH) patterning. C) DRIE for microchannel ( $\mu\text{CH}$ ) pattern. D)  $\text{SiO}_2$  mask removal. E)  $\text{SiO}_2$  thermal oxidation growth. F) Conductive poly-Si deposition. G) Insulating SiC deposition. H) Membrane structure.

Each wafer features 120 membrane chips (Figure 3.6), which were diced into individual membranes (6x6 mm<sup>2</sup>) via a dicing Saw (ADT 7100 Dicing Saw). Each chip presents 199 round microchannels organized in a hexagonal spatial configuration (Figure 3.5H). Every microchannel is connected to 1400 identical slit nanochannels (length 10 μm) organized in 19 rows and 96 columns. Each membrane chip features a total of 278,600 nanochannels.

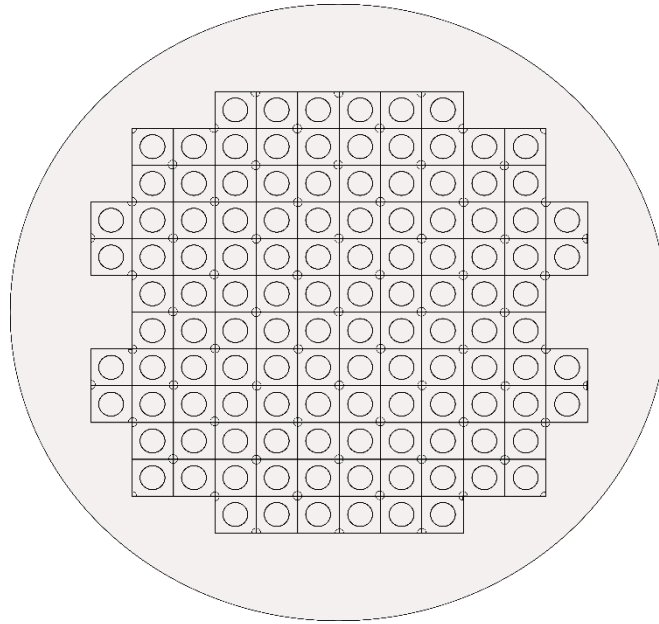


**Figure 3. 6:** Final wafer featuring 120 nanofluidic membranes.

Process Step:	Conditions:
Dry thermal oxidation of wafer for selective oxidation mask	1055°C 5 L/min O <sub>2</sub> Layer thickness: 600 nm
Photolithography for nanoslits array on device layer	KARL SUSS MA6 Contact aligner AZ 5209 as positive photoresist (Futurrex, Franklin, NJ), spun at 5000 rpm to a thickness of 700 nm
Reactive Ion Etching through silicon dioxide down to device layer to transfer nanoslits pattern into the oxide mask layer	PlasmaTherm 790 (PlasmaTherm, LCC) 40 sccm CHF <sub>3</sub> 3 sccm O <sub>2</sub> 75 mTorr

	1000 Watt Etch depth: 600 nm								
Deep Reactive Ion Etching through the device layer for nanoslits arrays	PlasmaTherm 790 (Plasma-Therm, LCC) 40 sccm CHF <sub>3</sub> 3 sccm O <sub>2</sub> 40 mTorr 1000 Watts Etch depth: 10 µm								
Inductively Coupled Plasma Deep Silicon Etching through 10 µm device layer	PlasmaTherm, VERSALINE® Generation 3 Deep Silicon Etcher (Plasma-Therm, LCC) <table border="1"> <tr> <td>Number of Cycles</td><td>120</td></tr> <tr> <td>               Polymer deposition:                C<sub>4</sub>F<sub>8</sub> 150 SCCM                Ar 30 sccm                25 mTorr                RF forward bias voltage 10V                RF forward bias power 5000Watts             </td><td>2 seconds</td></tr> <tr> <td>               Polymer removal from bottom of trench:                SF<sub>6</sub> 50                Ar 30 sccm                20 mTorr                RF forward bias voltage 300 V                RF forward bias power 5000 Watts             </td><td>1.5 s</td></tr> <tr> <td>               Silicon Etch:                SF<sub>6</sub> 50                Ar 30 sccm                25 mTorr             </td><td>0.75 s</td></tr> </table>	Number of Cycles	120	Polymer deposition: C <sub>4</sub> F <sub>8</sub> 150 SCCM Ar 30 sccm 25 mTorr RF forward bias voltage 10V RF forward bias power 5000Watts	2 seconds	Polymer removal from bottom of trench: SF <sub>6</sub> 50 Ar 30 sccm 20 mTorr RF forward bias voltage 300 V RF forward bias power 5000 Watts	1.5 s	Silicon Etch: SF <sub>6</sub> 50 Ar 30 sccm 25 mTorr	0.75 s
Number of Cycles	120								
Polymer deposition: C <sub>4</sub> F <sub>8</sub> 150 SCCM Ar 30 sccm 25 mTorr RF forward bias voltage 10V RF forward bias power 5000Watts	2 seconds								
Polymer removal from bottom of trench: SF <sub>6</sub> 50 Ar 30 sccm 20 mTorr RF forward bias voltage 300 V RF forward bias power 5000 Watts	1.5 s								
Silicon Etch: SF <sub>6</sub> 50 Ar 30 sccm 25 mTorr	0.75 s								

	RF forward bias voltage 10 V RF forward bias power 5000 Watts	
Photolithography for macrochannels array on handle layer	KARL SUSS MA6 aligner for double alignment Megaposit SPR 220-4.5 positive photoresist, spun at 4700 rpm to a thickness of 700 nm	
ICP deep silicon etching was used to etch through the 400 $\mu$ m handle wafer	PlasmaTherm, VERSALINE® Generation 3 Deep Silicon Etcher (Plasma-Therm, LCC)	
	Number of Cycles	500
	Polymer deposition: C <sub>4</sub> F <sub>8</sub> 75 SCCM Ar 30 sccm 25 mTorr RF forward bias voltage 10V RF forward bias power 4000Watts	2.5 seconds
	Polymer removal from bottom of trench: SF <sub>6</sub> 300 Ar 30 sccm 25 mTorr RF forward bias voltage 10 V RF forward bias power 4000 Watts	1.5 s
	Silicon Etch: SF <sub>6</sub> 50 Ar 30 sccm	3 s

	25 mTorr RF forward bias voltage 10 V RF forward bias power 4000 Watts	
Piranha clean of resist	H <sub>2</sub> SO <sub>4</sub> (96%) : H <sub>2</sub> O <sub>2</sub> (30%) = 2:1 (KMG Chemicals, Inc.: Ultra Pure Solution, Inc.	
BOE solution to remove 1 um of SiO <sub>2</sub> layer	6:1 buffered oxide etch (Capitol Scientific, Inc.) 10 minutes Final nanochannels height: 770 nm	
Wet thermal oxidation for nanochannels height reduction high temperature oxide HTO SiO <sub>2</sub>	1055°C ultra-high purity UHP water vapor 11 minutes Final height: 580 nm	
Gate electrode		
Low Pressure Chemical Vapor Deposition of phosphorous doped polysilicon gate electrode	800 °C 20 sccm SiH <sub>4</sub> 70 sccm PH <sub>3</sub> 70 mTorr Layer thickness: 121 nm	
Plasma Enhanced Chemical Vapor Deposition of amorphous silicon carbide	800 °C 20 sccm SiH <sub>4</sub> 70 sccm CH <sub>4</sub> 70 mTorr  Layer thickness: 64 nm SiC	
HF dip to selective removal of amorphous silicon Carbide via fluorine-based RIE	H <sub>2</sub> O : HF (49%) = 20 : 1 30 s (KMG Chemicals, Inc.) Exposed contact area: ~ 1 mm <sup>2</sup>	

**Table 3. 1:** The process flow for the nanofluidic membrane.

### **3.2.2 Focused ion beam (FIB), scanning electron microscope (SEM) imaging, energy dispersive X-ray spectroscopy (EDX) and ellipsometry**

The structure and fabrication repeatability of the nanofluidic membrane was assessed by imaging with a dual-ion beam (FIB) system FEI 235 at the nanofabrication facility of the University of Houston, Texas. Nanochannel cross sections were obtained using gallium ion milling. The resulting structures were imaged at a 52° angle using scanning electron microscopy (SEM). Evaluation of the silicon and carbon quantities inside the thin layer of the nanochannels was performed via EDX spectroscopy, while the thickness of the deposited layer was measured via ellipsometric spectroscopy.

### **3.2.3 The gas testing system**

The structural integrity and the reproducibility of the fabrication protocol of the nanochannel membranes was investigated by using the convective nitrogen flow test[121]. This procedure, called burst test[22], allows the estimation of the time constant of the fluidic characteristic of the nanochannels. It permits to measure the dimension of the nanochannel by mean of a nitrogen gas[23]. The gas transport across nanochannels consisted in application of nitrogen gas under specific pressure flowing through the nanochannels device layer. The pressure used for the test was 0.1 MPa. The structural integrity and the reproducibility of the fabrication protocol were evaluated performing a burst test at pressure comprised between 0.1MPa and 1MPa. The process of evaluation is detailed discussed in Fine et al.[22] In Figure 3.7 it is reported the nitrogen gas test.



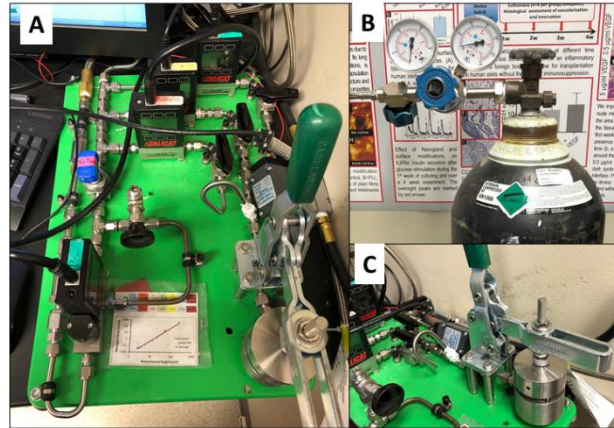


**Figure 3. 7:** Nitrogen Gas Test used to evaluate the size of the nanochannels and the mechanical robustness of the nanochannels membrane. A) Mass Flow meters connected to the pressure controller. B) Nitrogen Gas tank. C) Membrane holder.

## 3.3 Results

### 3.3.1 Nanofluidic membrane

To assess the quality of the fabrication process, all chip membranes were first visually inspected through optical microscopy. Then a gas test characterization on all chips to assess the nanochannel dimension uniformity across the wafer was performed. I employed a previously developed model to predict the nanochannels dimension from the measurement of transmembrane nitrogen gas flow upon application of a pressure difference[23]. A gaussian non-linear fit ( $R^2 = 0.99$ ) of the cumulative distribution of the obtained values shows a predicted nanochannel size of  $292 \pm 44$  nm. Selected chips were further analyzed using FIB-SEM imaging (Figure 3.8). Figure 3.8A shows a picture of a single diced chip which has a size  $6 \times 6$  mm<sup>2</sup> and a thickness of 400  $\mu$ m. The membrane features 199 cylindrical microchannels which measure 200  $\mu$ m in diameter and 390  $\mu$ m in length.

The hexagonal configuration of the cylindrical microchannel ensures high channel density and structural mechanical robustness. Nanochannels are efficiently aligned in a circular pattern that matched the microchannel area (Figure 3.8B, 3.8C). Figure 3.8D shows FIB cross sections of the slit nanochannels where despite

the high aspect ratio, all deposited layers show high uniformity (inset of Figure 3.8D). The innermost  $\text{SiO}_2$  layer created via slow thermal oxidation allows for tight control of the nanochannels dimension. The poly-Si is used as a distributed gate electrode that extends for the whole nanochannels area to offer high electrostatic gating performances. External connection to the poly-Si layer is possible through the conductive pads at the edge of the chip (Figure 3.8A). The outer-most layer of a-SiC forms an excellent bio-inert coating, while serving as an insulating layer for the gate electrodes.

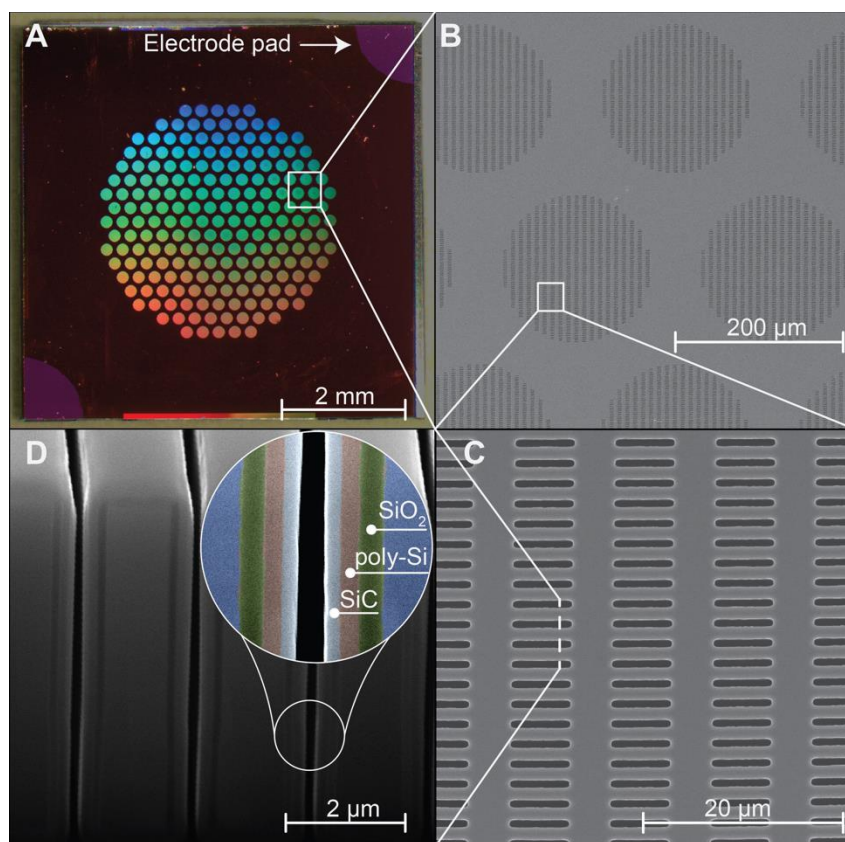


**Figure 3. 8:** Nanofluidic membrane. A) Picture of the nanofluidic membrane which measure 6 mm x 6 mm with a total thickness of 400  $\mu\text{m}$ . B) SEM image of the top face of the membrane (device layer) that shows the vertically etched nanochannels arranged in circles. C) SEM image of nanochannels array. D) FIB-SEM image of nanochannel cross-section which shows the vertical nanochannels and highlight the layer stack on the nanochannels walls. In order from the innermost (Silicon, blue) to the outermost layer there is silicon dioxide ( $\text{SiO}_2$ , 175 nm, green), n-doped polycrystalline silicon (poly-Si, 121 nm, red) and silicon carbide (SiC, 64 nm, gray). The different layers in the FIB image are artificially colored for clarity.

### 3.3.2 EDX, and Ellipsometry Measurements

The composition of the external coating layer a-SiC was investigated by using the EDAX measurements on three membranes located in four different spots of the wafer to assess the fabrication process. The results relative to one measurement is reported in Figure 3.9.

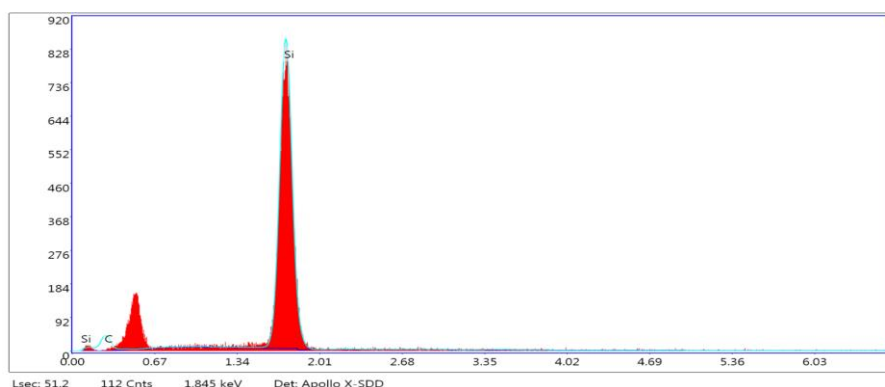


**Figure 3. 9:** EDX measurement relative to one membrane.

The deposited a-SiC layer featured  $51.47 \pm 1.95$  wt% of silicon (Si),  $14.22 \pm 1.95$  wt% of carbon (C), and  $34.30 \pm 2.05$  wt% of oxygen (O). The low standard deviations associated with the elements indicated that the deposition process was uniform. Simultaneously to the detection of the Si and C, O was detected. The presence of the O can be associated to native oxide. In fact, every silicon substratum exposed to the atmosphere naturally develop a thin layer of oxide, between 3 nm to 5 nm thick.

To measure the thickness of the deposited polysilicon and s-SiC, ellipsometric measurements was performed on four membranes located in different spots of the wafer and reported in Figure 3.10. The data were fitted in the range of the wavelength 270 – 1000 nm and averaged. The averaged thickness and standard deviation of the layers was calculated: the polysilicon was estimated  $121.98 \pm 12.3$  nm, while the a-SiC was estimated  $64.22 \pm 15.2$  nm.

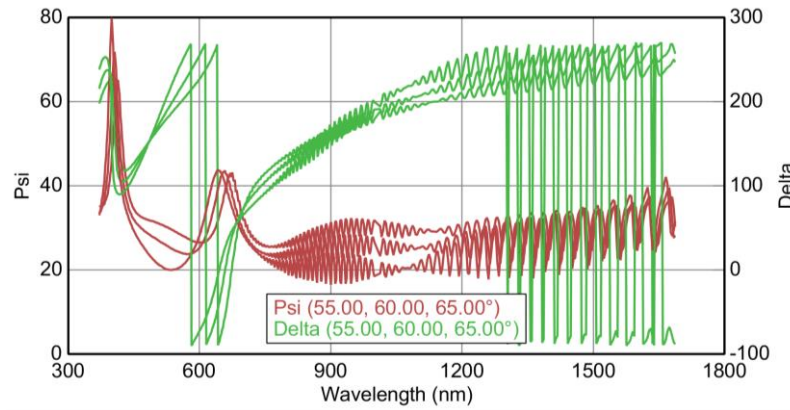


**Figure 3. 10:** Variable Angle Spectroscopic Ellipsometric Data relative to one membrane.

### 3.3.3 Mechanical Robustness and Nanochannel Dimension Tests

The Gas test characterization was performed on the diced chips, to measure the nanochannels dimensions. After the evaluation of the nanochannel size using the Scanning Electron Microscopy, and the after performing a first investigation of the vertical channel section by mean of the Focus Ion Beam of some of the nanochannel membrane, the nitrogen gas test allowed to measures the nanochannel size of the all membranes deriving from the wafer. In fact, the photolithographic process performed could provide a variation in terms of size of nanochannels despite the nanofluidic membranes were fabricated on the same SOI wafer. For each SOI wafer, the nanochannels size was estimated as an average measure. The average measure calculated on the same SOI wafer associated with a standard deviation that was comprised in the range of  $\pm 120$  nm.

## 3.4 Conclusion

As compared to our previous technology[19,22,44] the present membrane presents two key advantages: i) the streamlined fluidic structure, with cylindrical microchannels directly connected to the array of through nanochannels allows for a substantially simplified fabrication process[22]; ii) by accounting for same nanochannel size, the fluidic architecture achieves a 45% and 37% reduction in diffusive length and resistance, respectively. As compared to other AAO-based

gating systems[122], which dispersed pores size can affect performances[123], the present membrane possesses monodispersed channel dimensions. This is important in the context of the tight control of drug delivery. Further, in contrast to most gated fluidic systems, designed for the evaluation of electrostatic phenomena[124], our technology achieves molecular transport rates suitable for medical applications.

---

## Chapter 4

# In-Vitro Degradation Study

### Abstract

In this chapter, the a-SiC was investigated in comparison with the silicon dioxide SiO<sub>2</sub>, the most used material in solid-electronics. The evaluation was performed by using different techniques to observe the corrosion effect on the surface of the nanofluidic membrane. Results demonstrated that the a-SiC is an ideal candidate for harsh environment, since it demonstrated greater stability and no evidence of degradation.

## 4.1 Introduction

The silicon manufacturing use materials that have been demonstrated to be biocompatible[73,75]. The nanofluidic membrane was fabricated by using amorphous silicon carbide, that insulate the embedded electrode. At the same time, the biocompatibility of the a-SiC allowed low immunity reaction[82] generated on the implantation site of the nanofluidic device.

### 4.1.1 Scanning Electron Microscopy

The Scanning Electron Microscopy (SEM) consents to investigate physical characteristics of specimens, and to gather information regarding the surface and the near surface area in the bulk material, as the structure, the composition and the defects of the sample. This investigation is performed by using an electron beam with small wavelength and a high energy, and this permits to reach an extremely high resolution that can reach the limits lower than 1 nm.

The ability to resolve the images is determined by the wavelength used to inspect the samples. In fact, considering the visible light that presents a large wavelength ( $\lambda=380-760\text{nm}$ ), the achievable resolution is 200  $\mu\text{m}$ . In case the wavelength used is shorter, as in case of ultraviolet light, then the resolution can be enhanced. In fact, considering the use of a lens in contact with a dielectric with high refractive index as for a lens immersed in oil, the resolution reaches the limit of 0.1  $\mu\text{m}$ . Significant improvements are reached in case the wavelength used is even smaller, since the generated power is increased and the image depicts more details.

Formation of the image. The SEM instrument is composed by three units: an electron column, a vacuum chamber to host the samples, and an electronic control. The electron beam occurs in the electron gun situated in the upper part of the electron column, and it is gathered into system of electromagnetic lenses that generate a beam exhibiting a diameter of few micrometers. The collision between the electron beam and the surface of the specimen produces a several different signals associated with backscattered electrons, secondary electrons, auger electrons and x-ray. Additionally, depending of the accelerated voltage used, the

electron beam can enter through the surface and reach the substrate of the sample. The depth of penetration, that usually is few  $\mu\text{m}$ , is determined by the density of the material under inspection and the acceleration voltage of the electron beam. In fact, the collision between the electrons and the surface produces a scattering phenomenon that can be elastic and inelastic. Figure 4.1 the scattering signals and their penetration depth. The elastic scattering redirects the hitting electrons into new coordinates preserving the same amount of energy. This event causes the propagation of the electrons inside the bulk material in a teardrop formation. This type of scattering occurs with a bias voltage of 5 – 20 kV. On the other hand, during the inelastic scattering, energy is transferred to the nucleus of the atoms, but the direction of propagation is kept as the original incident direction, or it can vary with small angles respect the original one.

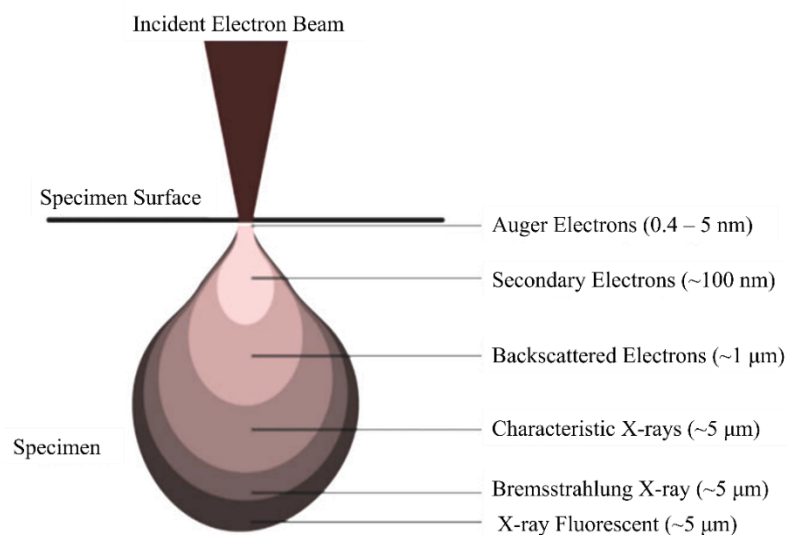


**Figure 4. 1:** Teardrop generated by the collision of the incident electron beam and the specimen surface. The generated scattering signals and their penetration depths are illustrated.

The information that one can gather from the imaging are different. It is possible to observe the superficial micro- and nano-structure of the specimens for a variety of materials, from inorganics, such as metals, ceramics, compounds, to organics, such as biological specimens, among others. Additionally, the specimens can be or not be conductive.



The resolution offered is in less than 1 nm, and in case of SEM structure provided with field emission gun, the sample can be investigated with a lateral spatial resolution of 1 nm. SEM imaging can be obtained by using both type of electrons: secondary or backscattered electrons. In the first case, the imaging is used to provide topographic images, while in the second can provide a compositional description simultaneously to the topographic images.

#### 4.1.2 Energy Dispersive X-ray Spectroscopy

The electron beam can be generated using two types of guns: thermionic or field emission. The generated electrons are accelerated by using a bias voltage, and the focused into a beam through electromagnetic lenses. Signals generated by the collisions can be of different types, i.e. the secondary and the backscattered electrons, auger electrons, characteristic x-ray and photons. The signals originated from the interaction that occurs between the sample and the beam provides information regarding the sample composition.

The Energy Dispersive X-ray spectroscopy is employed to examine the qualitative and quantitative elemental composition of the specimens[125]. The working principle of the EDX spectroscopy can be explained considering the atomic model reported in Figure 4.2. The atom nuclei, where the protons and neutrons are located, presents a positive charge due to its composition. Electrons on the orbits carrying negative charges are placed on specific shells depending on their energy that increases as the distance from the nucleus increase.

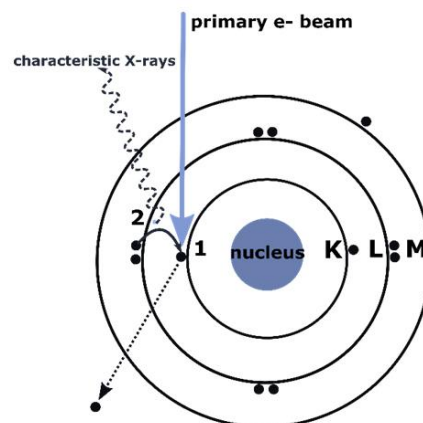


**Figure 4. 2:** Atomic model displaying the shells K, L, and M.

As the electron beam hits the surface of the material, the interaction between accelerated electron and the atoms takes place in the inner shell. The electron placed on this shell is bounced to the next orbital and a vacancy take its place, ionizing the atom. The vacancy is occupied again as soon as an electron from outer orbits collapse into inner orbit, causing the release of an x-ray photon provided with the energy corresponding to the energetic difference of the two orbits. In Figure 4.2 is reported the atom with its shells hit by the electron beam and the generated characteristic x-ray.

This results in an electromagnetic emission spectrum with unique set of peaks[125], which represent the main purpose of the spectroscopic investigation. The position of the peaks is determined by the Moseley's Law[126].

#### **4.1.3 FIB Focus Ion Beam**

The focus ion beam microscopy employs ions beam to raster the surface of the sample. The ions hitting the specimens generate secondary ions and electrons that provide information as in case of SEM, but the resolution is limited to 5 nm. The FIB is usually performed to micromachining, etching or sputtering the specimens. Since the positively charged ions exhibit a momentum and a weight larger than electrons, the ion beam can eliminate matter from the surface of the sample without damaging the underside substrate with nanometric precision.

The interactions between ions and surfaces consists in transferring the ionic energy and momentum to the surface of the specimen. As in case of the SEM, the collision can be elastic and inelastic. In first case, the elastic collision can originate the displacement of atoms from their original position, and this led to the damage of the sample. In case of inelastic interactions, it is possible to observe electromagnetic and radiation emission of electrons and ions. There is three type of ion supplies: the liquid metal, gas field and plasma ion source. One of the most used ionic sources is the liquid metal gallium, since it exhibits a low melting point, high stability and reduced energy spread.

The ionic imaging is performed as in case of the SEM imaging. While in the scanning electron microscopy the image is generated by the secondary electrons or

backscattered electrons, in the FIB microscopy technique, the secondary electrons generated by ions collision possess lower energy. In fact, by using a gallium ionic beam, the energy associated with Gallium comprised between of 5 kV to 30 keV can generate secondary electrons that feature an energy 10 eV.

#### **4.1.4 Atomic Force Microscopy**

The Atomic Force Microscopy (AFM) is one of the scanning probe microscopies that can provide a very-high-resolution measurements of the surfaces of the specimens under test. It has a resolution of order of fraction of nanometer, and can give a topological map of the surface of the sample under test. Information deriving from the measurements are generated by a mechanical probe put in direct contact with the specimen surface. This probe is a piezoelectric element driven by electronic command and control that provide a high accurate and precise scanning.

The information that one can gather from a measurement are regarding the force measurements, the topographic imaging, and the manipulation. In force measurement mode, the AFM scan can evaluate the forces generated by the mutual interaction of the probe and the specimen. Specifically, the probe demonstrates high sensibility toward the forces offered by the specimen surface. This interaction produces a raster scanning image where the variation in height of the sample are recorded due to the contact probe-specimen. This principle can be used to evaluate the mechanical properties, i.e., the Young's modulus, that is related to the stiffness of the solid material specimen[127]. The surface topography can be displayed in a pseudo-colored, where the different color indicates different height level of the surface. In manipulation mode, the interaction between the probe and the sample is employed to modify the features of the specimen in a precise fashion, as in case of photolithographic processes AFM scanning probe based and atomic modification of the surface specimen, and biological application, as in case of localized cells stimuli. AFM investigation permits to acquire other type of information, as the stiffness of adhesion strength, electrical conductivity and surface potential of the specimens, among other properties.

### 4.1.5 Spectroscopic Ellipsometry

Spectroscopic ellipsometry is an optical tool that evaluate the variation in reflection or transmission polarization signal by comparing to a model[128,129]. This technique is widely used to investigate properties associated with thin film, as for example the thickness or depth of the film, the doping composition, the roughness, the electrical conductivity, the crystallinity of the film, among others.

The incident light beam that interacts with the thin film generate a spectral data depending on the returning component of the reflected light beam. The interference resulting from the interaction of the reflected light through the different layers can be constructive and destructive. The type of interactions is determined by the light wavelength and by the phase of each light component. Additionally, the reflected light exhibits a delay depending on the thickness of the layer and the refractive index of the material. For this reason, the measurements generate data depending on the properties of the layer.

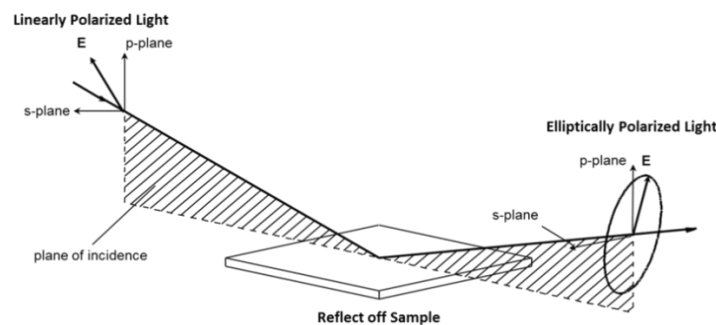


**Figure 4. 3:** Ellipsometric measurement principle. Polarization light is reflected by the specimen.

## 4.2 Materials and Methods

### 4.2.1 Membrane degradation

To test the inertness of the membrane in view of implantable applications, an in-vitro study in simulated physiological conditions at 37 °C as well as in accelerated conditions at 77 °C was performed. Two sets of membranes were used: 1) in the first set, the fabrication procedure was stopped at the thermal oxidation (Set A),

resulting in the outmost layer of SiO<sub>2</sub> (~300 nm), 2) the second set of membranes (Set B) featured an outmost layer of SiC (~70 nm), which was deposited as previously described right after SiO<sub>2</sub> (~270 nm) thermal growth. Each set of membranes was divided into 3 groups: the first group was soaked in 4 mL of 2 μM sodium fluoride (NaF) in PBS at 77°C, the second group was soaked in the same solution at 37°C and the third group – in 2 μM NaF in PBS also containing 16 mg/mL BSA at 37°C. This resulted in a total of 6 groups with n = 4 replicates for each. To prevent exposure of SiO<sub>2</sub> from the side in the Set B, the sides of each membrane was covered with thermal epoxy (354-T Epoxy Technologies, Inc.) and cured at 150°C for 30 minutes.

The degradation study was run for a total of 120 days with timepoints every 15 to 30 days depending on the group. At each timepoint, the membranes were removed from the solution and triple rinsed in deionized water (DI H<sub>2</sub>O) followed by isopropyl alcohol (IPA) before being dried. To assess degradation, the surface roughness, surface composition and thickness of the different layers were evaluated using electronic and optical tools.

#### **4.2.2 Spectroscopic Ellipsometry**

The thickness of the coating thin films was measured by spectroscopic ellipsometry technique using the J.A.Woollam M2000U Ellipsometer in the spectral range of 245 - 900 nm. All the spectra were recorded at room temperature, using three incident angles of 55 °C, 60 °C, and 65 °C.  $\psi$  and  $\Delta$  were recorded in standard mode, by using the configuration of 0 ° for the modulator, and 45° for the polarizer. To fit the experimental measured data, appropriate optical fitting models were developed for the silicon dioxide and amorphous silicon carbide samples. The spectral range for the evaluation of the thickness of the coating films and the surface condition was chosen between 370 – 1000 nm.

#### **4.2.3 SEM, and EDX**

To perform a visual inspection and the chemical modification, the specimens were inspected by SEM and EDX techniques. The SEM used for investigation was

a Nava Nano SEM 230 (Thermal Fisher, USA) and the EDX Detector mounted on the side of the SEM is EDAX-Octane Super device (AMETEK, Inc. USA). Measurements were performed at room temperature 23 °C. The SEM accelerator voltage was set at 5 kV and 8 kV for SiO<sub>2</sub> samples and a-SiC samples, respectively. The high vacuum chamber was set at  $3 \times 10^{-6}$  Torr. The spot was set at 3 nm for imaging, since the diameter of the e-beam was 3 nm. The emission imaging mode was set to process the imaging and to have the high-resolution image. The SEM work distance was set at 5 mm.

To perform the EDX investigation, the accelerator voltage, the working distance and the vacuum conditions were maintained the same of the SEM investigation.

#### 4.2.4 AFM

To study the surface morphology, an atomic force microscope (AFM Catalyst) operating in contact mode was used. In Contact mode, the micrometer-scale allowed an investigation of 50  $\mu\text{m}$  x 50  $\mu\text{m}$ . Measurements were performed with a diamond conductive coated probe.

### 4.3 Results

**Degradation study.** In vitro degradation testing was performed to evaluate the membrane chemical robustness in view of its application for implantable drug delivery. The testing conditions in PBS at 37 °C were chosen as they represent an established model of biological fluids in subcutaneous tissues. Accelerated conditions at 77 °C allowed us to monitor long-term degradation within a shorter timeframe, while maintaining relevance with respect to the physiologic conditions. Moreover, because fluoride ions are known to readily erode various types of silicon containing materials, the stability of the membrane was tested in solutions containing NaF. Fluoride is present in small quantities in drinking water as well as in physiological fluids. Importantly, in humans, fluoride ions are not regulated homeostatically and fluoride concentration in plasma averages at 0.01 ppm[130]. For this reason, the solution used contained almost 4 times the average fluoride concentration found in human plasma (2  $\mu\text{M}$ ).

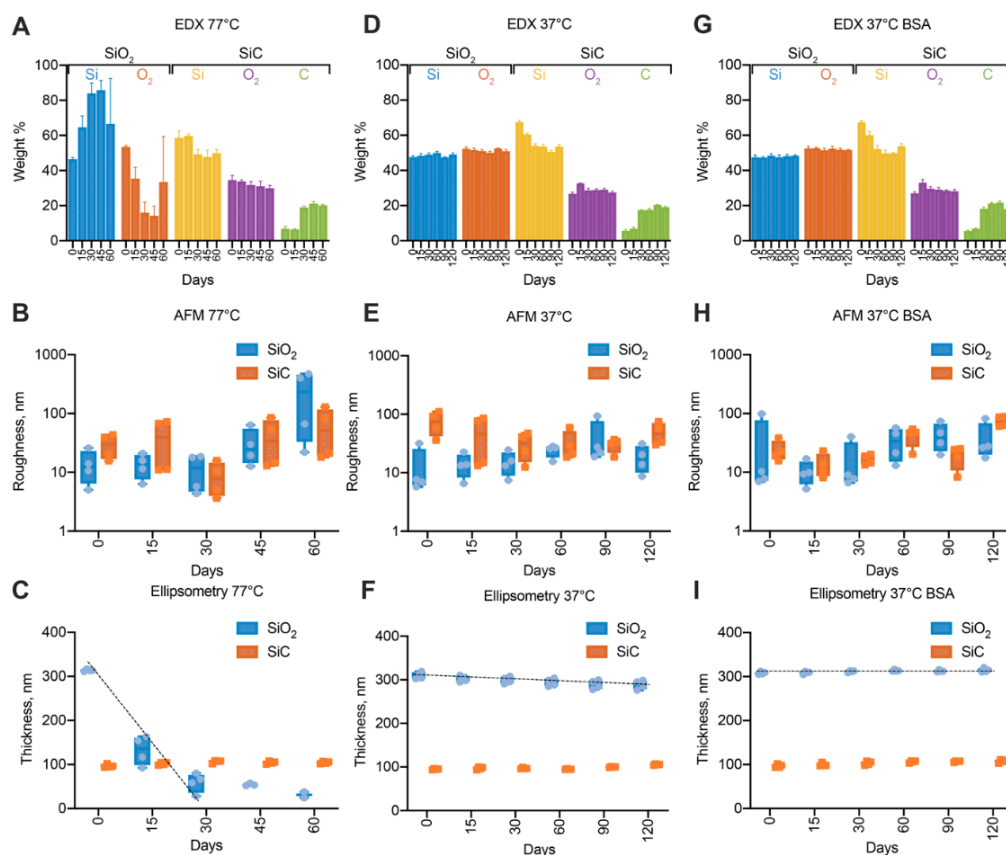


**Figure 4. 4:** Nanofluidic membrane degradation. Energy-dispersive X-ray spectroscopy (EDX) for membranes coated with SiO<sub>2</sub> versus SiC at 77 °C (A), 37 °C (D) and at 37 °C with BSA (G). Surface roughness calculated with atomic force microscopy (AFM) for membranes coated with SiO<sub>2</sub> versus SiC at 77 °C (B), 37 °C (E) and at 37 °C with BSA (H). Layer thicknesses fitted through ellipsometry data for membranes coated with SiO<sub>2</sub> versus SiC at 77 °C (C), 37 °C (F) and at 37 °C with BSA (I).

Figure 4.5 A, D, G show the surface composition of the chips analyzed through energy dispersive X-ray spectroscopy (EDX). For SiO<sub>2</sub> chips in accelerated conditions (Figure 4.5A), the relative abundance of silicon and oxygen peaks significantly changed during the first 30 days, resulting in an increasing trend of silicon presence. EDX analyses a volume deeper than the thickness of our SiO<sub>2</sub> layer, including the underlying silicon. Therefore, the shift in composition toward silicon suggests an erosion of the initial SiO<sub>2</sub> layer (~300 nm). The reduction in silicon oxide thickness was corroborated by ellipsometry measurements (Figure 4.5C), which show a constant decreasing trend. However, surface roughness

(Figure 4.5B) did not show any significant changes during the first 30 days, hinting small to no change in solid-liquid interface composition. Interpolation of the ellipsometry measurements during the first 30 days yields a corrosion rate of 8.5 nm/day, which predicts the complete degradation of the silicon oxide layer in ~35 days. In fact, the surface roughness (Figure 4.5B) increases after day 30 suggesting a change in surface composition, likely due to a change in exposed surface from silicon oxide to silicon. The presence of oxygen in the EDX for the 45 and 60 days timepoints does not exclude the hypothesis that the thermal grown oxide is completely corroded. This can be explained by the formation of Si-O-Si bonds that occurs due to nucleophilic attack of oxygen from OH-terminated Si to nearby surface Si atoms with dangling bonds[131]. The silicon surface is concurrently oxidized and hydrolyzed by the surrounding water. The rate of this corrosion process is likely higher than the silicon oxide corrosion rate, resulting in an increased surface roughness as reported by the AFM measurements (Figure 4.5B).

In contrast with SiO<sub>2</sub> coating, membranes presenting a SiC outmost layer did not show appreciable trends of degradation (Figure 4.5A-C). The thickness of SiC measured with ellipsometry (Figure 4.5C) was constant over the whole duration of the experiment, demonstrating inertness of SiC in electrolytic solutions, even in the presence of fluoride ions. It should be noted that EDX revealed a sharp increase in abundance of carbon concurrent with the reduction of silicon at 30 days (Figure 4.5A). Due to the abrupt rather than continuous change and the absence of carbon source, I attribute this observation to a poor fitting of the EDX spectrum which suffers from suboptimal signal-to-noise ratio.

No notable trends were observed in either the surface composition or roughness at 37 °C (Figure 4.5D, E). However, the thickness of the silica layer was slowly decreasing as evident by ellipsometry (Figure 4.5F). The degradation rate was obtained by fitting the data points and is equal to 0.17 nm/day. To evaluate the effect of the addition of fluorine ions on degradation, the temperature coefficient ( $\gamma$ ) of silica degradation was calculated by assuming linear degradation kinetics and adopting the Arrhenius equation[132]. Assuming that the degradation kinetics are linear in time, it was used the degradation rate constants at 37° C and 77°C in Arrhenius equation to determine the temperature coefficient ( $\gamma$ ) of silica layer degradation[132]:



$$k_{t2} = k_{t1} * \gamma^{\frac{\Delta t}{10}} \quad (4.1)$$

$$\gamma = \left( \frac{8.5 \text{ nm/day}}{0.17 \text{ nm/day}} \right)^{\frac{10}{77^{\circ}\text{C} - 37^{\circ}\text{C}}} \cong 2.7 \quad (4.2)$$

Temperature coefficients for corrosion reactions are usually in the range of 2-2.3. However, particular experimental conditions can lead to values outside this range[133]. In fact, previous studies of silica and quartz degradation have found coefficients between 1.7 and 3.7 depending on the temperature range considered and solution properties such as molarity and pH[134]. Therefore, in order to correctly estimate degradation times extrapolated from accelerated conditions studies, the  $\gamma$  for specific experimental conditions must be calculated. The  $\gamma$  experimentally found in this study (2.7) is within what was previously found in literature. Comparison to other studies on dissolution rate of silica[134] showed that the presence of  $\text{F}^-$  in solution increases the degradation rate by factor of 24 at 37 °C and by factor of 50 at 77°C (No  $\text{F}^-$  at 77 °C vs  $\text{F}^-$  at 77 °C).

A higher value than reported in the literature (typically  $\gamma=2-2.3$ )[135] was obtained ( $\gamma=2.7$ ), which is indicative of the harsher degradation conditions generated by fluorine ions. Even in this setting, a-SiC coated membrane showed no sign of degradation, demonstrating superior chemical inertness and suitability for long-term implantable applications.

Further, the influence of protein adsorption on surface degradation (Figure 4.5G, H, I) was investigated. Membranes were incubated at 37 °C in PBS solution containing 1.6% BSA, concentration compatible to what previously reported in the subcutaneous space[136,136]. Ellipsometry measurements showed no evidence of surface silica loss throughout the whole duration of the experiment. While in solution, BSA adsorbs to the silica surface, creating a uniform layer that has been reported to exhibit properties typical of BSA[137]. In these conditions the adsorbate masks the silica properties and limits the diffusive access of water to the surface. Thus, protecting the underlying silica from corrosion[131].

## 4.4 Conclusion

In this chapter, the corrosion evaluation of the a-SiC was presented in comparison with the silicon dioxide. Overall, the investigation demonstrated that the silicon oxide erodes at appreciable rate in the absence of proteins at 37 °C and very fast at 77 °C. Despite the spontaneous formation of protective protein layer, it is not reliable for long term use in vivo. In contrast, silicon carbide showed superior stability and no evidence of degradation was observed across all tested conditions, including incubation in 2  $\mu$ M fluoride buffer at 77 °C.

---

## Chapter 5

# Electrochemical characterization of the nanofluidic membrane as homogeneous IFET nanochannels

### Abstract

In this chapter, the performances of the gated membrane for electrostatic control of charged species were evaluated. The gating performances of the nanofluidic membrane were evaluated by applying an electrostatic potential (-3 V to 3 V) to the gated nanochannels. I-V characteristics were measured potassium chloride (KCl) aqueous solution to assess the ionic field effect transistor IFET permselectivity of the nanofluidic membrane. Additionally, the performances were evaluated where the ionic Debye length is smaller than the nanochannel size, in light of future biomedical applications such as reservoir-based implants. Furthermore, the leakage current was measured in the phosphate buffer saline (PBS) solution at different concentrations. The physics of the devices was investigated and the transport phenomena responsible for the leakage current were identified. A small-signal linear time-invariant (LTI) circuit was determined and the flat band potential and density of interface states were estimated.

## 5.1 Introduction

### 5.1.1 Physical theory of conductivity in amorphous material

The nanochannels are provided with a doped layer of polycrystalline silicon coated with a layer of amorphous silicon carbide. This structure represents the gating electrode of the nanofluidic membrane. The amorphous status of the dielectric coating could be subjected to phenomena of electric transports through the density of distribution of states generated during the deposition process.

The physical properties of the solid materials are related to their electronic band gaps. Crystalline materials present valence band, conduction band, and forbidden energy gap that are responsible for the electronic transport and conductive properties. On the other hand, the amorphous materials still exhibit electrical properties similar to intrinsic semiconductor materials, but they also feature bandgap between occupied and unoccupied states, as it can be observed in crystalline semiconductors or dielectric insulator.

The conduction theory of the bandgap in crystalline and insulator material was firstly described by Wilson[138–140], and it stated that the electronic charges can freely move in the crystalline lattice, occupying specific energetic states that can relate to the Bragg reflection condition. To observe the electronic conduction, i.e., current, the electron must possess an energy that allow him to move from the valence band  $E_V$  to the conduction band  $E_C$ . A schematic diagram representing the conduction theory is reported in Figure 5.1.

In an insulator material, all states in the conduction band are all vacant, while the states in the valence band are full, impeding the generation of electronic transport and the generation of current.

A key role in the electronic conduction mechanism is played by the Fermi level position, the trapping phenomenon, the minority carriers, the bending occurring at the junction with other materials, the impurities as well as the distribution of the of states.

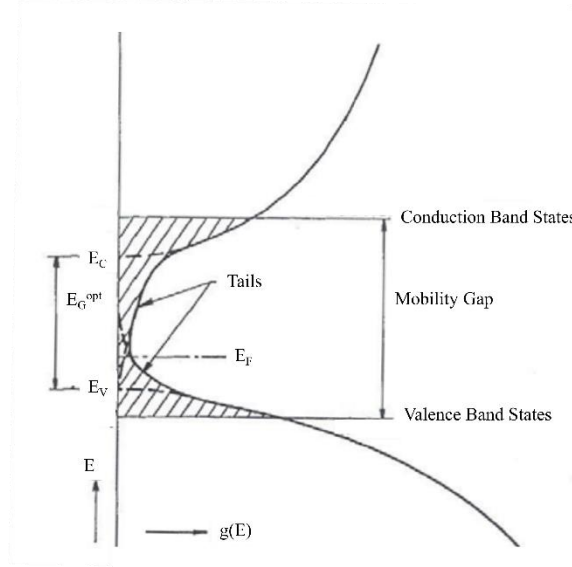


**Figure 5. 1:** Electronic density of states in amorphous silicon carbide.

The electronic distribution of the density of states represents one of the most important aspect in the electrical conductivity on the amorphous semiconductor[141]. It can be divided in localized density of states and extended density of state. They concur in the conductivity of current depending on the temperature. In fact, when the temperature is 0 °K electronic conduction involves only the extended states.

The electrical conductivity  $\sigma$  of the amorphous material can be described by the equation 5.1:

$$\sigma = ne\mu \quad (5.1)$$

where  $n$  represents the carrier density, and  $\mu$  represent the electronic carrier mobility. Considering that the electrical conductivity can be expressed as the contribution of the electrons featuring an energy above the Fermi energy  $E_F$  and the holes featuring an energy below the Fermi energy  $E_F$ , it is possible to describe the conductivity as

$$\sigma = \int N(E) e \mu(E) f(E, T) dE \quad (5.2)$$

where  $f(E, T)$  represent the Fermi function,  $N(E)$  represents the total amount of minority carriers and  $\mu(E)$  represents the carrier mobility, and all those quantities are function of the energy. Considering the particular case when the conductivity involves only one type of carriers, then the equation 5.3 can be rewritten as

$$\sigma = \int N(E) e \mu(E) \exp \left[ -\frac{(E - E_F)}{kT} \right] dE = \frac{1}{kT} \int \sigma(E) \exp \left[ -\frac{(E - E_F)}{kT} \right] dE \quad (5.3)$$

where  $k$  is the Boltzmann's constant,  $T$  is the temperature, and  $\sigma(E) = N(E) e \mu(E) kT$  denotes the conductivity at  $E = E_F$ . The equation highlights that the conductivity is dependent on the density of state and on the carrier mobility. For this reason, the density of defects that could appears into the bandgap can generate a mechanism of conduction by hopping transport at the Fermi level, as reported in Figure 5.2.

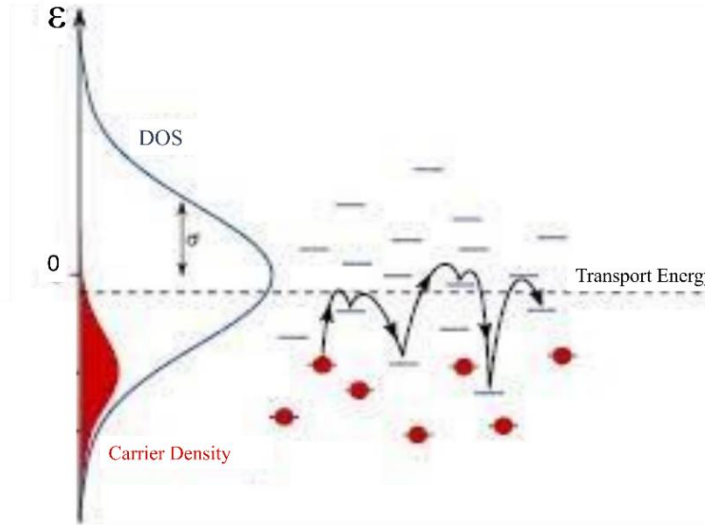


**Figure 5. 2:** Conduction mechanism associated to the hopping transport.

To avoid the hopping effect, it is convenient to produce materials with a low amount of defect. In this way, the conduction mechanism is originated only in the band edges. In fact, the carriers involved in the conduction process possess a higher energy level that permits the to “jump” to the conduction band if compared to the

ones involved in the hopping effects. This guarantees more control over the generation of current and the conduction mechanism.

When the temperature is above the 0 °K, the carriers are free to move in extended states and additionally, in the localized state by the hopping mechanism. Furthermore, when the material presents any inhomogeneity, the carriers are subjected to elastic and inelastic movements. For this reason, the conductivity of the material can be evaluated as an average of local conductivity values calculated over the density of states.

**Activation Energy.** The mechanism of conduction in amorphous materials is thermally stimulated, and can be defined with the equation 5.4:

$$\sigma(T) = \sigma_0 \exp\left(\frac{-E_\sigma}{kT}\right) = \sigma_0 \exp\left(-\frac{(E_{TR} - E_F)}{kT}\right) \quad (5.4)$$

where  $E_{TR}$  represents the average energy of the conduction electrons,  $E_\sigma$  represents the activation energy and  $\sigma_0$  represent the conductivity pre-factor. Considering the conductivity model for *abrupt mobility edge*, where the transport mechanism involves the conduction and valence bands,  $E_{TR}$  correspond to the conduction energy  $E_C$ . Considering other conduction mechanisms, for instance the *band tail hopping*, the  $E_{TR}$  can be different from  $E_C$ . The distribution of states, the activation energy  $E_{TR}$ , and the band tail mechanism are reported in Figure 5.3.

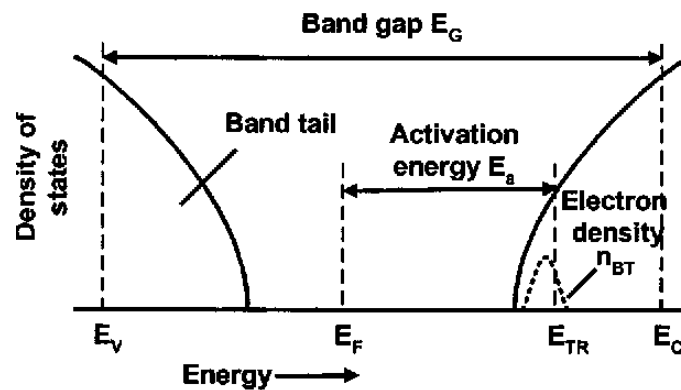


**Figure 5. 3:** Schematic reporting the density of state, the abrupt conduction mechanism, the band tail hopping , as function of the energy. Fermi energy  $E_F$ , activation energy  $E_\sigma$ , and average conduction energy  $E_{TR}$  are reported.

### 5.1.2 Electrical properties of the amorphous/crystalline heterojunction

The electrode is composed by the phosphorous doped polysilicon covered with a thin layer of a-SiC. The composition of the amorphous silicon carbide represents an important aspect for the electrical properties. Based on the ratio between the carbon and the silicon, the obtained amorphous silicon carbide exhibits different conductivities[142]. Additionally, the interface between polysilicon and a-SiC can originate a space charge region. The space charge region is characterized by the presence of free and trapped charges that can increase the conductivity. Polycrystalline silicon is doped by adding phosphorous atoms, generating a n-type semiconductor. The excess of electrons results in an energy level  $E_F$  closer to the conduction band  $E_C$ . Consequently, they can be easily excited by applying an appropriate potential, and involved in the conduction mechanism.

## 5.2 Materials and Methods

### 5.2.1 Electrolytic solutions

The dielectric leakage currents were evaluated using two different aqueous solution: the KCl and the PBS. The employment of the monovalent solution KCl allowed to characterize the nanofluidic membrane as an IFET. Instead, the PBS solution at different concentration permitted to evaluate the leakage current when the nanofluidic device would be implanted. In fact, the pharmaceuticals used to perform experimental control for the release of drugs in in-vitro fixture were dissolved in PBS, the physiological solution used for in-vivo experiments. Further details regarding the in-vitro electrostatic control of the pharmaceuticals are provided in Chapter 6.

### 5.2.2 Setup for electrochemical measurements

The Setup for the electrochemical measurements is reported in Figure 5.4. Electrochemical measurements were performed in a poly(methyl methacrylate)



PMMA (McMaster Carr, Douglasville, GA) fixture. The setup system was constituted by two reservoirs containing 2 mL of solution, each provided with two Ag/AgCl electrodes (counter electrode and reference electrode). The under-testing samples (membranes and blank) were secured in between the two reservoirs by using two rubber silicone O-rings (Apple Rubber, Lancaster, NY). The fixture was screwed by a mean of 4 SS316L M3 screws. All measurements were performed using the potentiostat multichannel (Ivium Technologies B.V.).

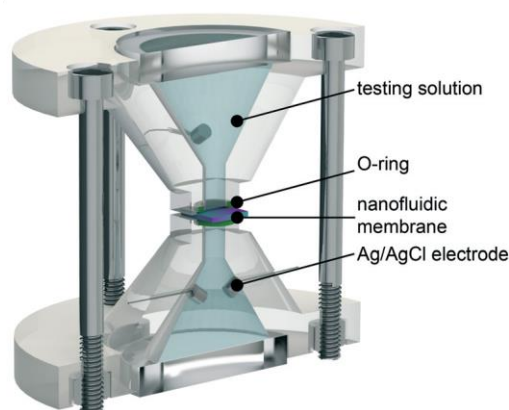


**Figure 5. 4:** Assembled system setup to perform electrochemical measurements. The membrane separates the two reservoirs containing two Ag/AgCl electrodes. Reservoirs are called Source (S) and Drain (D).  $V_{DS}$  is the transmembrane potential, and  $V_{GS}$  are the polarization potential.

### 5.2.3 Nanofluidic membrane

The nanofluidic membrane used to electrochemically characterization was fabricated as described in Chapter 3. Briefly, the lithographic fabrication process was performed on a silicon-on-insulator (SOI) 4-inch (100)-oriented p-doped wafer with a device layer ( $15 \pm 1 \mu\text{m}$ ), a buried oxide layer ( $1 \mu\text{m}$ ), and a handle wafer ( $400 \mu\text{m}$ , Ultrasil Corporation Hayward, CA). After a first wet thermal oxidation step to produce 600 nm of sacrificial oxide on the surface of the device layer, nanoslit templates with a 500 nm width and a 6  $\mu\text{m}$  length were patterned by using a reactive ion etching (RIE) step via inductively coupled plasma (ICP) deep silicon etching. On the other side of the SOI wafer, the handle wafer was patterned with a

high density of hexagonal arranged circular microchannels by ICP to provide mechanical stability. Then, the built-up polymer covering the nanochannels and microchannels was cleaned, and the buried thermal oxide layer was removed in a buffered oxide etchant (BOE) solution. Nanochannels were shrunk by growing a layer of SiO<sub>2</sub> through wet thermal oxidation. To build the buried gate electrode, a low-pressure chemical vapor deposition (LPCVD) step allowed the deposition of 121 nm of phosphorus-doped polysilicon (poly-Si) over the surface of the nanochannels. A further plasma-enhanced chemical vapor deposition (PECVD) step coated all of the wafer with a 64 nm a-SiC dielectric layer. Two contact pads (1 x 1 mm<sup>2</sup>) were created by selective removal of a-SiC by fluorine-based RIE at the edge of the membrane to expose the doped poly-Si. One hundred twenty total membranes were diced into 6 x 6 mm<sup>2</sup> pieces using a dicing saw. Each membrane presents 199 microchannels organized in a hexagonal spatial configuration. Each microchannel is connected to 1400 identical slit nanochannels arranged in 19 rows and 96 columns, and consequently, the membrane chip features 278600 nanochannels.

#### **5.2.4 Planar gate electrode fabrication**

A planar gate electrode was reproduced on the same type of wafer by following the same photolithographic process. Briefly, the 4-inch p-doped SOI wafer underwent a wet thermal oxidation step producing a layer of SiO<sub>2</sub>. Then, the gate electrode was obtained via LCPVD deposition of 121 nm of phosphorous doped poly-Si. The wafer was diced in half before proceeding to the coating with dielectric. On a half wafer, a PECVD step deposited a-SiC dielectric coating, and on the other half of the wafer, a wet thermal oxidation step produced a SiO<sub>2</sub> coating. The contact pads for the poly-Si were created by selective removing the dielectrics by fluorine-based RIE at the edge of the blanks. Each half-wafer hosted sixty 6 x 6 mm<sup>2</sup> blank diced via dicing saw.

### 5.2.5 Electrode connection

One contact pad exposing the poly-Si was connected to an insulated high-temperature 36 AWG wire via conductive silver epoxy (H20E, Epoxy Technology, MA) and underwent a 1-hour curing step at 150 °C. The conductive exposed connection was isolated with UV epoxy (OG116, Epoxy Technologies, Inc.) and cured via UV for 2 hours.

### 5.2.6 Conductance, current-voltage (I-V) curves, and leakage current

Electrochemical characterization of the nanochannels was performed in a KCl solution. The conductance was measured in a 4-electrode configuration using different concentrations of KCl, ranging from  $10^{-7}$  M to  $10^1$  M. A potential across the membrane, also called the transmembrane potential (VDS), was applied using one channel of the potentiostat (Ivium Multichannels). To monitor the transmembrane current IDS, a staircase of 250 mV steps was applied from -1 V to 1 V in a 4-electrode configuration, and each step was held for 30 s to overcome transient phenomena. The conductance was calculated by taking the last sample point of each step and averaging the measured values. We repeated measurements per membrane three times, and the complete study was performed on three membranes. During the conductance measurements, a gate potential was not applied.

The I-V characteristics and leakage current were evaluated in  $10^{-5}$  M KCl and  $10^{-4}$  M KCl. A voltage across the membrane (VDS) and a voltage on the gate electrode of the membrane (VGS) were applied using two channels of the potentiostat (Ivium Multichannels) to monitor the transmembrane current IDS and the leakage current IGS in parallel. To monitor IDS, a staircase of 250 mV steps was applied from -1 V to 1 V in a 4-electrode configuration, and each step was held for 30 s to overcome transient phenomena. VGS was applied between the gate electrode and two Ag/AgCl electrodes in the source reservoir facing the nanochannel layer device in a 3-electrode configuration with a DC potential ranging from -3 V to 3 V at a 500 mV step. IDS and IGS were measured under different

VDS and VGS nested voltage sweeps applied to the working and reference electrodes.

The gate leakage investigation by using physiological solution was performed in the custom made two reservoir fixture reported in Figure 5.2. Both reservoirs were filled with either 1xPBS, 0.1xPBS or 0.01xPBS solution. The voltage was applied between the gate electrode (working electrode) and the two Ag/AgCl electrodes (counter and reference electrodes) in the reservoir facing the nanochannels using an electrochemical workstation (CH Instruments, Inc. 660E). A staircase of 250 mV steps was applied from  $-3$  V and  $+3$  V. Each step was held for 30 s to allow for stable measurement and avoid confounding effects of transient phenomena.

### 5.2.7 SEM, AFM, and Ellipsometry

To assess the nanofluidic membrane structure, we morphologically inspected nanochannels by obtaining cross-sections of the nanofluidic membrane via a gallium ion milling focused ion beam (FIB, FEI Dual-Beam 235 FIB, FEI, Hillsboro, OR, USA). The size of the nanochannels was measured with SEM (Nova NanoSEM 230, FEI, Hillsboro, OR, USA).

To investigate the thickness of the deposited layer, we performed ellipsometry measurements using a J. A. Woollam M2000U ellipsometer (Lincoln, NE, USA) on a-SiC and SiO<sub>2</sub> blanks. To assess the roughness of the surface, we performed topographic mapping by AFM (Bruker MultiMode Atomic Force Microscope).

### 5.2.8 EIS

EIS measurements were performed using blank samples with two different dielectrics, a-SiC and SiO<sub>2</sub>. The blank was inserted in the previous fixture, for which only the reservoir with two Ag/AgCl electrodes was used. The pressing of the blank samples against the cell via the O-ring left 7.07 mm<sup>2</sup> exposed to the solutions.

The measurements were performed in a 3-electrode configuration in 10<sup>-4</sup> M KCl. Impedance spectra were obtained using a 50 mV VPP amplitude AC signal over a

frequency range from  $10^{-2}$  Hz to  $10^5$  Hz and a DC potential scan ranging from -3 V to 3 V, with a step of 500 mV. Mott-Schottky analysis was carried out at a  $10^5$  Hz frequency to calculate the carrier concentrations, flat band potential, and density of interface states.

## 5.3 Results and Discussion

### 5.3.1. Nanofluidic membrane

The final nanofluidic membrane was inspected via optical microscopy to assess the mechanical integrity and the average size of the nanochannels measured via nitrogen flow test[23] was estimated  $\sim 106$  nm. The etching procedure and layer deposition uniformity were analyzed using FIB-SEM microscopy. Figure 5.5A displays the 6 mm x 6 mm x 0.4 mm nanofluidic membrane, highlighting the electrode pads at the top left and bottom right edges. The membrane features 199 vertically oriented microchannels arranged in a hexagonal fashion to optimize the membrane porosity, simultaneously preserving the structural stability. Figure 5.5B presents an SEM image of the nanochannels densely packed in 19 rows and 96 columns for each microchannel. The nanochannel cross-section is shown in Figure 5.5C, and a detailed nanochannel cross-section with different layers is presented in Figure 5.5D.

The image shows that the layers were deposited, achieving good thickness uniformity despite the high aspect ratio of the nanochannels. In comparison with our previously developed nanofluidic technologies[19,22,44,48], the nanofluidic membrane requires a simplified photolithographic process owing to the easy connection derived from the vertical orientation of both microchannels and nanochannels [22,50] and features a substantially higher nanochannel number [46,48].

Compared to other nanofluidic devices for gate control, such as AAO [123] membranes fabricated with the gate electrode only at one end of the nanochannels, our nanochannel membrane features an extended buried polysilicon gate electrode. The buried electrode represents a crucial aspect that allows fine electrostatic control by modulating the ionic conductance along the entire length of the nanochannels.

Additionally, the streamlined structure that connects nanochannels and microchannels permits the development of a nanofluidic membrane that features 278600 nanochannels, permitting a sustainable release rate in view of future biomedical applications for therapeutic administration [143].

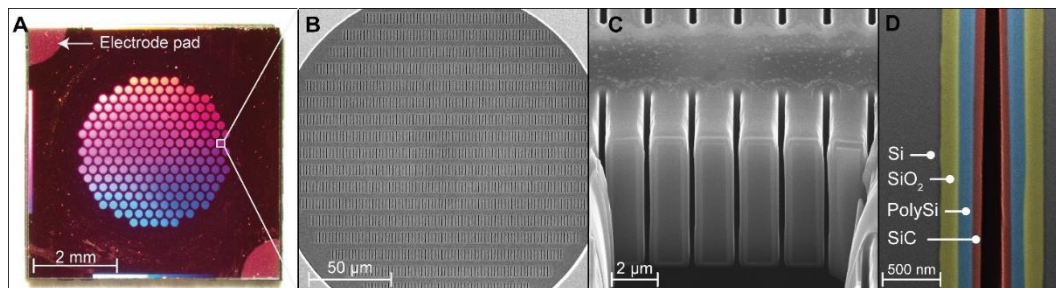


**Figure 5. 5:** Image of the silicon nanofluidic membrane. A) Final diced membrane with a size of 6 mm x 6 mm x 0.4 mm. In the photograph, the exposed contact pads of the polysilicon electrode used for connection to the external source for the polarization potential are indicated. B) SEM image of the highly densely packed parallel nanochannel design. C) FIB-SEM vertical cross-section showing the membrane nanochannels. D) FIB-SEM vertical cross-section image of the wall of a nanochannel. The layers obtained at different stages of the photolithographic processes were color-enhanced to highlight the native original p-Si of the device layer of the wafer (in gray), thermally grown silicon dioxide ( $\text{SiO}_2$ , ~175 nm, in green), poly-Si deposited by LPCVD (~121 nm, in blue), and a-SiC deposited by PECVD (64 nm, in red).

### 5.3.2 EDL modulation: theoretical background and operation mode

At the nanoscale, many transport processes in liquid are dictated by the interaction of ions with charged surfaces. Material surfaces display an electrical charge when in contact with an aqueous medium where charged species are dissolved. To neutralize the electrical charges present on the surface, counterions electrostatically accumulate at the material/solution interface. Their distribution forms a layer called the EDL. Considering the Gouy-Chapman-Stern (GCS) model, the EDL is formed by two layers of ions. The first layer, called the compact layer, is composed of solvent molecules and ions that are immobile and adsorbed on the material-solution interface. The second layer positioned over the first layer is called

the diffuse layer and consists of a mobile layer carrying a net charge within the solution. The thickness of the EDL is related to the ionic strength of the aqueous solution and the charge exhibited by the surface. In a nanochannel where the EDL thickness can be comparable to at least one of its sizes, the exclusion enrichment effect [54,55,60] and concentration polarization [144] can be observed. These phenomena can actively alter the diffusional flow of charged species and modify the ionic conductance in the nanochannel. Thus, modification of the surface charges leads to a variation in the EDL thickness and, consequently, ionic conductance. Control of the surface charge of a nanochannel can be achieved through application of an electrostatic field to the nanochannel wall, as shown in Figure 5.6. This phenomenon can be called electrostatic gate modulation [145]. Owing to this phenomenon, the surface charges of the nanochannels can be customized, allowing fine-tunable control of the ionic transport over the EDL thickness. Figure 5.6B shows the altered EDL thickness as a consequence of the electrostatic control applied to the nanochannel.

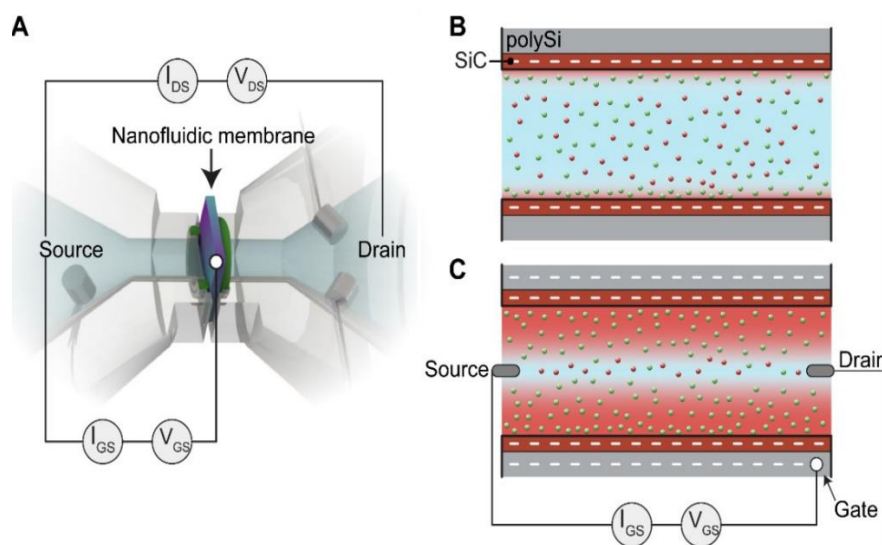


**Figure 5. 6:** Measurements set for I-V characteristics. A) To perform the I-V and conductance measurements, transmembrane potential  $V_{DS}$  is applied between the source electrode and drain electrode in the reservoir, and gate potential  $V_{GS}$  is applied between the source electrode in the reservoir and the buried gate electrode of the membrane. B) Telescopic illustration of the nanochannel wall and the buried gate electrode. C) Application of gate potential  $V_{GS}$  that polarizes the surface of the nanochannel wall, leading to alteration of the conductance of the charged species and, consequently, modulation of the ionic current  $I_{DS}$ .

To investigate the features of the nanofluidic membrane, the surface charge of the nanochannels measured by measuring the conductivity, while the gate control performance and permselectivity variation were assessed through I-V measurements.

### 5.3.3 Ionic conductance at the floating gate

To electrically characterize the nanochannels, we first performed nanochannel conductance measurements by applying transmembrane potential  $V_{DS}$  ranging from -1 V to 1 V with the gate electrode floating. Figure 5.7 shows the nanochannel conductance as a function of KCl concentration. The conductance characteristic presents two parts: the bulk conductance occurring when the nanochannel height ( $h$ ) is larger than the Debye length ( $\lambda$ ), with the ratio  $h/\lambda \gg 1$ ; the surface-dominated conductance region occurring when  $h$  is smaller than  $\lambda$ , with  $h/\lambda \sim 1$  or  $h/\lambda < 1$ . In the bulk conductance region, the conductivity is linearly dependent on the electrolyte concentration. In contrast, in the surface-dominated conductance region, the conductivity shows a plateau due to the enrichment of the counterions to compensate and neutralize the surface charge. For this reason, the conductance only depends on the surface charge.

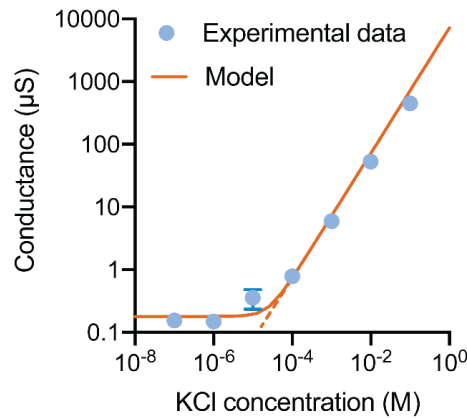


**Figure 5. 7:** Floating gate ionic conductance. Measured (points) and calculated (curve) ionic conductance across the nanochannels versus the electrolyte concentration. The dashed line represents the bulk prediction, which deviates from the experimental data in the low ionic concentration region. The standard deviation of the measurements was calculated based on three membranes, tested three times each.



The transition between the two regions occurs at  $10^{-5}$  M, where the Debye length is  $\sim 96$  nm. Considering the conductance of the nanochannels as the superimposition of the two contributions, the bulk conductance and the surface charge conductance, we can apply the following formula [146]:

$$G = 10^3(\mu_{K^+} + \mu_{Cl^-})cN_Ae \frac{wh}{l} + 2\mu_{K^+}\sigma \frac{w}{d} \quad (5.5)$$

where  $\mu_{K^+}$  and  $\mu_{Cl^-}$  are the ionic mobilities of K and Cl,  $c$  is the molar concentration,  $N_A$  is Avogadro's number, and  $w$ ,  $h$ , and  $l$  are the width, height, and length of the nanochannel, respectively. Using the width and length obtained from the morphological characterizations, we evaluated the height of the nanochannels. By utilizing the bulk conductance formula, we obtained an average nanochannel height of  $\sim 106$  nm. The results are consistent with the obtained gas flow test measurements [23]. Using the surface-dominated conductance formula reported in the equation 5.5, the surface charge on the nanochannel walls was calculated to be  $0.471 \mu\text{Cm}^{-2}$ . This result is consistent with other surface charge values for SiC [147] and our previous studies [143,148].

The native surface charge exhibited by the a-SiC is smaller than that exhibited by the widely used SiO<sub>2</sub> at pH 7.4 ( $1\text{--}100 \text{ mCm}^{-2}$ ) [149]. This aspect provides benefits when gate control is needed. The reason lies in the need to electrostatically control the reaction at the interface that acts as a charge buffer. The ability to regulate the protonation and deprotonation of reactive groups present at the dielectric/electrolyte interface is key to generating and controlling the charge distribution in the double layer [150].

### 5.3.4 I-V characteristics and leakage current

The nanofluidic membrane device has two distinguishing features: 1) phosphorus-doped polysilicon with an excess of electron carriers as the gate electrode and 2) low surface charge density. The first feature allows control of the leakage currents and consequently the power dissipation of the devices. Regarding the second aspect, exhibiting a low surface charge density environment can help

with high-efficiency gate modulation. In fact, small changes in gate potentials can be relatively significant in the case of very low surface charge [70,151].

To test the performance of the nanofluidic membrane, ionic current  $I_{DS}$  vs  $V_{DS}$  curves were measured as a function of  $V_{GS}$  within the voltage range of  $|V_{GS}| < 3$  V at a step of 0.5 V and  $|V_{DS}| < 1$  V at a step of 0.25 V. To evaluate the power consumption, we simultaneously measured the leakage current  $I_{GS}$  vs.  $V_{GS}$  flowing from the gate to source. To test the ability of the nanofluidic membrane to modify the permselectivity of the nanochannels, measurements were performed in  $10^{-5}$  M KCl, the concentration at which the nanochannels present the transition between the surface-charge-governed regime and the geometry-governed regime. Here, the electrolyte exhibited a Debye length comparable to the nanochannel height of the nanofluidic membrane. Moreover, the gating performance of the nanofluidic membrane were evaluated using  $10^{-4}$  M KCl, a concentration at which  $\lambda < h$ . The purpose of this investigation is to evaluate the capability of the n-doped polysilicon electrode to manipulate the extension of the EDL in the nanochannel under the condition of the conductance being dictated by the geometry.

Figure 5.8 shows a representation of the ionic flow when gate and transmembrane potentials are applied. The transmembrane potential  $V_{DS}$  influences the direction of the ions in the nanochannels. The application of  $V_{DS} < 0$  V directs potassium ions  $K^+$  to the drain electrode and negative chloride ions  $Cl^-$  to the source electrode, whereas  $V_{DS} > 0$  V conveys  $K^+$  to the source and  $Cl^-$  to the drain. Some of the ions in the nanochannels are partially involved in the formation of the EDL depending on the polarization potential applied to the gate electrode and consequently the exposed surface charge. The negative charge of the nanochannel wall and the n-doping profile of the polysilicon strongly influence the ionic transport in the nanochannel since it exhibits an excess of negative carriers (i.e., electrons in the polysilicon) that attract a majority of positive ions to the nanochannel wall. As a consequence, the ionic transport in the nanochannels and thus the conductance and leakage currents are strongly influenced.

Upon application of polarization potential  $V_{GS}$ , the charged ionic species are electrostatically attracted to the nanochannel wall and participate in forming the EDL.  $V_{GS} < 0$  V attracts positive  $K^+$  to the nanochannel wall, creating a positively charged EDL. As a consequence, the number of positive ions  $K^+$  in the nanochannel

increases (Figure 5.8A and B), and negative ions  $\text{Cl}^-$  are repelled. In contrast,  $V_{\text{GS}} > 0$  V attracts  $\text{Cl}^-$  ions to the nanochannel wall, creating a negative EDL and repelling  $\text{K}^+$  (Figure 5.8C and D).

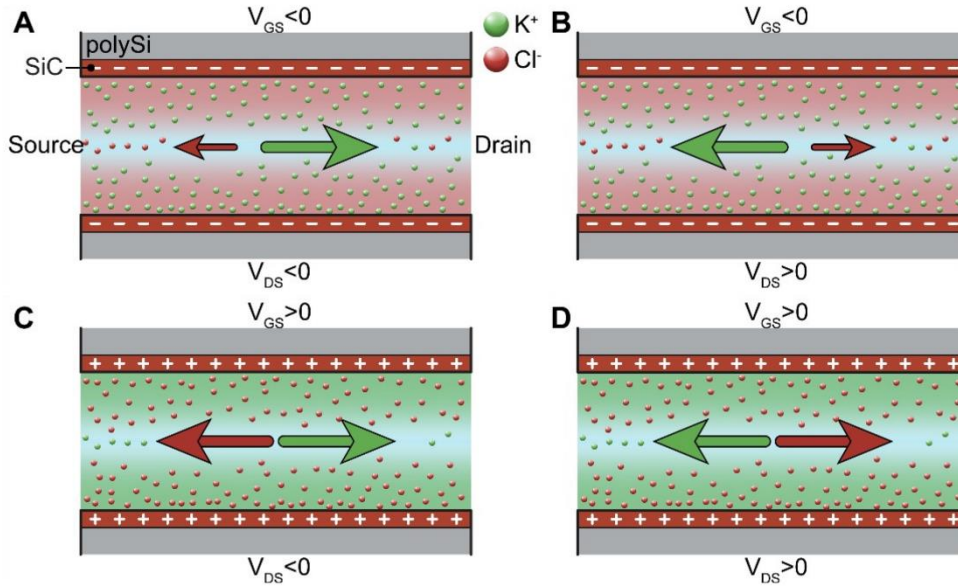


**Figure 5. 8:** Ionic current  $I_{\text{DS}}$  when gate potential  $V_{\text{GS}}$  and transmembrane potential  $V_{\text{DS}}$  are applied. Blue points represent  $\text{Cl}^-$  ions, while red points represent  $\text{K}^+$  ions.  $V_{\text{DS}} < 0$  V attracts positive potassium ions  $\text{K}^+$  to the drain electrode, whereas  $V_{\text{DS}} > 0$  V attracts negative chloride ions  $\text{Cl}^-$  to the source electrode.  $V_{\text{GS}} > 0$  V draws  $\text{Cl}^-$  to the nanochannel wall, creating a negatively charged EDL. Consequently, the number of negative ions in the nanochannel increases, and positive ions  $\text{K}^+$  are repelled.  $V_{\text{GS}} < 0$  V attracts  $\text{K}^+$  to the nanochannel walls, leading to an increased number of  $\text{K}^+$  and a decreased number of  $\text{Cl}^-$ .

The experimentally measured  $I_{\text{DS}}-V_{\text{DS}}$  characteristics and leakage current  $I_{\text{GS}}-V_{\text{GS}}$  in  $10^{-5}$  M KCl and  $10^{-4}$  M KCl are presented in Figure 5.9. The nanochannel membrane shows a unipolar behavior with a shallow surface charge density due to the a-SiC layer and the gate electrode, the so-called all-around-gate structure. Figure 5.9A and C show  $I_{\text{DS}}$  for  $10^{-5}$  M KCl and  $10^{-4}$  M KCl, respectively. At higher KCl concentrations, higher ionic current values were obtained. When  $V_{\text{GS}} = 0$  V, the ionic current shows a linear ohmic relationship between  $I_{\text{DS}}$  and  $V_{\text{DS}}$ . The same ionic current is expected for both coions and counterions, independent of the drain and source electrode, because potassium and chloride have similar mobilities in a

liquid ( $76.2 \times 10^{-7} \text{ m}^2/\text{sV}$  for  $\text{K}^+$  and  $79.1 \times 10^{-7} \text{ m}^2/\text{sV}$  for  $\text{Cl}^-$ ) [152]. Upon applying the gate voltage, the ionic conductance can vary based on the polarity of the ions in the bulk.

In solid-state electronics such as FET devices, the electronic current depends on the gate voltage and the doping of the device, and the nanofluidic membrane exhibits behavior comparable to that of a p-type junction FET (JFET), where upon application of a positive gate voltage, the electronic current decreases. Application of  $V_{\text{GS}} > 0 \text{ V}$  leads to reductions in the ionic conductance and  $I_{\text{DS}}$  over the range  $|V_{\text{DS}}| < 1 \text{ V}$ . In contrast, application of  $V_{\text{GS}} < 0 \text{ V}$  leads to two different scenarios based on the polarity of  $V_{\text{DS}}$ . For both concentrations  $10^{-5} \text{ M}$  and  $10^{-4} \text{ M KCl}$ , a negative transmembrane potential  $V_{\text{DS}} < 0 \text{ V}$  causes increases in the ionic current and conductance in the nanochannels, whereas a positive transmembrane potential  $V_{\text{DS}} > 0 \text{ V}$  generates decreases in the ionic current and conductance in the case of  $10^{-5} \text{ M KCl}$  and a slight effect on the transmembrane current  $I_{\text{DS}}$  and conductance in the case of  $10^{-4} \text{ M KCl}$ .

To explain the ionic transmembrane current behavior, one can refer to conduction mechanisms in an aqueous solution. The recombination process between the high number of electrons in the polysilicon and the ions in the aqueous solution [153,154] could be responsible for the different responses of the nanochannels. Additionally, we need to consider that a-SiC can act as an amorphous n-doped semiconductor [155]. Regarding this last aspect, the polarization potential  $V_{\text{GS}}$  can strongly influence the conduction mechanism in the dielectric a-SiC. Due to its nature, a-SiC favors recombination of electrons with positive ionic species. Realistically, in the case of  $V_{\text{GS}} < 0 \text{ V}$ , some of the positive charges electrostatically attracted to the nanochannel wall could be involved in the conduction mechanism, and consequently, the thickness of the EDL could be reduced since the species return to their electroneutral state [153,154]. Upon application of  $V_{\text{DS}} < 0 \text{ V}$ , many positive ions are attracted into the nanochannels, increasing  $I_{\text{DS}}$  and the conductivity. In contrast,  $V_{\text{DS}} > 0 \text{ V}$  drives negative charges into the nanochannels that are repelled by the application of a negative polarization potential. In the case of  $V_{\text{GS}} > 0 \text{ V}$ , the negative ions  $\text{Cl}^-$  attracted to the nanochannel wall are negligibly

involved in the conduction mechanism. Higher values of  $V_{GS}$  induce the EDL to extend in the nanochannels, leading to reduced  $I_{DS}$  and conductance. Considering the  $I_{DS}$  in  $10^{-4}$  M KCl for  $V_{DS} = 1$  V,  $V_{GS} = 3$  V causes  $I_{DS}$  to decrease from 600 nA to 129 nA, corresponding to a promising reduction of 78.5% in the ionic transmembrane flow. Additionally, it can be observed that for values of  $V_{GS}$  in the range of 1.5 V to 3 V,  $I_{DS}$  exhibits a slight reduction. This phenomenon can be associated with the electron depletion region formed at the polysilicon-dielectric interface. In fact, for a positive polarization potential, the electrostatic attraction of negative ions to the dielectric interface is achieved by the lack of electrons at the polysilicon-dielectric interface. This lack produces an electron depletion region, where positive electronic carriers (called holes) are responsible for electrostatic control of the EDL. Since the polysilicon is doped with an excess of electrons, holes are numerically inferior in the depletion region. Therefore, the positive electrostatic charge that can be modulated in the depletion region is lower than the negative charge originating from negative  $V_{GS}$ . As a consequence, the EDL cannot be exceedingly extended.

The n-doping of the polysilicon and the behavior of the a-SiC as a negative amorphous semiconductor are responsible for the asymmetric leakage currents presented in Figure 5.9B and D. In fact, these two aspects strongly influence the conduction mechanism upon voltage application, working in favor of the conduction mechanism for negative gate potential  $V_{GS}$  and against it for positive gate potential  $V_{GS}$ . Further details will be presented in the next section.

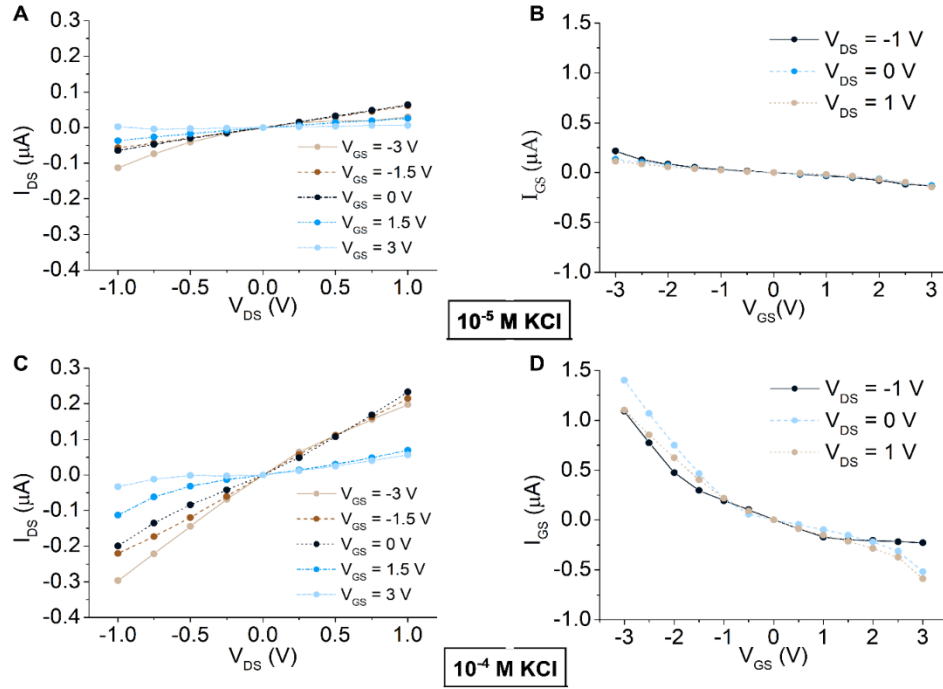


**Figure 5. 9:** I-V ( $I_{DS}$  vs  $V_{DS}$ ) ionic transfer characteristics and leakage current ( $I_{GS}$  vs  $V_{GS}$ ) characteristics of the nanofluidic membrane measured for  $10^{-5}$  M KCl and  $10^{-4}$  M KCl. A)  $I_{DS}$  vs  $V_{DS}$  measured for  $10^{-5}$  M KCl. B)  $I_{GS}$  vs  $V_{GS}$  measured for  $10^{-5}$  M KCl. C)  $I_{DS}$  vs  $V_{DS}$  measured for  $10^{-4}$  M KCl. D)  $I_{GS}$  vs  $V_{GS}$  measured for  $10^{-4}$  M KCl.

Figure 5.10 shows the nanochannel conductance for  $10^{-4}$  M KCl as the ratio of the conductance modulated by the application of  $V_{GS}$  and the conductance at the floating gate at  $V_{DS} = -1$  V and  $V_{DS} = 1$  V. The graph indicates that for  $V_{DS} = -1$  V, the conductance is enhanced for  $V_{GS} < 0$  V and reduced for  $V_{GS} > 0$  V. In the case of  $V_{DS} = 1$  V,  $V_{GS} < 0$  V does not significantly influence the conductance in the nanochannels, while  $V_{GS} > 0$  V causes a significant reduction in the normalized conductance. Additionally, the conductance exhibited at  $V_{GS} = 3$  V is barely reduced compared to the conductance calculated at  $V_{GS} = 1.5$  V. This finding is in agreement with previously described ionic transport phenomena occurring in the nanochannels.

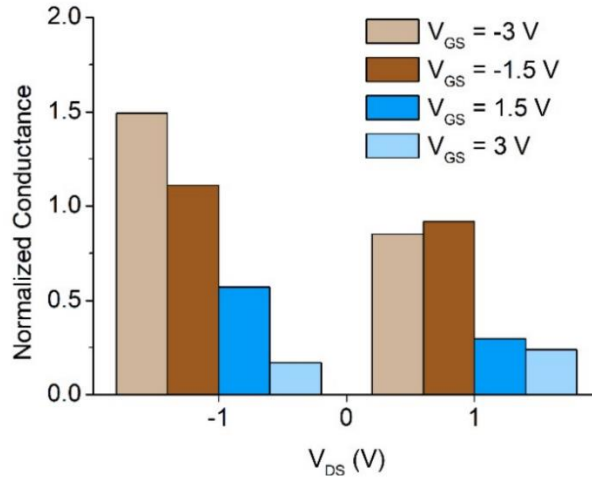


**Figure 5. 10:** Normalized conductance for  $10^{-4}$  M KCl, defined as the ratio of the conductance after application of the gate voltage to the conductance measured with a floating gate for  $V_{DS} = -1$  V and  $V_{DS} = 1$  V.

### 5.3.5 Power consumption in KCl

Leakage currents allow estimation of the power consumption ( $P_{diss}$ ) of the nanofluidic membrane. The worst working conditions are created when  $I_{GS}$  exhibits higher values in the range of applied gate potential of -3 V to 3 V. Referring to  $10^{-4}$  M KCl, higher values of  $I_{GS}$  are shown for  $V_{GS} = \pm 3$  V and  $I_{DS} = 0$  V. In these cases, the power consumption ( $P_{diss}$ ) results in  $P_{diss} = 4.2 \mu\text{W}$  for  $V_{GS} = -3$  V and  $P_{diss} = 1.74 \mu\text{W}$  for  $V_{GS} = 3$  V. By applying  $V_{DS}$ ,  $P_{diss}$  for  $V_{GS} = 3$  V can be reduced by approximately 22%, and in the case of  $V_{GS} = -3$  V, the power consumption can be reduced by 87%. Compared with previous work, the power consumption was reduced by one order of magnitude [143]. This can be related to the fact that the ionic strength of the solution used for this measurement is 1.37 times lower than the ionic strength of the solution used for our previous study [143].

An advantageous aspect of having asymmetric leakage currents lies in reducing the power consumption. In fact, we meet the need to reduce the ionic conductance by modulating the EDL extension in the nanochannel with the application of  $V_{GS} > 0$  V. Under this condition, the considerable performance of the nanofluidic membrane is associated with low power consumption.

The investigation of the capability of the nanofluidic membrane to electrostatically modulate the conductance and ionic transport in the nanochannel geometry-dictated regime can lay the groundwork to use biocompatible nanofluidic membranes in reservoir-based implants. In such devices, the highly concentrated drug in the reservoir is released at a rate established by the geometrical dimensions of the nanochannels [22,26,30,37]. In view of future manipulation of charged drug molecules, evaluation of the electrostatic control of ionic species exhibiting a Debye length  $\lambda$  almost one-third of the nanochannel height can provide a demonstration of the performance of the nanofluidic membrane.

### 5.3.6 Leakage current in PBS

Furthermore, the performance of a-SiC were investigated in PBS solution. The leakage currents was measured and compared with the gate leakage current in an equivalent chip with a SiO<sub>2</sub> insulator layer instead of a-SiC, since SiO<sub>2</sub> and in general metal oxides represent the standard for gate dielectrics in solid electronics[156]. However, lack of durability and reliability of SiO<sub>2</sub> in aqueous environment leads to the adoption of alternative materials such as a-SiC. As the leakage current is affected by the ionic strength of the solution[157], the leakage currents was analyzed for both SiO<sub>2</sub> reported in Figure 5.11A and a-SiC reported in Figure 5.11B at three different ionic strengths[143].

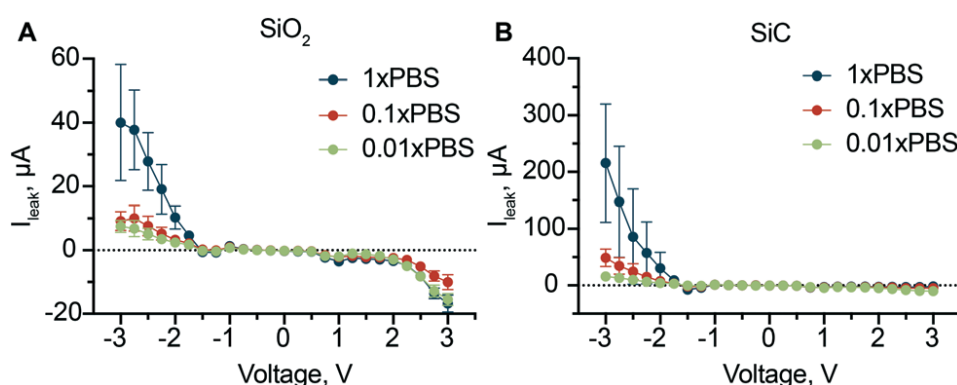


**Figure 5. 11:** Gate leakage current. Gate leakage current at different solution concentrations for A) SiO<sub>2</sub> dielectric layer A) and B) a-SiC dielectric layer.



The results clearly show a linear dependence of the leakage current on the ionic strength of solution for both dielectric materials, hinting that the origin of this phenomena lies on the ionic charges in solution. As opposed to solid electronics where SiO<sub>2</sub> and a-SiC have high intrinsic breakdown voltages,  $\sim 15 \text{ MV cm}^{-1}$  [158] and  $\sim 2 \text{ MV cm}^{-1}$  [83] respectively, the leakage currents measured exhibited values in the order of  $\mu\text{A}$  for  $0.5 \text{ MV cm}^{-1}$ . These findings are related to the ‘non-ideality’ of the insulating materials as the presence of defects and irregularities both in the oxide layer or at the Si–SiO<sub>2</sub> interface can increase the current flow at low electric fields [158]. Although this phenomena has been investigated for more than 50 years, several aspects of the time-dependent dielectric breakdown are not yet fully understood, especially in the presence of aqueous solutions [158]. The most accepted theory (percolation model) postulates that with the application of an external electric field, electrons are injected and trapped into the oxide. There they can create clusters that, when within tunneling distance, create percolating paths (known also as conductive filaments) [159]. These lead to increased currents through the insulating films [160]. In aqueous solutions, formation of defects can be accelerated by the migration of protons in the insulating material [161] where the dissolution of a percolating path can create nanometric pores [162]. Therefore, high ionic strength of solution results in a high probability of the defect formation and thus high leakage currents. Interestingly, the current for negative applied voltages is significantly higher than the respective positive voltages especially for a-SiC.

As previously illustrated, this asymmetry can be due to the doping of the polysilicon. Moreover, depending on the gate voltage, the mechanism of formation of conductive filaments inside the dielectric material can be more or less noticeable. Also, in case of PBS, the negative voltage, and consequently, the electric field pulls protons from the solution to the solid interface. Protons travel through the insulator and can interact with electrons when they reach the dielectric/poly-Si interface. This mechanism promotes the formation of a conductive filament in the insulating material, resulting in high currents. Conversely, a positive voltage, pushes the protons toward the solution, resulting in the breaking of eventual conductive filaments already present significantly lowering leakage currents. Both dielectrics

seem to be affected by these phenomena. However, in aqueous environment a-SiC has the advantage of being more stable[143].

### **5.3.7 Power Consumption and Electrostatic gating energy efficiency in PBS**

Power consumption was measured and the value ranged from 1.5  $\mu\text{W}$  to 45  $\mu\text{W}$ , and it was depended on the applied voltage. Accordingly, commercially available and implant compatible 200 mA h batteries could support implant autonomy from 6 months to a few years, depending on the schedule of applied voltages. Compared to previous works[19,50], the power consumption was reduce power consumption by almost one order of magnitude. This was achieved by adopting electrostatic gating as opposed to electrophoresis or ionic concentration polarization, which were associated with substantially higher currents. In electrostatic gating, the energy consumption is determined by leakage currents through the dielectric film. Despite the fact that materials exhibiting high-k dielectrics constant can achieve very low leakage currents, they lack in biocompatibility and bio inertness. The use of the bio inert a-SiC demonstrated to achieved power consumption comparable to previously developed gating devices[48,123].

### **5.3.8 Leakage current and Cyclic voltammetry**

Further investigation regarding the leakage currents in PBS were performed by using cyclic voltammetry, and it was compared to a  $\text{SiO}_2$  coated device[148]. The measurements did not show substantial differences between  $\text{SiO}_2$  and a-SiC, except for 3V, as reported in Figure 5.12. However, the steep increase in leakage observed for a-SiC between 2 and 3 V, emphasized by the electrolytic solution environment, highlight that the amorphous silicon carbide can act as a semiconductor, while the silicon dioxide is exhibiting an insulating behavior associated with the lower current[158].

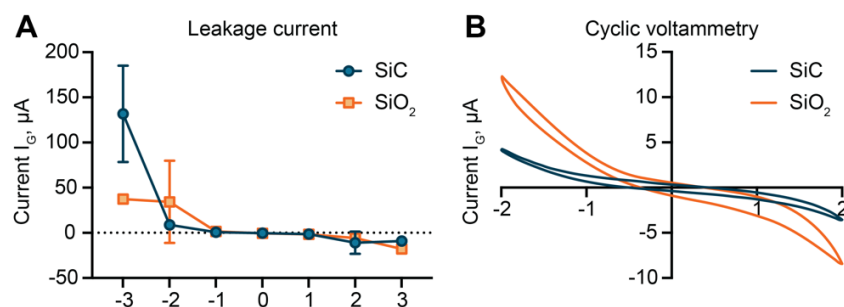


**Figure 5. 12:** Leakage current and cyclic voltammetry in PBS. A) Comparison of gate leakage current for SiO<sub>2</sub> and a-SiC dielectric. B) Cyclic voltammetry comparison between SiO<sub>2</sub> and SiC.

In the voltage range between  $-2$  and  $2$  V, SiC and SiO<sub>2</sub> exhibited similar values of leakage currents. Thus, cyclic voltammetry (CV) was performed to closer investigate differences. As compared to SiO<sub>2</sub>-coated membranes, lower currents were measured for SiC at each applied voltage (Figure 5.12B). Interestingly, the non-linear proportional relationship between voltage and current for both materials was observed. a-SiC exhibited a steep increase in current for voltages higher than  $1$  V in absolute value. This suggested that for small applied voltages, no faradaic currents occurred, and the material behaved almost as an ideal capacitor. For voltages above  $\pm 1$  V, electrochemical reactions between the surface groups (SiO<sup>-</sup>) and reactive species in the electrolyte solution (Cl<sup>-</sup>, HO<sup>-</sup>) led to increased currents. In contrast, the significant current increase observed for the leakage currents (Figure 5.12A) for voltages over  $2$  V was likely related to material deterioration and conductive filament formation. The asymmetry between results obtained with positive and negative voltages provided further support for this theory. Higher currents for negative applied voltages were observed in both measurements. For negative voltages, positive species were attracted to the surface. The percolation model suggests that in the presence of strong electrostatic attraction, protons can diffuse in the insulator, starting a percolating path that can lead to the formation of a conductive filament[159]. Instead, for positive potentials, proton repulsion may cause a reversible interruption of the conductive filament, effectively decreasing leakage[163]. Additionally, the difference in hysteresis between the two CV profiles (Figure 5.12B) was suggesting a difference in surface charge accumulation between the two materials. A thinner CV profile usually correlates with low charge

accumulation. Collectively, the results showed that a-SiC suffered lower leakage currents in the  $-2$  V to  $2$  V range, exhibiting a lower charge accumulation. This can be associated with semiconductive behavior of the a-SiC, that allow the charges to be removed from the a-SiC bulk material, avoiding the storage into it.

### 5.3.9 EIS Investigation on polysilicon electrode using a blank device

To further investigate the physics of the nanofluidic membrane by deeping the phenomena that can originate the I-V gating performances, the gate electrode interface was immersed in  $10^{-4}$  M KCl aqueous solution. To do so, the dielectric-polysilicon heterojunction was reproduced on a blank device, and EIS measurements were performed. The same investigation was conducted on blanks with  $\text{SiO}_2$ , comparing the dielectric performances. Measurements were performed in a frequency range from  $10^{-2}$  Hz to  $10^5$  Hz by applying D.C. polarization potentials to the gate electrode from  $-3$  V to  $3$  V at a step of  $0.5$  V. These bias conditions hold the structure at an operating bias point such that the behavior of the structure is fairly linear over a small range of voltages around the bias point. First, the transport properties associated with the heterojunction immersed in KCl were determined and associated a small-signal LTI electric circuit and the transfer function. The transfer function represents an essential aspect of designing electronic control customized based on physical phenomena between solids and electrolytes. Then, the flat band potential  $V_{fb}$  was calculated by using the Mott-Schottky plot. Compared with the  $\text{SiO}_2$ , the a-SiC exhibits a lower  $V_{fb}$ , which is favorable for easily manipulating the surface charge. Then, the density of states  $D_{it}$  was calculated. These are “defects” that can be responsible for a higher leakage current and can be associated with the chemical process used to fabricate the dielectric/polysilicon interface.

### 5.3.10 Ellipsometry and AFM

The thickness of the deposited layers of the blank samples was assessed via ellipsometric measurements. Measurements related to a-SiC are presented in Figure 5.13A. The polysilicon layer in both cases was measured to be  $\sim 121 \text{ nm} \pm 15 \text{ nm}$ , the a-SiC layer was measure to be  $\sim 64 \text{ nm} \pm 10 \text{ nm}$ , and the  $\text{SiO}_2$  was measured to be  $\sim 66 \text{ nm} \pm 13 \text{ nm}$ . Morphological evaluation of the surface of the dielectric

coating was performed via AFM investigation. Measurements were performed at three different spots and averaged. Figure 5.13B shows a 50  $\mu\text{m}$  x 50  $\mu\text{m}$  AFM topographic map for an a-SiC blank device. The surface roughness was 22.9 nm  $\pm$  4.7 nm for a-SiC and 14.5 nm  $\pm$  3.9 nm for SiO<sub>2</sub>. The higher surface roughness measured for a-SiC blank devices can be associated with the pump-down vacuum phase verifiable during the fabrication process. During PECVD, the debris lying on the surface of the chamber could be redistributed on the sample surface by turbulent flows generated during the process.

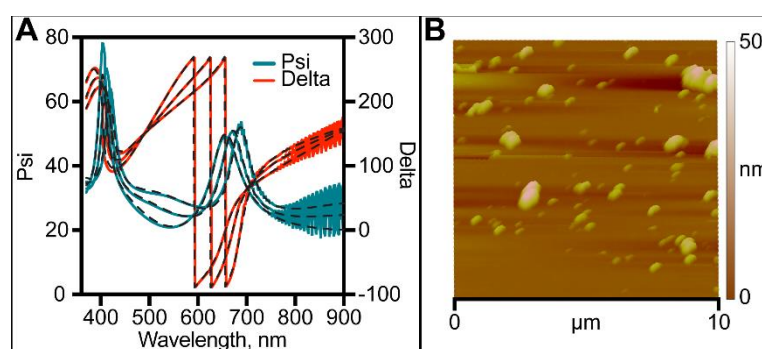


**Figure 5. 13:** Ellipsometric and AFM measurements. A) Ellipsometric measurement on blank a-SiC blank sample. B) 3D topographical map of 10  $\mu\text{m}$  x 10  $\mu\text{m}$  a-SiC blank sample.

**Band diagram theory.** When immersed in an aqueous solution, the blanks and the solution form a system that is organized into three layers and two interfaces: the first layer corresponds to the semiconductor n-polysilicon, which represents the buried electrode, the second layer corresponds to the dielectric coating, a-SiC or SiO<sub>2</sub>, and the third layer corresponds to the aqueous solution, as shown in Figure 5.14A. This is very similar to the solid-state MOS capacitor device composed of a metal layer, a dielectric layer, and a polysilicon layer. Here, the metal layer is replaced by the conductive electrolyte solution KCl, and the gate voltage is applied to the polysilicon. To explain how the polarization potential influences the carriers in the polysilicon, one can refer to band theory. Application of a polarization potential puts the blank into one of three states: accumulation, flat band condition, and inversion, as illustrated in the band diagram presented in Figure 5.14B. When no polarization potential is applied with  $V_{\text{GS}} = 0$  V, the Fermi level  $E_F$  in the polysilicon is pinned close to the conduction band  $E_C$  due to the nature of the

phosphorus donors. Notably, there is no Fermi level in the solution in contact with the dielectric since there is no redox couple in it. Applying a negative polarization potential  $V_{GS} < 0$  V to the electrode causes electron accumulation at the dielectric-semiconductor interface. The band bending presents a downward curvature and a thin layer, typically a few angstroms, of high electron concentration. This phenomenon leads to positive ions accumulating at the dielectric-electrolyte interface. Applying a positive polarization bias ( $V_{GS} > 0$ ) to the gate electrode causes a region depleted of electrons called the depletion zone to be formed. Here, the majority of carriers are holes, which are the native charges of the semiconductor, and the band bending presents an upward curvature. Mainly, in both cases, band bending occurs in the semiconductor, and a small part of it occurs at the double layer. Although the chemical potential in the dielectric and electrolyte cannot be well defined, the electrostatic potential drop can be determined [164]. For a capacitor,  $V = q/C$ , the potential drop across the EDL is smaller than the potential drop across the dielectric ( $C_{EDL} > C_{SD}$ ). According to the theory of solid-state semiconductor devices such as MOS capacitors [55], in the accumulation region, the capacitance increases due to the high number of electrons. Meanwhile, in the depletion region, the lack of electrons causes the capacitance to decrease until its value becomes almost constant.

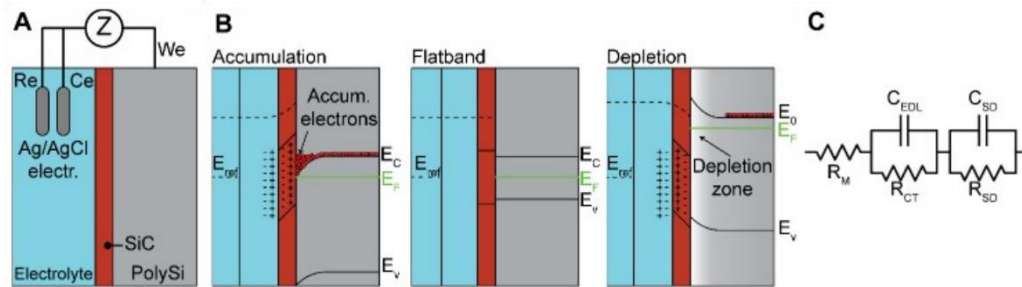


**Figure 5. 14:** Blank setup measurements. A) Blank sample immersed in the KCl electrolyte. B) Band diagram of a layered structure composed of the semiconductor poly-Si, a dielectric, and an electrolyte. Accumulation for  $V_{GS} < 0$ , flat band for  $V_{GS} = 0$  V, and depletion for  $V_{GS} > 0$  V. C) Equivalent circuit used to fit the impedance data.  $R_M$  is the electrolyte resistance,  $R_{SD}$  and  $C_{SD}$  are the resistance and the capacitance associated with the dielectric coating,  $R_{CT}$  is the charge transfer resistance, and  $C_{EDL}$  is the Helmholtz capacitance due to the EDL.

**Schematic circuit.** An equivalent LTI model for the buried electrodes was proposed and is shown in Figure 5.14C. The equivalent circuit includes a combination of resistances (R) and capacitors (C). For interpretation of the results, the fact that the resistance is a parameter strongly related to the carrier transport properties must be considered, and at the same time, the capacitance is linked to the carriers. The circuit is composed of the following elements:  $R_M$  represents the resistance of the electrochemical solution  $10^{-4}$  M KCl. The first parallel part is associated with the electrolyte-dielectric interface, and it is composed of  $C_{EDL}$ , the capacitance associated with the EDL, and  $R_{CT}$ , the charge transfer resistance associated with the charge transfer through the dielectric coating. The second parallel part is associated with the dielectric-semiconductor interface, and it is composed of  $C_{SD}$ , the capacitance associated with the semiconductor interface state capacitance, and  $R_{SD}$ , the resistance associated with the semiconductor interface state resistance.

The nonideality of the interfaces was considered, taking into account the nonconstant thickness of the deposited layers (polysilicon layer  $\sim 121 \text{ nm} \pm 15 \text{ nm}$ , a-SiC layer  $\sim 64 \text{ nm} \pm 10 \text{ nm}$ , and  $\text{SiO}_2$  layer  $\sim 66 \text{ nm} \pm 13 \text{ nm}$ ) and the experimental roughness (a-SiC layer  $\sim 22.9 \text{ nm} \pm 4.7 \text{ nm}$  and  $\text{SiO}_2$  layer  $\sim 14.5 \text{ nm} \pm 3.9 \text{ nm}$ ) measured as reported in Section 5.3.10 due to the deposition process and chemical defects that can be present in both the semiconductor polysilicon and dielectric layers [67–70]. For this reason, it is possible to use a constant phase element to relate to the  $i$ -th capacitance via the relationship  $Z_{CPEi} = \frac{1}{Q_i(j\omega)^{n_i}}$ , where  $Q_i$  is the constant associated with the constant phase element, and  $n_i$  is the empirical exponent measuring the distortion from the ideal impedance components. The constant phase element can be considered a capacitance when the value of  $n_i$  satisfies  $0.5 < n < 1$ . Figure 5.15 shows the  $R_{CT}$ ,  $R_{SD}$ ,  $Q_{EDL}$ , and  $Q_{SD}$  for both 64 nm a-SiC and 64 nm  $\text{SiO}_2$ . The resistance associated with the electrolyte solution  $R_M$  was estimated from the Nyquist plot and was found to be  $\sim 100 \text{ } \Omega$  in all measurements. Values were obtained by fitting the measured data with the circuit model shown in Figure 5.14C. Compared to the case without application of a polarization potential, both dielectrics SiC and  $\text{SiO}_2$  exhibit the same trend. Negative values of polarization potential  $V_{GS} < 0 \text{ V}$  cause  $R_{CT}$  and  $R_{SD}$  to decrease, while  $Q_{EDL}$  and  $Q_{SD}$  increase. For positive polarization potential  $V_{GS} > 0 \text{ V}$ , the opposite trend for  $R_{CT}$ ,  $R_{SD}$ ,  $Q_{EDL}$ , and  $Q_{SD}$  can be observed. We associated this behavior with the accumulation or

depletion of electrons at the dielectric-polysilicon interface, as previously illustrated. According to band diagram theory, as previously reported, in the accumulation state occurring for  $V_{GS} < 0$  V, the high number of electrons at the polysilicon-dielectric interface leads to a higher availability of electrons that can participate in the transfer process from the polysilicon to the aqueous solution through the dielectric, leading to a decrease in resistances associated with the interfaces (Figure 5.15A and B). At the same time, this phenomenon increases the capacitance at the polysilicon-dielectric interface and consequently increases the capacitance of the EDL at the dielectric-electrolyte interface (Figure 5.15C and D). Analogously, in the depletion state, electron carriers are depleted. This phenomenon leads to increases in the interface resistances and decreases in the capacitances associated with both interfaces, polysilicon-dielectric and dielectric-electrolyte, with respect to the case of no polarization potential applied.

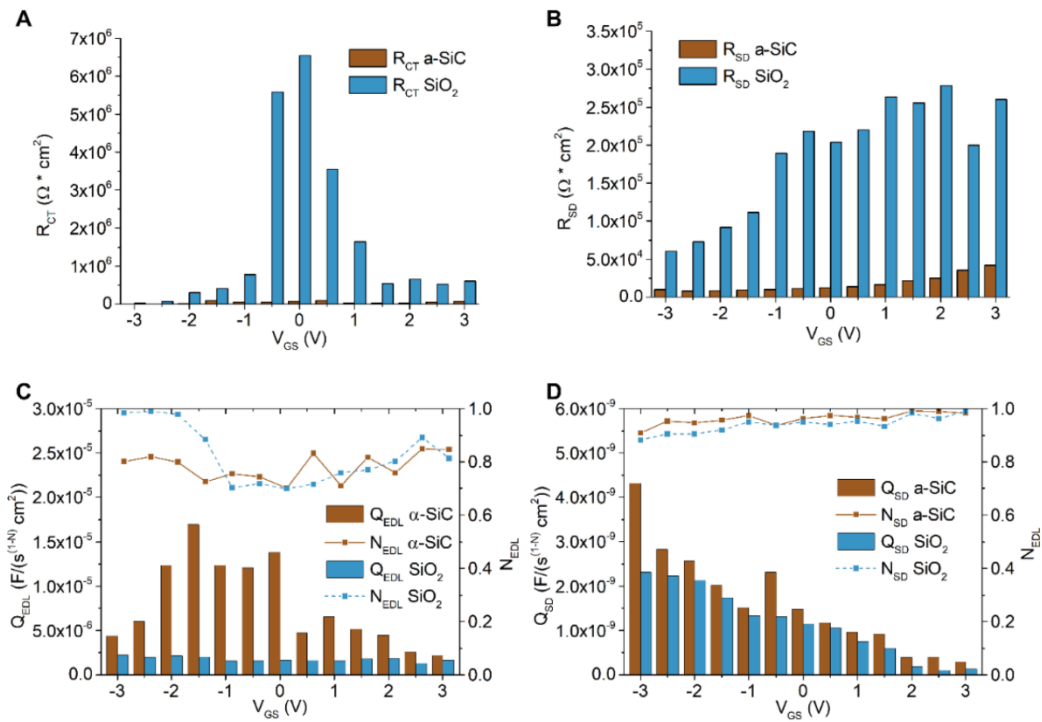


**Figure 5. 15:** Comparison between the fitted values for a-SiC and SiO<sub>2</sub>. A)  $R_{CT}$  charge transfer resistance; B)  $R_{SD}$  resistance of the polysilicon; C)  $Q_{EDL}$  constant phase element and its  $n_{EDL}$  factor associated with the EDL; D)  $Q_{SD}$  constant phase element and its  $n_{SD}$  factor associated with the polysilicon.



Compared with SiO<sub>2</sub> at V<sub>GS</sub> = 0 V, the a-SiC dielectric shows an R<sub>CT</sub> hundreds of times smaller. By applying a polarization potential, considering the entire range of -3 V to 3 V, the R<sub>CT</sub> for SiC maintains the trend, and it remains between tens and hundreds of times smaller than the R<sub>CT</sub> for SiO<sub>2</sub>. Analogously, the a-SiC R<sub>DS</sub> is tens of times smaller than that of SiO<sub>2</sub>. Regarding the constant phase elements associated with the two electrolyte/dielectric and dielectric/semiconductor interfaces, n<sub>EDL</sub> and n<sub>SD</sub> are in the range of 0.7 to 1. This fact confirms that the constant phase element acts as a capacitance. The Q<sub>EDL</sub> values exhibited by a-SiC are 1.5 to 8 times larger than those for SiO<sub>2</sub>. Very similar, the Q<sub>SD</sub> values of a-SiC are 0.8 to 3.1 times larger than those of SiO<sub>2</sub>. These differences were associated with the fact that SiO<sub>2</sub> is an insulator, while a-SiC can be considered an amorphous semiconductor material. In amorphous materials, there are free immobilized electrons in the disordered network [165]. Their presence provides stored charges that increase the capacitance associated with these materials.

The corresponding relaxation times for the two interfaces can be determined as  $\tau_{EDL} = (Q_{EDL}R_{CT})^{n_{EDL}}$  and  $\tau_{DS} = (Q_{DS}R_{DS})^{n_{DS}}$ . These quantities correspond to the amount of time needed for polysilicon and the dielectric to reach equilibrium. They are related to the charge transfer phenomena and to the recombination lifetime of the carriers. Specifically, for a-SiC,  $\tau_{EDL}$  is between 3 ms and 1.8 s, while in the case of SiO<sub>2</sub>,  $\tau_{EDL}$  is between 50 ms and 30 s, where the maximum values are measured at V<sub>GS</sub> = 0 V. These values are in agreement with the theoretical explanation of amorphous semiconductor and insulator materials [166,167]. Regarding the recombination lifetime  $\tau_{DS}$ , a-SiC exhibits values between 8.9  $\mu$ s and 12  $\mu$ s, while SiO<sub>2</sub> exhibits values between 38  $\mu$ s and 43  $\mu$ s. The measured values are in agreement with other values measured for polycrystalline silicon [168].

The total impedance exhibited by the buried electrode immersed in the ionic solution associated with the fitting electrical circuit (Figure 5.14C) can be written as

$$Z = R_M + \left( \frac{1}{R_{CT}} + \frac{1}{Z_{CPE_{EDL}}} \right)^{-1} + \left( \frac{1}{R_{DS}} + \frac{1}{Z_{CPE_{DS}}} \right)^{-1}. \quad (5.6)$$

The real and imaginary parts of the impedance can be separated and written as

$$Re[Z] = R_M + \frac{R_{CT} \left( 1 + R_{CT} Q_{EDL} \omega^{n_{EDL}} \cos \frac{n_{EDL} \pi}{2} \right)}{1 + 2 R_{CT} Q_{EDL} \omega^{n_{EDL}} \cos \frac{n_{EDL} \pi}{2} + (R_{CT} Q_{EDL} \omega^{n_{EDL}})^2} + \frac{R_{SD} \left( 1 + R_{SD} Q_{SD} \omega^{n_{SD}} \cos \frac{n_{SD} \pi}{2} \right)}{1 + 2 R_{SD} Q_{SD} \omega^{n_{SD}} \cos \frac{n_{SD} \pi}{2} + (R_{SD} Q_{SD} \omega^{n_{SD}})^2}, \quad (5.7)$$

$$Im[Z] = \frac{R_{CT}^2 Q_{EDL} \omega^{n_{EDL}} \sin \frac{n_{EDL} \pi}{2}}{1 + 2 R_{CT} Q_{EDL} \omega^{n_{EDL}} \cos \frac{n_{EDL} \pi}{2} + (R_{CT} Q_{EDL} \omega^{n_{EDL}})^2} + \frac{R_{SD}^2 Q_{SD} \omega^{n_{SD}} \cos \frac{n_{SD} \pi}{2}}{1 + 2 R_{SD} Q_{SD} \omega^{n_{SD}} \cos \frac{n_{SD} \pi}{2} + (R_{SD} Q_{SD} \omega^{n_{SD}})^2}. \quad (5.8)$$

**High frequency.** The flat band potential is determined from the polysilicon-dielectric interface, and it is associated with the change in the working state of the electrode. Electrical transport properties such as the current flow through the dielectric are associated with the charge “trap” sites at the polysilicon-dielectric interface. These sites are responsible for capturing electrons from polysilicon, generating an electron depletion region in polysilicon and increasing the availability of electrons that can participate in the transfer processes with the electrolyte [169]. To understand the amount of charges available to participate in the conduction transfer process, the resistance and capacitance were analyzed at  $10^5$  Hz. The chosen frequency corresponds to a short time scale that prevents filling and unfilling of the surface states and, consequently, building up of the double-layer capacitance. For this reason, the circuitry can be simplified as a single capacitor and a single resistor in parallel [164]. The capacitance-voltage (C-V) (Figure 5.16A) and conductance-voltage (G-V) (Figure 5.16B) values were used to determine the flat band potential, the number of donors, and the interface trap density.

The capacitance, C, and the conductance, G, were evaluated using the relationships

$$g = \frac{Re[Z]}{Re[Z]^2 + Im[Z]^2}, \quad (5.9)$$

and

$$C = \frac{-Im[Z]}{\omega(Re[Z]^2 + Im[Z]^2)}, \quad (5.10)$$

at  $10^5$  Hz.  $Im[Z]$  and  $Re[Z]$  are the real and imaginary parts of the impedance  $Z$ , respectively. The conductance and capacitance results (Figure 5.16) confirm that in the accumulation state, the high number of carriers favors higher  $C$  and  $G$  values, while in the depletion state, the lack of carriers leads to lower  $C$  and  $G$  values.

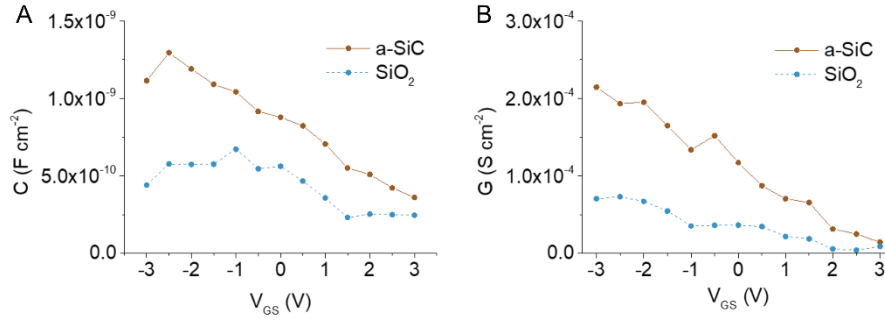


**Figure 5. 16:** C-V and G-V data plots. A) Capacitance-voltage (C-V) and B) conductance-voltage (G-V) data at a high frequency of  $10^5$  Hz evaluated on blank devices.

To determine the flat band voltage  $V_{fb}$  and the number of donors  $N_D$ , it was used the Mott-Schottky plot presented in Figure 5.17A for the polarization potential bias window of -3 V to 3 V. According to Mott-Schottky theory, the capacitance and potential are related by the equation

$$\frac{1}{C^2} = \frac{2}{\epsilon \epsilon_0 A^2 e N_D} \left( V - V_{fb} - \frac{k_B T}{e} \right), \quad (5.11)$$

where  $C$  is the interfacial capacitance,  $A$  is the area exposed to the electrolyte,  $N_D$  is the number of donors or carrier concentration,  $V$  is the applied voltage,  $V_{fb}$  is the flat band potential,  $k_B$  is the Boltzmann's constant,  $T$  is the absolute temperature, and  $e$  is the electronic charge.

The carrier concentration  $N_D$  and  $V_{fb}$  were evaluated by taking the horizontal intercept of the  $1/C^2$  versus  $V$  plot [169]. We estimated  $V_{fb} \sim -0.23$  V for 64 nm a-SiC and  $V_{fb} \sim -0.70$  V for 64 nm  $SiO_2$ . The number of donors was evaluated to be  $N_D \sim 2.8 \times 10^{15}$   $cm^{-3}$  for a-SiC and  $N_D \sim 5.67.8 \times 10^{14}$   $cm^{-3}$  for  $SiO_2$ . The flat band

voltage  $V_{fb}$  indicates the potential needed to neutralize the surface potential at the dielectric/electrolyte interface. The  $V_{fb}$  of the a-SiC blank is lower than that estimated for  $\text{SiO}_2$ . As a consequence, the surface charge exhibited by the a-SiC is lower than that exhibited by the  $\text{SiO}_2$ , confirming the previous results of a low surface charge exhibited by a-SiC in section 3.4. This result represents a positive aspect since a positive surface potential can be switched to a negative surface potential by applying a low potential to the polysilicon. Regarding the number of donors, the slight difference found between a-SiC and  $\text{SiO}_2$  could be due to the roughness of the surface area (reported in Section 5.3.3) exposed to the electrolyte.

The density of interface states, shown in Figure 5.17B, was extracted for a-SiC and  $\text{SiO}_2$  from the G-V [170] data in the depletion [164] state using the equation [171]

$$\frac{G}{\omega} = \frac{e\omega\tau}{1+(\omega\tau)^2}, \quad (5.12)$$

where  $\tau$  represents the recombination lifetime, evaluable as the product of the measured charge transfer resistance  $R_{CT}$  and the dielectric/polysilicon capacitance  $C_{SD}$  at the interface,  $\tau = R_{CT}C_{SD}$ .

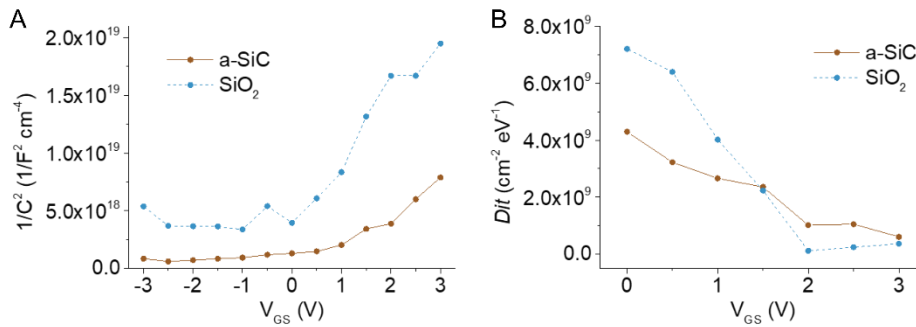


**Figure 5. 17:** Flat band potential and density of states evaluation. A) Mott-Schottky plot for a-SiC and  $\text{SiO}_2$ . Flat band potential evaluation for a-SiC and  $\text{SiO}_2$  electrodes in  $10^{-4}$  M KCl. B) Extracted density of interface states for a-SiC and  $\text{SiO}_2$ .

The density of states indicates the general distribution of the electronic states in terms of energy. It is helpful for understating the conductivity and electrical transport phenomena at the interfaces. The  $D_{it}$  calculated for a-SiC and that for

SiO<sub>2</sub> exhibit similar trends (Figure 5.17B), and the values are low compared with other previously conducted studies [172]. The reason lies in the low ionic strength of the electrolyte used.

To evaluate the charge involved in the electrical transport mechanism, one can use the formula [173]

$$Q_{it} = -e^2 D_{it} V \quad (5.13)$$

where  $e$  is the electron charge and  $V$  is the applied potential. The interface charge density values in the depletion state range from  $-1.6 \times 10^9 \text{ e cm}^{-2}$  to  $-3.56 \times 10^9 \text{ e cm}^{-2}$ . SiO<sub>2</sub> shows  $Q_{it}$  values slightly higher in the range of  $-2.18 \times 10^9 \text{ e cm}^{-2}$  to  $-3.28 \times 10^9 \text{ e cm}^{-2}$ . Due to the direct relationship with the density of states previously evaluated, the charges involved in the transport phenomena are few because of the corresponding low availability of charged ionic species in the electrolytic solution.

## 5.4 Conclusion

This chapter demonstrated the ability of a nanofluidic membrane to electrostatically control charged ions in a monovalent aqueous KCl solution through the application of a potential to the embedded electrode. The DC gating behavior of the nanochannel membrane was initially investigated through the I-V characteristics using  $10^{-5} \text{ M KCl}$ , which exhibits  $\lambda$  comparable to the nanochannel height. Furthermore, gating performances were investigated in the geometry-dictated regime using  $10^{-4} \text{ M KCl}$ . Depending on the polarity of the polarization potential  $V_{GS}$ , the formed EDL favors or hinders ionic transport in the nanochannels. Considering a concentration of  $10^{-4} \text{ M KCl}$ , at  $V_{DS} = -1 \text{ V}$ , the nanochannel conductance was enhanced by 1.5 times for  $V_{GS} = -3 \text{ V}$  and reduced to 0.8 times for  $V_{GS} = 3 \text{ V}$  with a low power consumption ranging from  $1.74 \text{ }\mu\text{W}$  to  $4.2 \text{ }\mu\text{W}$ . Additionally, leakage currents were evaluated in different concentration of PBS solution. The power consumption was estimated between  $1.5 \text{ }\mu\text{W}$  to  $45 \text{ }\mu\text{W}$ . This investigation demonstrated that the nanofluidic membrane can noticeably control ionic species exhibiting a  $\lambda$  that is one-third of the nanochannel height, thus in a geometry-dictated regime. The proven performances could be very useful in

reservoir-based implantable devices, where the drug molecules could exhibit a  $\lambda$  smaller than the nanochannel dimensions due to the high concentration in the drug reservoirs. In this case, the molecules would be transported in the nanochannels in a geometry-dictated regime.

AC electrochemical properties were determined using EIS. By using band diagram theory and associating an LTI electrical circuit with the gated electrode, electrical transport phenomena at the dielectric-electrolyte interface were investigated. The investigation of electrical transport phenomena at the dielectric-electrolyte interface demonstrated that phosphorus-doped polysilicon favors the leakage current for a negative polarization potential due to the accumulation of electrons at the polysilicon-dielectric interface. Further studies need to be conducted to investigate the behavior of the nanochannel membrane when using a p-doped semiconductor electrode. In this case, the acceptor mobility is typically lower in a p-type semiconductor than the donor mobility in the n-type semiconductor, which would reduce the leakage current.

---

## Chapter 6

# In-vitro release of drugs

### Abstract

The new method of molecular release control of the charged particle was developed and characterized with experimental measurements. Measurements were performed by application of the gate potential to the polysilicon electrode, without application of bias transmembrane potential.

The solid-state nanofluidic membrane was investigated by its transport properties. Five molecules were selected as proof of reproducible and repeatable in vitro release modulation: a small fluorophore (Alexa Fluor 647), a large polymer poly(sodium 4-styrenesulfonate), a medically relevant agent (DNA), multi-functional nanoparticles with applicability from bio-labeling to targeted drug delivery (quantum dots), and a first-line therapeutic approach for rheumatoid arthritis (methotrexate).

## 6.1 Introduction

### 6.1.1 Ultraviolet-visible (UV-Vis) Spectroscopy

Ultraviolet-visible (UV-Vis) spectroscopy is a technique that measures the absorbance spectra of a compound in a solution or a solid. The measurements provide the light energy or electromagnetic radiation of the compound in a solution or in a solid through the absorbance. The electrons of the observed compound are excited by the incident light emitted at a specific wavelength, and they move from the ground state to the first singlet excited state. Usually, the energy wavelengths range from 1.5 eV to 6.2 eV, corresponding to 800 nm to 200 nm. The equation that describes the absorbance phenomenon is the Beer-Lambert Law, and it governs the principle behind the absorbance spectroscopy. Considering a single wavelength, the formula can be written in the form:

$$A = \epsilon bc \quad (6.1)$$

where  $A$  is the absorbance, usually indicated unitless, or alternatively as absorbance units or arbitrary units,  $\epsilon$  ( $\text{M}^{-1}\text{cm}^{-1}$ ) is the molar absorptivity of the compound or molecules in solution,  $b$  ( $\text{cm}^{-1}$ ) is the length path of the holder, usually corresponding to a cuvette, and  $c$  ( $\text{M}$ ) is the solution concentration. The UV-Vis instruments are provided with a light source (usually a deuterium or tungsten lamp), a sample holder, and a detector.

Information deducible from UV-Vis spectroscopic measurements provides qualitative and quantitative information of the diluted compound or molecules. To start the measures, irrespective of which information is required, the use of a reference cell fulfilled with only the solvent is necessary to set the starting level or zero level. For the informative quantitative data on the compound, it is required to calibrate the instrument using a known concentration of the mixture under measurement prepared in the same solvent employed for the unknown sample concentration under measurements. For qualitative information regarding the validation of the presence of the compound in the solution, the calibration curve is not required. Despite that, if the measurements are about an over-time study, such as degradation study, or reaction study over time, and the concentration of the



compound in the solution is needed. Thus, characterization of the solution through a calibration curve is required.

The calibration curve is a collection of measurements of at least three concentrations of the compound. The starting concentration should be right above the estimated concentration of the unknown sample and should go down to about one order of magnitude lower than the highest concentration. The concentration should be equally spaced to provide the higher possible accuracy.

## 6.2 Materials and Methods

### 6.2.2 In vitro release fixture

Release modulation experiments were performed with a custom-made, two reservoirs fixture comprising a macro cuvette (sink reservoir) and a drug reservoir. The cuvette was glued with UV epoxy (OG116, Epoxy Technologies, Inc.) to a PMMA (McMaster Carr, Douglasville, GA) membrane holder. The drug reservoir (500  $\mu$ L capacity), made of PMMA, was secured to the membrane holder through 2 SS316L M3 screws. The membrane under testing was clamped between the two PMMA pieces, with 2 O-rings (2418T113, McMaster Carr, Douglasville, GA) to avoid solution leakage. The reservoir was capped with silicone plugs (9277K87, McMaster Carr, Douglasville, GA). The final device is reported in Fig. 6.1.

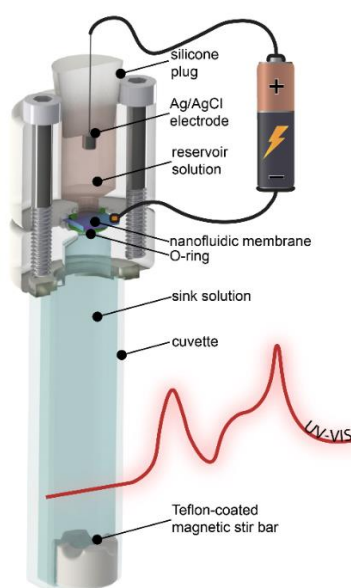


**Figure 6. 1:** Rendering of the custom device used for in-vitro release modulation.

### 6.2.3 In vitro release modulation

Release modulation experiments were performed using 300 nm membranes with both poly-Si and a-SiC deposition. After the electrode connection, membranes were immersed in isopropyl alcohol for 1 h to ensure proper channel wetting, rinsed in deionized H<sub>2</sub>O at least three times, and immersed in a sink solution of 0.01 x PBS overnight. After filling the sink reservoir with 4.45 mL of 0.01 x PBS solution, the membranes were assembled in the diffusion fixture. The source reservoir of the diffusion fixture was loaded with either 300  $\mu$ L/mL Alexa Fluor 647 (Thermo Fisher Scientific, Waltham, MA) (N=1) in 0.01 x PBS, 200  $\mu$ g/mL of Poly(sodium 4-styrenesulfonate) (243051-5G, Sigma Aldrich, St. Louis, MO) in 0.01 x PBS (N=4) or 1 mg/mL of DNA (Deoxyribonucleic acid sodium salt from herring testes; D6898-1G, Sigma Aldrich, St. Louis, MO) in 0.01xPBS (N=2). At pH 7.4, all molecules are negatively charged:  $-3q$  ( $= -4.8 \times 10^{-19}$  C) for Alexa Fluor,  $\sim 380q$  ( $= -608 \times 10^{-19}$  C) for Poly(sodium 4-styrenesulfonate), and highly charged DNA fragment which charge depends on the fragment length. A reference Ag/AgCl pellet electrode (Harvard Apparatus, Holliston, MA) was positioned in the source reservoir.

The assembled diffusion fixtures were then loaded in a custom robotic carousel [174] connected to a Cary 50 UV-vis spectrophotometer (Agilent Technologies). Absorbance measurements of the sink reservoir were automatically performed every 5 minutes. Between each measurement, the sink solution was under constant stirring to ensure sample homogeneity. Wavelengths used for detection were 647 nm for Alexa Fluor, 256 nm for Poly(sodium 4-styrenesulfonate) and 260 nm for DNA. Electrical DC potentials were applied between the reference and the gate electrode using an arbitrary waveform generator (Keysight Technologies 33522A) in a succession of passive (0 V) and active (-1.5 V or -3 V) phases. Phase durations were 12 h and 8 h for passive and active, respectively. Phases were shortened for DNA release, due to its high molar extinction coefficient to 6 h and 4 h for passive and active, respectively[143].

Experimental release of quantum dots and methotrexate were performed using SiC-coated membranes with  $\sim 300$  nm nanochannels. To ensure proper channel

wetting, membranes were immersed in isopropyl alcohol for 1 h and then rinsed three times in deionized H<sub>2</sub>O. Membranes were then placed overnight in 0.01 x PBS or in 1 x PBS in preparation for quantum dots and methotrexate release, respectively. Sink reservoirs (4.45 mL) were filled with matching PBS solutions. After fixture assembly, the source reservoir was loaded with either 1 mg/mL 0.01 x PBS solution of quantum dots (CdTe core-type, COOH functionalized, 777978-10MG, Sigma Aldrich, MO) or 2.5 mg/mL PBS solution of methotrexate (13960, Cayman Chemical, MI). Both molecules possess a negative charge at pH 7.4, with methotrexate presenting a stable -2q charge ( $-3.2 \times 10^{-19}$  C) and quantum dots having a charge that ranges from -5q to -15q depending on pH and ionic strength[175]. Methotrexate has a molar mass of 454 kDa and an estimated diameter of 1.6 nm[176], while quantum dots have an estimated molar mass of 200 kDa and an estimated diameter of 4.7 nm[177]. Ag/AgCl reference electrode (Harvard Apparatus, MA) was used and placed in the source drug reservoir.

Absorbance measurements of every sample were performed at 5 minutes intervals using a custom UV-vis spectrophotometer apparatus consisting of a robotic carousel[174] connected to an Agilent Cary 50 spectrophotometer. Sink solution homogeneity was maintained by constant magnetic stirring (600 rpm). Methotrexate absorbance was measured at 373 nm, while quantum dots at 240 nm. Electrical potential (0, -1.5, or -3 VDC) was applied between the Ag/AgCl and the membrane electrodes through a waveform generator (33522A, Keysight Technologies). Passive (0 V) and active (-1.5 or -3 V) phases were alternated at regular intervals. For methotrexate, phases were alternated every 6 hours between passive and active (0 V and -3 V DC, respectively). For quantum dots, 12 h passive phases were alternated with and 8 h of active applied potential (-1.5 V)[148].

#### **6.2.4 Statistical analysis**

Graphs were plotted and statistical data analyses were performed with GraphPad Prism 8 (version 8.1.1; GraphPad Software, Inc., La Jolla, CA). Data are represented as mean  $\pm$  SD. Statistical significance was determined using two-tailed paired t-tests. For statistical analyses, the cumulative release of each phase was

fitted with a first order polynomial using MATLAB® polyfit function. The resulting angular coefficient represent the release rate of the considered phase[143].

## 6.3 Results

### 6.3.1 In vitro release of Alexa Fluor 647

As a proof of concept for the controlled release of small molecule therapeutics, which represents the vast majority of drugs[178], Alexa Fluor 647 (AF647) was investigated. AF647 is a fluorescent dye that offers high photostability and sensitivity. AF647 presents a molecular weight of ~1kDa and is a good surrogate for charged small molecule therapeutics. The release was performed in a custom-made release fixture (Figure 6.1) where an external voltage generator (represented as a battery) switched the applied voltage between 0 V and -1.5 V in alternating phases.

Figure 6.2 shows the cumulative release for the negatively charged AF647 where the passive (12 h) and the active (8 h) phases are highlighted by the blue and red background, respectively. During the passive phase the molecules are released following a concentration-driven diffusion, achieving a constant release rate. Upon application of the active phase, co-ions repulsion reduces the concentration of negatively charged molecules in the channel, AF647 included, resulting in a reduced transmembrane diffusion. The phase switching is repeated for 14 cycles, demonstrating repeatability of the electrostatic gating phenomena. I observed smooth release rate transitions, which can be attributed to various factors, including i) capacitive charge/discharge of the poly-Si gate; ii) transient formation or dissolution of percolating paths in the dielectric; iii) rearrangement of charged species in nanochannels. While it is difficult to pinpoint the contribution of each of these factors, smooth transitions are desired therapeutic administration. In fact, they can avoid peak-and-though plasma fluctuations that can elicit adverse side effects and negatively impact treatment[25].

For ease of comparison, release rates calculated for each phase from cumulative profiles are plotted in Figure 6.2 (bottom bar graph). To quantify the effect of gating the release rate of each phase (horizontal lines) was averaged and compared the

active to the passive release. A 60% reduction of release rate was observed during active phase and an average release rate of  $\sim 1 \mu\text{g/day}$  during passive phases. Release rates in the order of  $\mu\text{g/day}$  are in line with daily therapeutic doses for numerous small molecule therapeutics. This is the case for glucocorticoids[179], antivirals[180] and hormone therapeutics[181], among others.

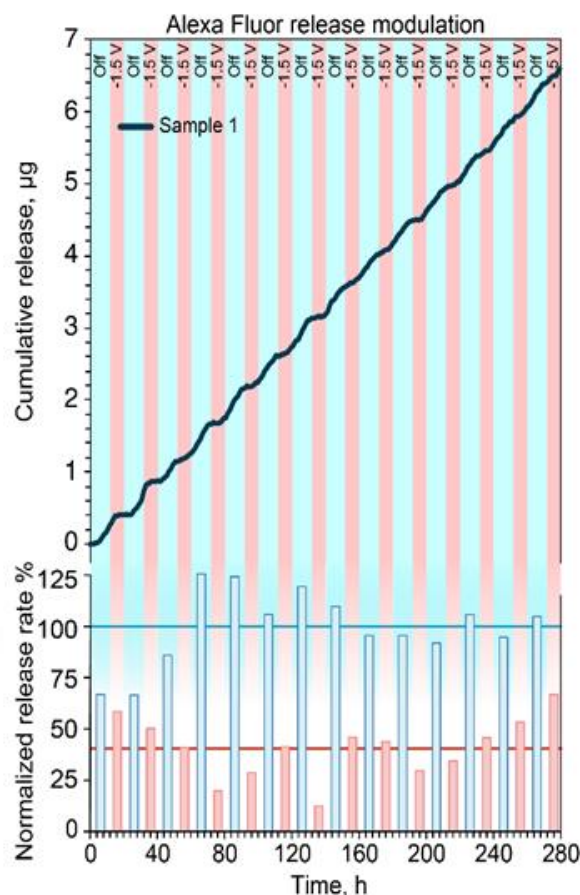


**Figure 6. 2:** Modulated release of Alexa Fluor 647. In-vitro cumulative release modulation of Alexa Fluor (top). Release rate for every phase, normalized to the average of the passive phases. Blue and red line represent the average of the passive and active (-1.5 V) phases respectively.

### 6.3.2 In vitro release modulation of polystyrene sulfonate

More than 40% of newly developed drugs are poorly soluble in water[27,182] and require vehicles for their administration. In this context, to assess the ability of the membrane to modulate the release of larger molecular constructs such as drug

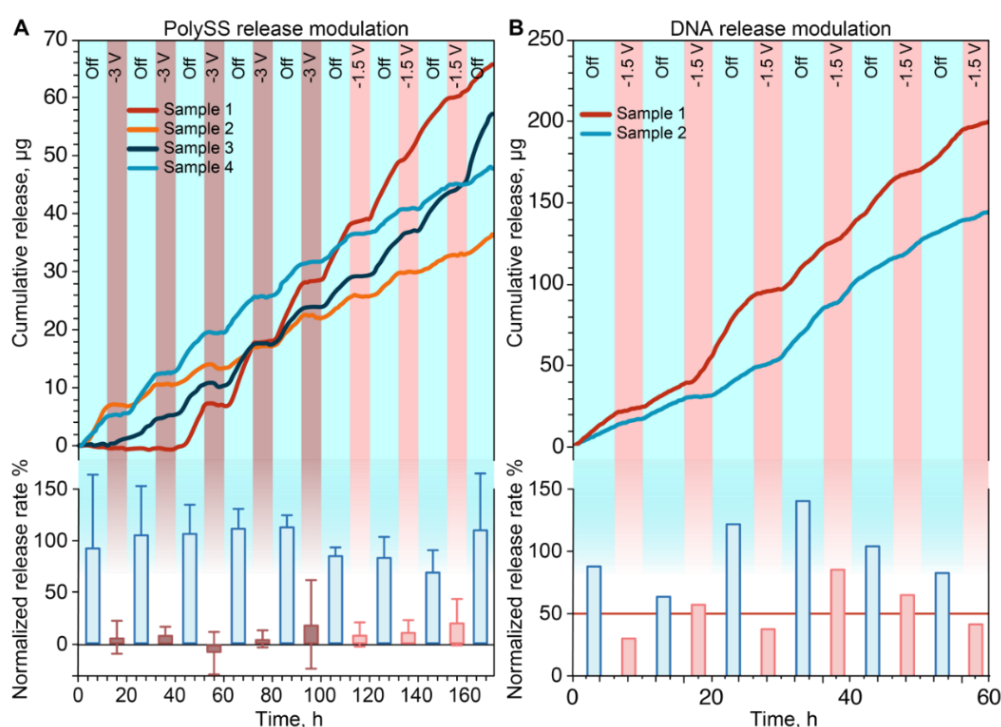
carriers[29,29], poly(sodium 4-styrenesulfonate) was chosen as representative of a large molecule. PolySS (70-1000 kDa) is a polyelectrolyte used for the treatment of acute and chronic kidney disease[183] and for the encapsulation of pharmacologically active compounds that exhibit poor water solubility[184,185]. Additionally, PolySS presents high exposed charge, which allow for effective transport modulation via electrostatic gating.

Figure 6.3A shows the cumulative release of PolySS when alternating passive (blue) and active phases (brown or red). During the first 5 active phases (brown) a voltage of -3 V was applied to the gate electrode, while during the last 3, the voltage was reduced to -1.5 V. As previously shown for AF647, the application of a gate voltage consistently decreased the release rate when compared to the passive phases, where a sustained release was observed. It is important to notice how for -3 V the release rate was almost completely stopped while for -1.5 V the release rate was considerably reduced, but not interrupted. I calculated the slope of each cumulative release and then normalized it to the passive release rate (Figure 6.3A, bottom) to clearly show the differences between the release rates of active and passive phases. More importantly, the reduction and restoring of the release upon change of the applied voltage is consistently repeated demonstrating that electrostatic gating performances do not degrade overtime. During the passive phases, I measured an average release rate of 12  $\mu\text{g}/\text{day}$ , which is clinically relevant in the context of hormone replacement therapies[186]. In these applications, our technology could emulate the function of the body by providing hormone release profiles that mimic the circadian cycle of hormone secretion[187].

### 6.3.3 In vitro release modulation of DNA salt

To demonstrate the controlled delivery of gene therapeutics, a release study with DNA salt as a surrogate for plasmid DNA (pDNA) or small interfering RNA (siRNA) was performed. pDNA and siRNA are the two main vectors used in gene therapy for the treatment of incurable diseases such as cancer or various genetic disorder[188]. Figure 6.3B shows the cumulative release of DNA when alternating passive (blue) and active phases (red). As for the AF647 and PolySS, the application of a negative voltage (-1.5 V) led to a substantial decrease of release rate with respect to the passive phase. Release rate analysis and normalization to the passive

phases (Figure 6.3B bottom) resulted in an average reduction of release rate of 50% of the passive release (Figure 6.3B bottom red line). The passive phase yielded an average release rate of 89  $\mu\text{g}/\text{day}$ . A target therapeutic dose for siRNA cannot be clearly identified, in part due to the fact that gene silencing therapies are still under development[189]. However, this result provides confidence of the ability of the nanofluidic system to function in conjunction with biologics, and control molecular transport at rates that are within the same order of magnitude of experimental therapies[190].



**Figure 6. 3:** Modulated release of Poly(sodium 4-styrenesulfonate) and DNA. A) In-vitro cumulative release modulation of PolySS (top). Release rate for every phase, normalized to the average of the passive phases (bottom). B) In-vitro cumulative release modulation of DNA (top). Release rate for every phase, normalized to the average of the passive phases. Red line represents the average of the active (-1.5 V) phases.

#### 6.3.4 Performance of release modulation through electrostatic gating

To better demonstrate the performance of electrostatic gating, Figure 6.4 shows the normalized release rates of the molecules used in this study, when grouped by

applied voltage. For AF647 the application of -1.5 V resulted in a ~60% reduction of the release rate.

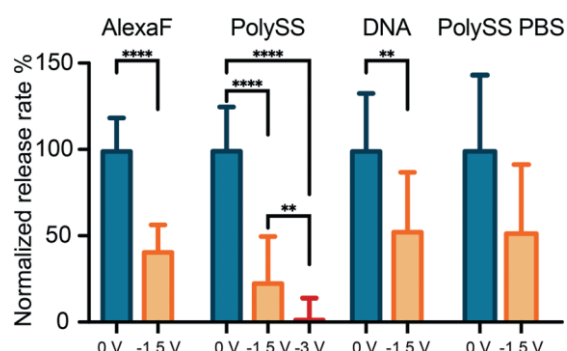


**Figure 6. 4:** Statistical analysis of release modulation. Release rates grouped by typology and compared.

Similarly, for PolySS both applied voltages in the active phases yielded a significant reduction in release rate of 77% and a remarkable 98% for -1.5 V and -3V respectively. Importantly, for PolySS the two active phases lead to a diffusivity reduction proportional to the intensity of the applied voltage, which is easily justifiable by different EDL extents when the surface charge density is changed. In fact, if the EDL extends to the whole nanochannel volume, co-ions repulsion results in an almost complete interruption of analyte diffusion. The analyte charge plays a central role in gating performances, as a higher charge leads to greater repulsion forces. Indeed, our results show that PolySS yielded a more pronounced reduction in release rate compared to AF647 with the application of -1.5 V.

In the case of DNA release, a statistically significant difference in release rate was demonstrated and observed when grouping the calculated slopes by phase typology. In this context, it is remarkable how even despite the presence of the DNA molecules of different lengths, dimensions and overall charge, the gating effect produced by our membrane was consistently and repeatedly able to decrease the diffusion rate through the nanofluidic channels. Nonetheless, it is possible to recognize that the performance achieved with the modulation of DNA is slightly less impressive than the one observed with PolySS. This detail can be attributed to the difference to the lower overall charge of DNA molecules. In fact, even though I expected a 60-70% reduction with the application of 1.5 V, I achieved a 50%



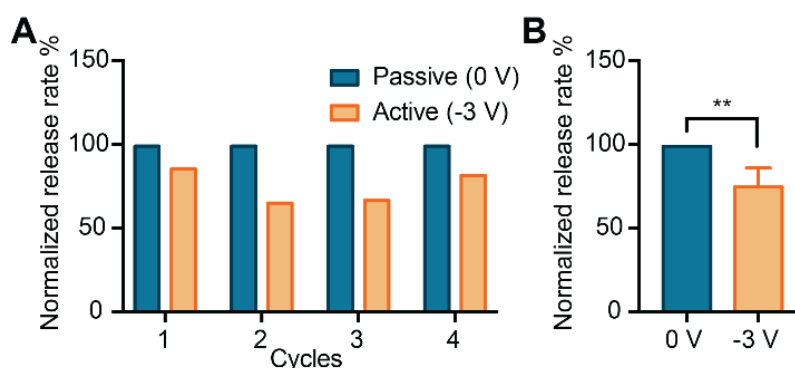
reduction, likely due to small DNA fragments diffusion through the bulk region of the nanochannels.

Figure 6.4 also shows the release rate modulation of polySS in PBS solution. I performed this release as a proof of concept of the ability of our current gated membrane to control drug release in an environment that mimics in vivo ionic strength conditions (1 x PBS). An average reduction of release rate of 55% was achieved with the application of  $-1.5$  V. Even though the modulation (decrease) of release rate results less dramatic as compared to the results obtained with 0.01x PBS (77% decreased release rate), our results indicate that electrostatic gating is a viable strategy for drug release modulation in vivo. Moreover, the same results obtained with 0.01 x PBS could be obtained in high ionic strengths fluids using higher wall potentials or smaller nanochannels. An increasing in the applied potential would increase power consumption. To avoid this problem, the usage of nanofluidic membrane with smaller nanochannels represent a solution for further development of the technology. It is worth mentioning that although in this study, the release modulation was performed for negatively charged molecules. Nevertheless, the nanofluidic membrane can be employed with positive molecules as well. However, our approach to drug release modulation is using electrostatic gating to increase the charge selectivity of channels and effectively generate a reduction in transport of co-ions. In this context, it was an easier test to start from negatively charged nanochannels to further increase the negative surface charge to limit the trans-membrane diffusion of negative charged species. For this reason, this approach favored the an optimization in terms of energy efficiency to modulate drug release. While inverting the native silica surface charge from negative to positive is feasible, this requires higher applied gating potential and high corresponding leakage currents[152]. In turn, this negatively affect the energy efficiency of our system. In light of these consideration, this proof-of-concept focused on adjusting the release rate of negatively charged molecules only. The same principle can be applied to positively charged molecule replacing a-SiC with a material that exposes positive charges, such as alumina[143].

### 6.3.5 In vitro control release of methotrexate

To investigate the effectiveness of electrostatic gating on controlling trans-membrane transport of a small charged analyte, an in vitro diffusion study using methotrexate was performed. Methotrexate has a molecular weight of 454 kDa and is a good representative of small molecules (< 900 Da) therapeutics, which accounts for the majority of pharmaceuticals[178]. Clinically, methotrexate is used as a chemotherapeutic agent for the treatment of various cancers, as well as in the management of rheumatoid arthritis[47].

Figure 6.5A shows the normalized release rates for four consecutive cycles alternating between passive and active phases. During the passive phases, negatively charged molecules (-2q for methotrexate) diffused through the nanochannels freely, largely unaffected by the low native charge of the a-SiC surfaces. When a negative voltage was applied (-3 V), an increase in negative surface charge repelled methotrexate molecules, reducing their release. The four alternation cycles between passive and active phases demonstrated that electrostatic gating allowed for repeatability of release modulation



**Figure 6. 5:** Electrostatically controlled release of methotrexate. A) Normalized release rate of methotrexate for four-cycle between free diffusion (Passive) and gated diffusion (Active). B) Release rate grouped by phase typology.

It was possible to observe a statistically significant (\*\*  $p \leq 0.01$ ) difference in release rate between active and passive phases, whereby the applied potential -3 V yielded a decrease in the release rate of ~35%. During the passive phase, an average release rate of 10  $\mu\text{g/day}$  was obtained, which was consistent with daily doses used

to treat rheumatoid arthritis in pre-clinical testing[191]. Other small molecule therapeutics, including glucocorticoids[179], hormone therapeutics[181], and antivirals[180], present effective daily doses in the order of micrograms. This indicates that the current membrane architecture could, in principle, be adopted for various therapeutic applications. However, further testing with different pharmaceutical agents is warranted[148].

### 6.3.6 In vitro controlled release of quantum dots

To demonstrate the flexibility of our nanofluidic membrane, I performed a release study with quantum dots. Quantum dots have a wide range of applications in vitro and in vivo, including cell labeling for tracking, imaging, or tissue staining[44]. They can also be used as biomarkers for cancer detection and for targeted drug delivery[192]. Quantum dots release was performed with modalities similar to methotrexate, passive (0 V), and active phases (-1.5 V) were alternated for a total of three cycles. Figure 6.6A shows the calculated release rate for each phase.

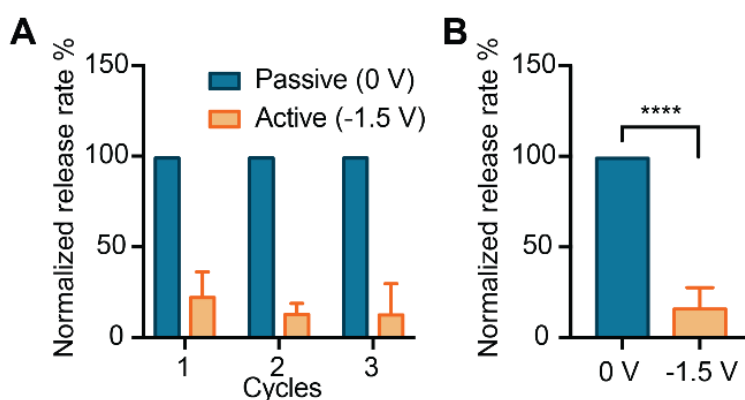


**Figure 6. 6:** Electrostatically controlled release of quantum dots. A) Normalized release rate of quantum dots for three cycles between free diffusion (Passive) and gated diffusion (Active). B) Release rate grouped by phase typology.

As for methotrexate, the application of a negative potential to the gate drastically reduces the release rate of quantum dots through the nanofluidic membrane. Subsequent cycles demonstrate consistent and reproducible release rate reduction.

Grouping the phases by typology Figure 6.6B, I demonstrated a significant difference between passive and active phases with a staggering 84% reduction in release rate. Compared to MTX, quantum dots clearly showed more effective electrostatic modulation, which can be attributed to two main factors: i) QD are COOH functionalized and in a solution with pH 7.4, are likely to exhibit a high surface charge, which makes them prone to electrostatic interactions with the nanochannels surface; ii) the ionic strength of the test solution employed for QD was 0.01xPBS which yields a ten times bigger Debye length compared to 1xPBS, resulting in an evident boost in modulation performance via gating[148].

## 6.4 Conclusion

The a-SiC coated nanofluidic membrane demonstrated the capability to perform a reproducible control of analyte transport via electrostatic gating. The application of a low-intensity electrical potential to the gate electrode allowed to alter nanochannel surface charge, leading to tunable membrane charge selectivity, and control over five therapeutic relevant charged molecules. With this evidence, the a-SiC nanofluidic membrane could be employed as actuators for remotely controlled drug delivery systems. the low voltage needed to modulate the release rate could be provided via small scale and low power circuitry. This investigation might pave the way for the development of the next generation of drug delivery systems, enabling pre-programmed or remotely managed pharmaceutical administration. Further, the gated nanofluidic membrane might find applicability in molecular sieving and lab on a chip diagnostic[143,148].

---

## **Chapter 7**

# **Design of the Printed Circuit Board for drug release control**

### **Abstract**

This chapter focuses on the design of the printed circuit board for remotely control the drug delivery device. The electronic board perform features a Bluetooth Low Energy wireless microcontroller to modulate the gate potential to be applied to the silicon nanofluidic membrane.

## **7.1 Introduction to wireless communication**

In the last decades, implantable devices are widely used for health monitoring and control of physiological functions of the human body. Implanted devices and external equipment can communicate in two ways: utilizing a short wire connection or radiofrequency telemetry. The first case can present some disadvantages such as breakage of wires, infections due to the local implantation, or introduce noise due to accidental mechanical movements. Some examples are related to brain stimulation implantable devices[193] and cardiac devices such as pacemakers and defibrillators[194]. Using the wireless radiofrequency communication, it is possible to avoid those complications[195]. Wireless radiofrequency communication can require significant features to be addressed to provide a real-time monitoring control remote communication. In the following, some aspects such as the type of radiofrequency communication and the power source of the implantable device are discussed.

### **7.1.1 Radio Frequency Communication**

Depending on the medical application, real-time monitoring systems or near real-time monitoring system can require the local storage of data for some period of time. To absolve this aspect, a flash memory can be present on the board to collect the produced data, and lately, transmit to the external device. In fact, direct access to the real-time produced data requires an additional local retriever to connect the implanted device with the external world. This would necessitate a supplementary implanted device placeable through further surgery. In this way, the safety of the patient could be reduced, and at the same time, the cost increases. All in said, to avoid those aspects, the clinical device can feature wireless connectivity to communicate with the external world. Many different technologies and protocols are present on the markets, such as WiFi, ZigBee, and Bluetooth (BLE)[196,197]. In particular, Bluetooth communication can require very low energy and power-saving compared to the other communication protocols[197]. Proprietary and non-proprietary protocols can be implemented with the BLE, and thanks to the extensive implementation and to low cost required from these standards, the biomedical

community is achieving standardized protocols that can be easily suitable for biomedical application such as the remote monitoring control of the implanted devices.

One of the most critical aspects of wireless communication concerns the safety and the electromagnetic interaction with the human body that could affect the wireless signal. In fact, it is demonstrated that organs generally attenuate the Radio Frequency signals[198]. To minimize the signal attenuation, it is possible to work at frequencies below 4 MHz or above 1 GHz[199]. To select the frequency range, one can consider the electromagnetic radiation emitted. Specifically, the Federal Communication Commission established two main categories that classify radiations as ionizing and non-ionizing[200]. The ionizing category, including frequencies in and above ultraviolet range, can cause severe tissue damage. The frequency used by the implantable device is in or below the range of the microwave, and this aspect put the focus on the safety concerns mainly related to the thermal energy produced adsorbed by the tissues surrounding the implanted device[201]. While thermal aspects regulations vary from country to country, the International Telecommunication Union provides frequency bands regulations for local communication to biomedical, manufacturing, and scientific fields[202].

### **7.1.2 Power**

Because the remote-control monitoring system requires a power source to maintain its operative status, the power supply represents one of the most significant aspects to be considered to design an implantable wireless control for the long-term operation properly. Thus, the choice of the power supply has to consider the remote-control system consumption rate, its operational period, and safety considerations. Usually, the most consumer of power can be attributed to wireless communications. In fact, different studies evaluated the power consumption associated with a remote sensing control using the wireless Zigbee protocol was higher than that consumed by the signal processor to control the various sensors located onboard[203]. Many aspects can strongly influence power consumption. In particular, the microcontroller (MCU), the wireless antenna, the signal processing, and the required levels of voltages are among the most important to be considered. The

wireless communication power consumption can be reduced by acting on the signal processing operated by the microcontroller since it is responsible for wireless communication signal processing. Thus, complex signal processing operations can be performed at the receiving devices, meaningfully reducing the computational load to perform on the board. For this purpose, it is possible to use ultra-low power devices such as ARM M0<sup>+</sup> Texas Instrument®. Another possible solution to limit the communication power consumption is implementing a communication protocol that could adequately balance the reliably transmitted data and the data redundancy. For this purpose, the Bluetooth protocols support a linked connection between implanted device and the external receiver device through a secondary transmission.

The power supply of the implantable devices represents a crucial aspect of the lifespan of the device itself. Usually, batteries or supercapacitors are incorporated directly into the implantable device, and their usage allows the implanted device to be independent of an eventual transmitter. The device can be powered and functioning anywhere, for all the lifetime of the battery, such as in the case of pacemakers[204]. As a disadvantage, the battery could significantly increase the dimension of the device, and this aspect could be uncomfortable for the patient.

## **7.2 Drug Delivery Device**

The drug delivery device comprises a drug-based implant that features an electronic board to control the application of the polarization potential to the gated nanofluidic membrane located in the drug reservoir.

### **7.2.1 Remotely controlled nanofluidic implantable platform**

Previously, an accurate experimental investigation was performed on a printed circuit board to evaluate the efficiency on the remote communication via Bluetooth and the life-span of the implantable device[50]. the previous printed circuit board integrated the system-on-chip (SoC) CC2541 (Texas Instrument) and was used for the Bluetooth low energy (BLE) communication since it provides ultra-low energy consumption. The power supply was the commercially available discoidal CR2016



(VARTA), that featured a total capacity of 90mAh. The board was designed with a step-down voltage converter (LM3670, Texas Instrument) used to modulate the power supplied by the battery voltage from 3 V to 1.5 V. two of the available general-purpose input-output GPIO pins P1 and P2 were connected to the electrodes used for the drug modulation. P1 was connected to the converter or the 1.5 V output, while P2 was connected directly to the GPIO for 3 V.

In this study, the power consumption of the PCB was evaluated considering the instant current absorbed by the PCB. The power consumption analysis to estimate the lifespan of the device, was performed by evaluating the different power consumption of the different sources composing the PCB. The circuitry activities can be divided into back-ground use, advertising and communication. Background processing and advertising consumed 97.5  $\mu$ W and 16.5  $\mu$ W during active and passive advertisement state, respectively. Data transmission during connection between the implant and server resulted in significant energy consumption activity estimated to be 1.22 mW. Further, the current flow between the two electrodes for the control of the release of drugs also account for battery depletion. The power consumption associated to the platinum electrode during the control of the release of drugs was evaluated in-vitro using 1xPBS solution. The experimentally measured leakage currents ranged from a few  $\mu$ A to peak of 100  $\mu$ A, corresponding to a maximum power consumption of 150  $\mu$ W. In view of the contribution of these sources of drainage of the battery capable of 270 mWh, the lifetime of the assembled implant in a high-power consumption scenario was estimated to reach 20 days.

The PCB used for this implant was round shaped, with a diameter of 20 mm with a height of 1 mm, while the PEEK embodiment assembled nanofluidic implant was featuring a size of 34 mm x 24 mm x 5.4 mm. The implant capsule was fabricated in polyether ether ketone (PEEK), a widely used biocompatible material resistant to strain[205]. This material was already used for other drug-based devices[50], demonstrating high biocompatibility and low immune response of the tissues surrounding the capsule. It was hosting two separate compartments: one for the membrane that also serves as a drug reservoir and the other for the battery and the

electronics. The reservoir was sealed with a PEED lid where two loading/venting ports were incorporated. Ports were sealed with implantable self-sealing silicon glue (MED3-4213, NuSeal, NuSil Technology) and a biocompatible thermal epoxy (Epotek, 302-3M, Epoxy Technology) was poured on the battery and electronics to embed them into the implant. The membrane was glued in place with biocompatible UV epoxy (OG116, Epoxy Technologies, Inc.). Finally, the lid was sealed with UV epoxy. The described implant is reported in Figure 7.1.

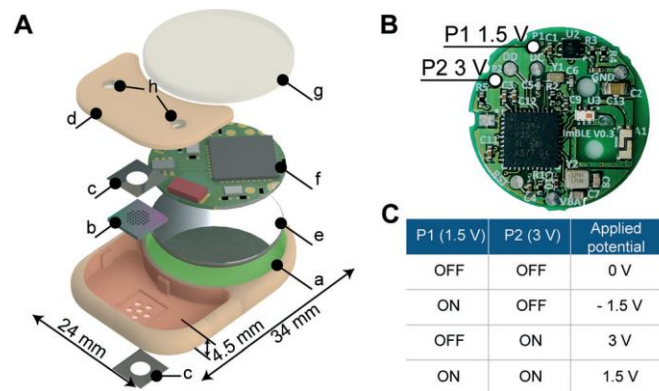


**Figure 7. 1:** Implant components, printed circuit board (PCB) and applied polarization potentials. (A) Exploded view rendering of the implant: a. PEEK body; b. silicon nanofluidic membrane; c. platinum foil electrodes; d. PEEK lid used to seal the drug reservoir; e. battery; f. printed circuit board (PCB); g. epoxy sealant; h. silicone drug filling ports. Red and green highlighted areas are the reservoir compartment and the circuitry chamber, respectively. (B) The printed circuit board (PCB) with the two GPIO pins P1 and P2 highlighted, which can apply 1.5 V and 3 V to the electrodes, respectively. (C) Schematic of possible voltages that can be applied to the membrane.

The new implantable platform of the envisioned implant is reported in Figure 7.2. The capsule is provided with two main compartments. One is reserved for the drug reservoir and the gated nanofluidic membrane, and the other one is dedicated to the discoidal battery. The two compartments would be sealed with implantable self-sealing silicon rubber glue (MED3-4213, NuSeal). The electronic board would be placed right above the two compartments, sealed with the same self-sealing glue. The prototype presents a total volume of  $\sim 2.0$  ml, where the drug reservoir compartment is 350  $\mu$ l. The drug-based device is designed to be powered by the commercially available discoidal VARTA CR2016 battery that features a total

capacity of 90 mAh. The implant is designed to be implanted on small animals such as rats. For this reason, the dimensions have to be restrained compared to the previous developed device reported in Figure 7.1A, that was implanted in rats and monkeys. The final implantable capsule has a length of 22 mm, a width of 14 mm, and a height of 8 mm.

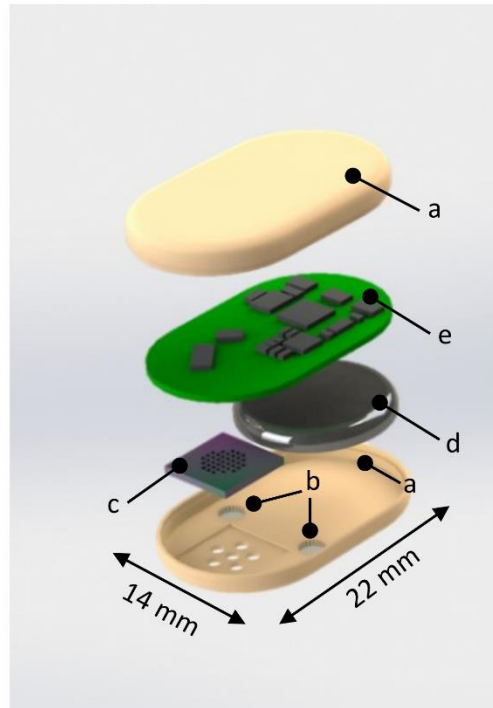


**Figure 7. 2:** Rendering of the implantable capsule. a. PEEK body; b. silicon drug filling ports; c. nanofluidic gated membrane; d. discoidal battery; e. the printed circuit board.

### 7.3 Electronic Printed Circuit Board Design

The custom Printed Circuit Board (PCB) was designed to comply the dimensional constraints required for *in-vivo* implantation. For this reason, the dimensions of the board trace the implantable capsule. In fact, the board features a length of 20 mm, a width of 12 mm, and a height of 423  $\mu\text{m}$ . As in the case of the discoidal board reported in Figure 7.1B, the new the printed circuit board, was designed to provide a remote communication via Bluetooth to allow the control on the application of the electric field to the nanofluidic membrane.

Contemporaneously to the dimension of the board, the other important aspect considered during the design of the PCB was the power consumption. Based on

experimental evaluation performed with the discoidal board[50], the power consumption can be associated to four main categories: the background use, the advertising, the communication and the current flow flowing through the nanofluidic membrane. The activities associated to the background usage, to the advertising and to the communication were assumed to be the same of the previous implanted device. Instead, the power consumption associated with the nanofluidic membrane was estimated through the electrochemical measurement in the physiological solution 1xPBS, where the leakage currents that affected the membrane were evaluated. The results are reported in Chapter 5. The potentials applied during those measurements were in the range of -3 V to 3 V, and the leakage current was evaluated to correspond to few nA to 220  $\mu$ A. The total power consumption in the 1xPBS solution was estimated to be comprised between 1.5  $\mu$ W to 45  $\mu$ W. Compared with the power consumption exhibited by nanofluidic membrane used for the previous implantable platform, the a-SiC membrane exhibited a lower power consumption. The power supply used to design the board was the discoidal battery CR2016 (VARTA) previously used.

The polarization potential applied to the nanofluidic electrode investigated by performing the in-vitro study described in Chapter 6. The polarization potential is generated accordingly to the two phases. Those phases are defined as in the following: one phase corresponding to the zero-order release upon no application of potential, i.e., 0 V, and the other phase corresponding the controlled and reduce release rate of the therapeutics, that requires the application of the polarization potential equal to -1.5 V, and -3 V, depending on the therapeutics.

The electronic design was accomplished by using Altium Designer® software.

***Schematic Design and Components.*** The electrical schematic of the PCB is reported in Figure 7.3. The components are grouped into different sections to highlight the tasks and functions they perform.

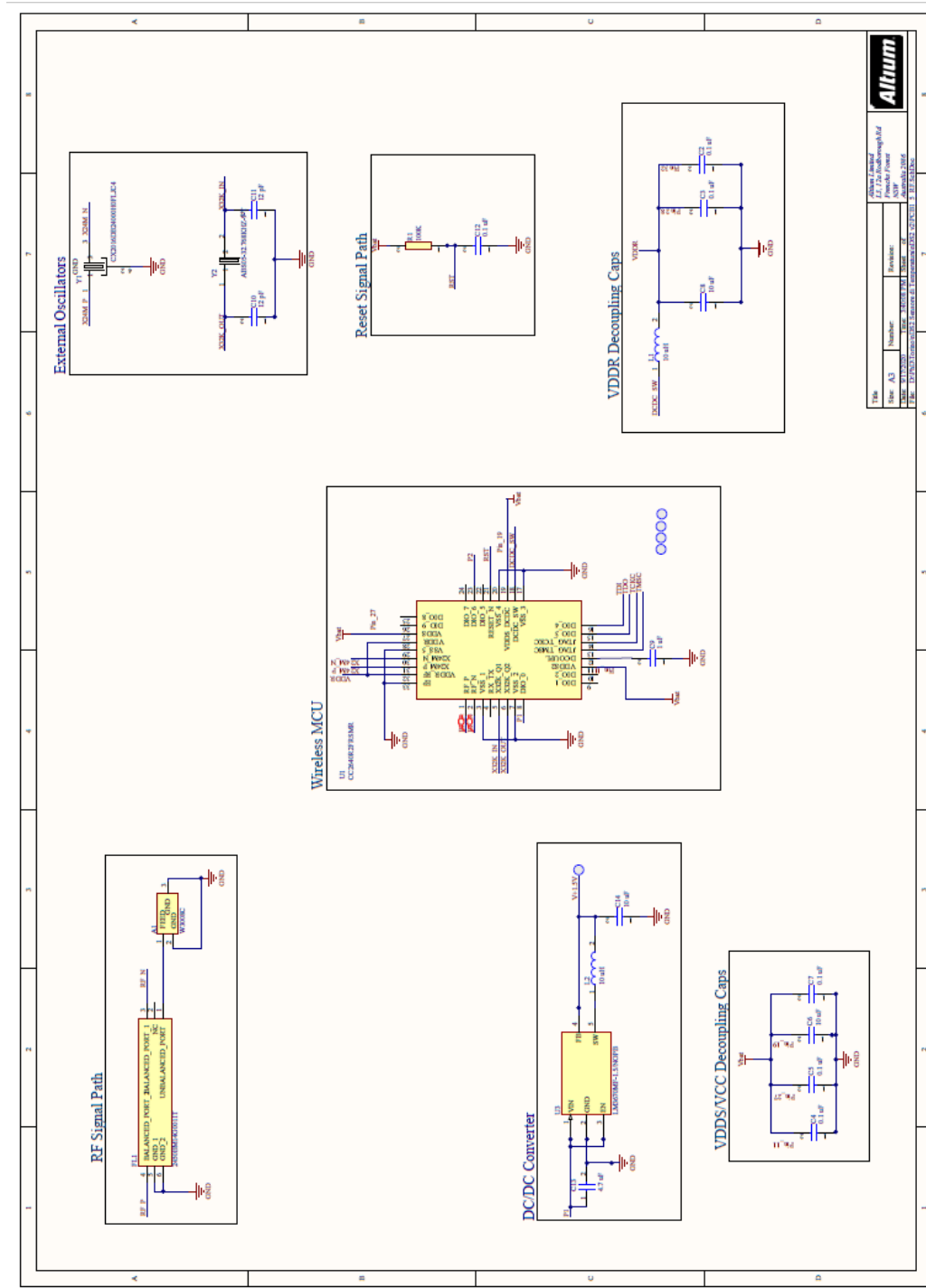


**Figure 7. 3:** Schematic circuit of the printed circuit board.

**Bluetooth Low Energy Microcontroller.** The Bluetooth Low Energy Microcontroller (MCU) employed is the CC2640R2F. It supports the Bluetooth® 5.1 Low Energy 2.4 GHz RF applications. It is widely used in applications that require low-power wireless communication, such as sensing applications and



Figure 7.5. The other two power rails are connected to decoupling circuits comprised of inductances and capacitances. Two crystal oscillators are required: 24 MHz oscillators are used for the RF blocks in power-on mode, while the 32 kHz oscillator is used in power-down mode.

The used antenna is a ceramic chip antenna W3008 adequately connected to the MCU by means of the balun to convert the balanced signal to an unbalanced one. The dedicated PINs for the debug mode are in the number of five: the TCK (Test Clock), the TMS (Test Mode Select), the TDI (Test Data In), and the TDO (Test Data Out). The RESET circuitry connected to the RST PIN is implemented with a pull-up resistor and bypass-capacitor, and it requires to be externally accessible.

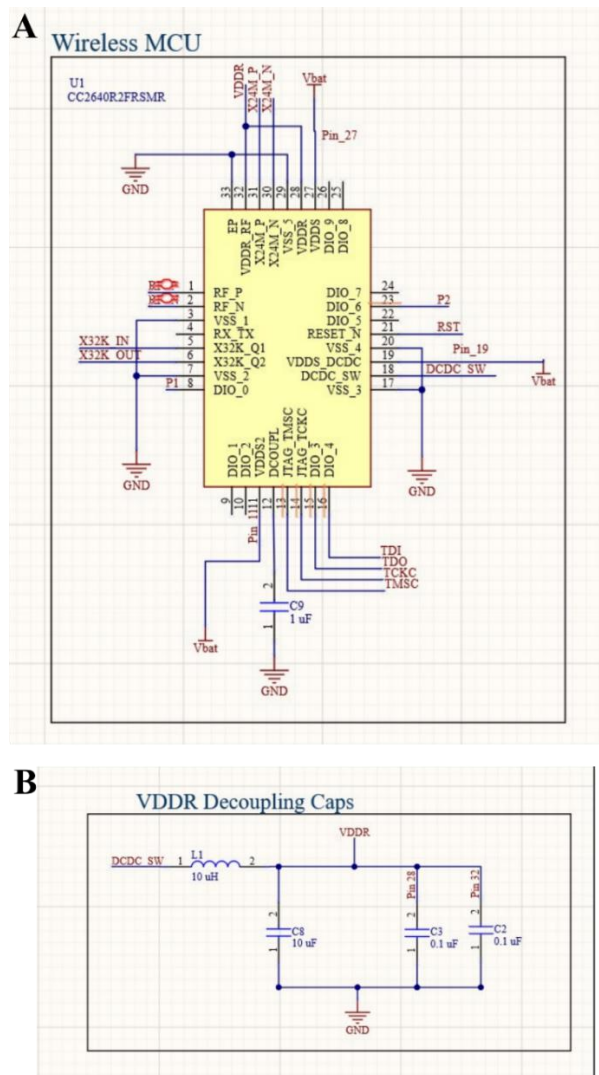


**Figure 7. 5:** Schematic circuit of MCU and VDDR network. A) MCU reporting the pins connection, and B) VDDR Decoupling Capacitors network.

**Radio Frequency Bluetooth Antenna.** The dimension of the PCB requested that the components should present a valid trade-off between their performances and their size. For this reason, the design of the RF block necessitated an antenna capable to provide good performances during the remote communication, reduced power consumption and small dimension.

Mainly, there are three types of antennae used for healthcare, medical applications and remote control: the micro-strip antenna, the metal plate antenna and the chip antenna[206,207]. With the same performances, the first and the second categories present moderate and large dimensions, while the third category feature small size. Consequently, the PCB was implemented by using a chip antenna.

The chip antenna presents important key features very useful for the final purpose of implantable device. Specifically, the antenna exhibits a very compact size, a low cost and an easy implementation on the board, and can be widely used for wireless applications, such as WIFI, and Bluetooth. The crucial aspect to meet the requirement of the performances of the chip antenna is represented by a good design of the feed line, the matching net and the PCB structure. Those aspects requires that the final thickness of the PCB and the routing to feed the antenna must match the typical input impedance value required by the antenna, i.e., 50  $\Omega$ .

The RF block was designed featuring a ceramic chip antenna Pulse Larsen Antenna W3008 exhibiting a compact size 3.2 x 1.6 mm and clearance area of 4.00 x 4.25 mm, and the Johansson Technology balun 2450BM14G0011T 1.6 mm x 0.8 mm. The antenna works in a frequency range of 2.4 - 2.483 GHz, demonstrating a linear max gain of 1.7 dB, and an efficiency of 70% (-1.6 dB). The antenna presents a linear polarization and omnidirectional radiation. To transform the balanced signal to unbalanced signal, it was employed the balun 2450BM14G0011T Johanson Technology compatible with the MCU. The schematic of the RF communication is reported in Figure 7.6.



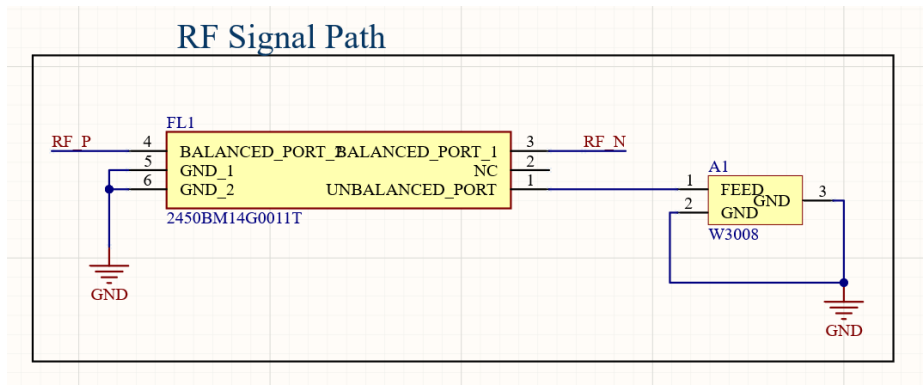


**Figure 7. 6:** Schematic diagram of the electric circuit for the RF communication antenna.

Another important aspect is represented by the radiation pattern in the XY, ZX and YZ plane, that reported in the Figure 7.7A, B and C respectively. The omnidirectional radiation pattern can ensure that the wireless communication can take place on all planes, a crucial characteristic for implantable medical device. In fact, due to the variability of position of the implantation site, the orientation of the device cannot be assured. By using an omnidirectional antenna, the RF signal propagates on the three radiation planes, eliminating the need of a proper orientation of the implanted device.

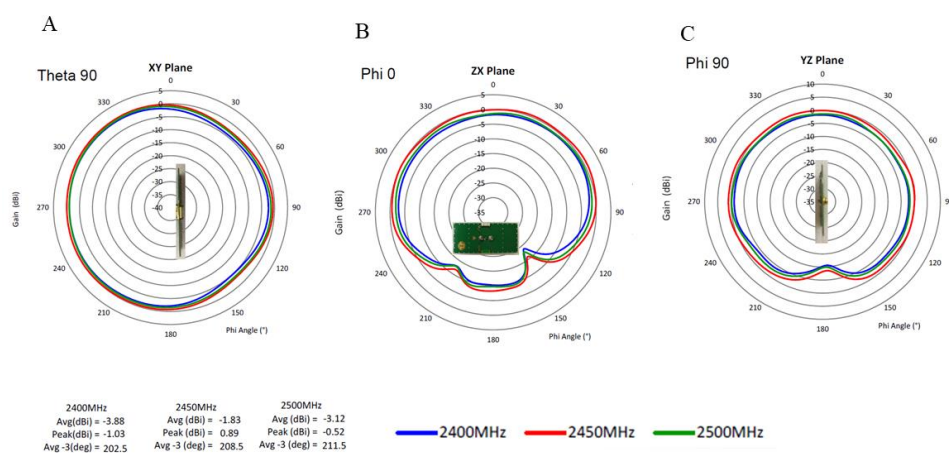


**Figure 7. 7:** Radiation diagram of the ceramic antenna for XY, ZX, and YZ plane.

**Polarization voltage for drug release control.** To polarize the nanofluidic membrane, the polarization potential needs to be applied between the embedded

electrode of the nanofluidic membrane and the reference electrode in the drug reservoir. To solve at this purpose, the usage of a STEP-DOWN (Texas Instruments) DC-DC converter is contemplated. The output of the converter is directly connected with the nanofluidic membrane (P1). The reference electrode instead is linked directly to the GPIO output of the MCU (P2). In order to achieve the different drug release rates, a different combination of P1 and P2 On and OFF status on the PCB allows the application of 4 different voltages, +1.5 V, -1.5 V, +3 V, and 0 V, as illustrated in Figure 7.1C. When both P1 and P2 are ON, the applied voltage to the electrodes is +1.5V; when P1 is On, and P2 is PFF, the applied voltage is -1.5 V; when P1 and P2 are both OFF, the applied voltage is 0 V.

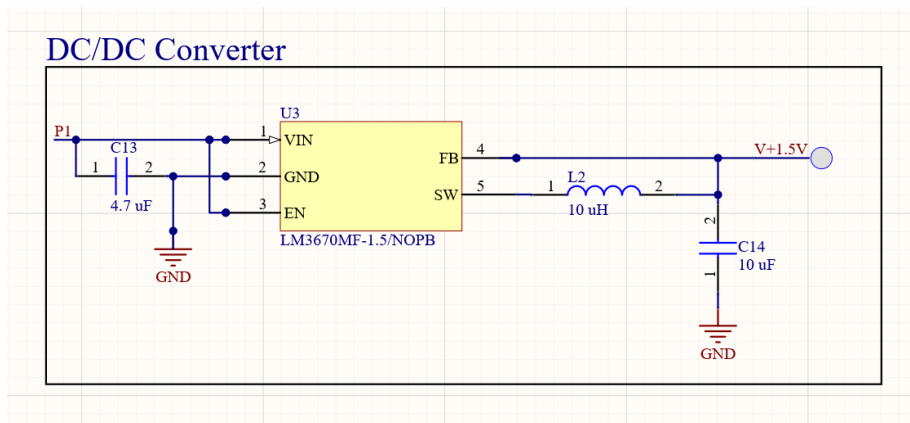


**Figure 7. 8:** Schematic of the electronic circuit for the generation of the polarization potential.

**Printed Circuit Board.** The prototype of the PCB comprised a double-layer compact size PCB containing 22 components on one side and the easy-to-assess pads for the delivery of the polarization signals to the nanofluidic membrane.

In Figure 7.9 is reported the top and the bottom layer of the PCB. It is possible to observe the component placement, the routing, and the via positioning. The distance between components is kept at a minimum of 0.254 mm. The traces connecting the components are all 0.2 mm thick. The antenna trace is designed to have the characteristic impedance of 50  $\Omega$  impedance, and it exhibits a width of 0.65 mm.

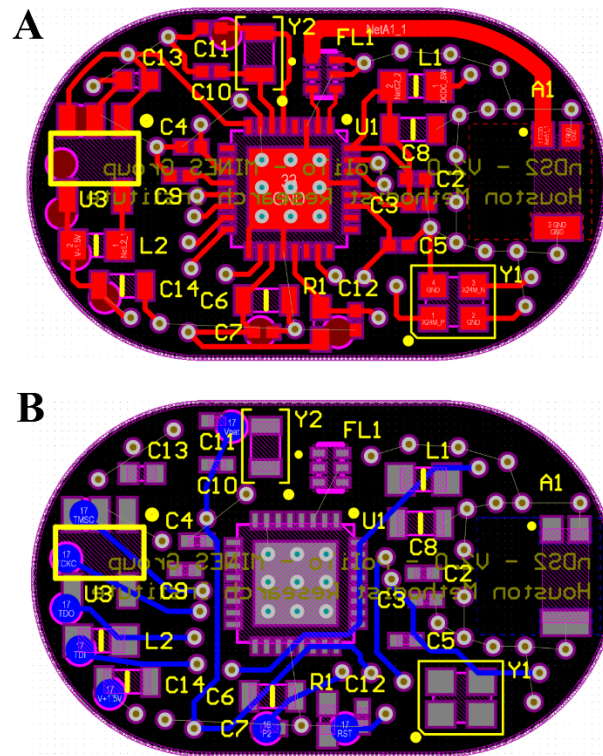


**Figure 7. 9:** Layers of the PCB with highlighting the routing and component placements: A) Top Layer, and B) Bottom Layer.

The used the routing rules, and the manufacturing constraints are reported in Figure 7.10 and 7.11. The cross-section of the layer stack of board is reported in Figure 7.12. The dielectric used is 1 oz copper, that features a thickness of 353  $\mu\text{m}$ . The double layer PCB exhibits a final thickness of 423  $\mu\text{m}$ .

Report Generated From Altium Designer

Name	Priority	Enabled	Type	Category	Scope	Attributes
Assembly/Testpoint	1	True	Assembly Testpoint Style	Testpoint	All	Under Comp - Allow Sides - Top, Bottom Pref Size = 1.524mm Pref Hole Size = 0.813mm Using Grid = Yes Grid = 0.025mm Grid Tolerance = 0mm
Assembly/TestpointUsage	1	True	Assembly Testpoint Usage	Testpoint	All	Testpoint - One Required Multiple - Not Allowed
Clearance	1	True	Clearance	Electrical	All - All	Generic clearance = 0.15mm and 10 value(s) for objects
ComponentClearance	1	True	Component Clearance	Placement	All - All	Horizontal Clearance = 0.15mm Vertical Clearance = 0.15mm
DiffPairsRouting	1	True	Differential Pairs Routing	Routing	All	Pref Gap = 0.15mm Min Gap = 0.15mm Max Gap = 0.254mm Pref Width = 0.15mm Min Width = 0.15mm Max Width = 0.381mm
Fabrication/Testpoint	1	True	Fabrication Testpoint Style	Testpoint	All	Under Comp - Allow Sides - Top, Bottom Pref Size = 1.524mm Pref Hole Size = 0.813mm Using Grid = Yes Grid = 0.025mm Grid Tolerance = 0mm
Fabrication/TestPointUsage	1	True	Fabrication Testpoint Usage	Testpoint	All	Testpoint - One Required Multiple - Not Allowed
Farout_BGA	1	True	Farout Control	Routing	ISBGA	Style - Auto Direction - Alternating In and Out Via Grid = 0.025mm
Height	1	True	Height	Placement	All	Pref Height = 12.7mm Min Height = 0mm Max Height = 25.4mm
HoleSize	1	True	Hole Size	Manufacturing	All	Min = 0.025mm Max = 2.54mm
HoleToHoleClearance	1	True	Hole To Hole Clearance	Manufacturing	All - All	Hole To Hole Clearance = 0.254mm
LaserPairs	1	True	Laser Pairs	Manufacturing	All	Laser Pairs - Enforce
MinimumSolderMaskSilver	1	True	Minimum Solder Mask Silver	Manufacturing	All - All	Minimum Solder Mask Silver = 0.254mm
NetAntennae	1	True	Net Antennae	Manufacturing	All	Net Antennae Tolerance = 0mm
PasteMaskExpansion	1	True	Paste Mask Expansion	Mask	All	Expansion = 0mm
PlaneClearance	1	True	Power Plane Clearance	Plane	All	Clearance = 0.508mm
PlaneConnect	1	True	Power Plane Connect Style	Plane	All	Style - Relief Connect Expansion = 0.508mm Width = 0.254mm Gap = 0.254mm # Entries = 4
PolygonConnect	1	True	Polygon Connect Style	Plane	All - All	Style - Relief Connect Width = 0.254mm Angle = 90 # Entries = 4 All Gap = 0.254mm
RoutingCorners	1	True	Routing Corners	Routing	All	Style - 45 Degree Min Setback = 2.54mm Max Setback = 2.54mm
RoutingLayers	1	True	Routing Layers	Routing	All	Top Layer - Enabled Bottom Layer - Enabled
RoutingPriority	1	True	Routing Priority	Routing	All	Priority = 0
RoutingTopology	1	True	Routing Topology	Routing	All	Topology - Shortest
RoutingVia	1	True	Routing Via Style	Routing	All	Pref Size = 0.508mm Pref Hole Size = 0.254mm
ShortCircuit	1	True	Short Circuit	Electrical	All - All	Short Circuit - Not Allowed
SilkToSilkClearance	1	True	Silk To Silk Clearance	Manufacturing	All - All	Silk To Silk Clearance = 0.1mm
SilkToSolderMaskClearance	1	True	Silk To Solder Mask Clearance	Manufacturing	IsPad - All	Silk To Solder Mask Clearance = 0.254mm
SolderMaskExpansion	1	True	Solder Mask Expansion	Mask	All	Expansion = 0.102mm
UnpouredPolygon	1	True	Modified Polygon	Electrical	All	Allow modified - No Allow shelved - No
UnRoutedNet	1	True	Un-Routed Net	Electrical	All	(No Attributes)
Width	1	True	Width	Routing	All	Pref Width = 0.2mm Min Width = 0.1mm Max Width = 0.7mm
Farout_LCC	2	True	Farout Control	Routing	ISLCC	Style - Auto Direction - Alternating In and Out Via Grid = 0.025mm
Farout_SOIC	3	True	Farout Control	Routing	ISOIC	Style - Auto Direction - Alternating In and Out Via Grid = 0.025mm
Farout_Small	4	True	Farout Control	Routing	(CompPinCount < 5)	Style - Auto Direction - Out Then In Via Grid = 0.025mm
Farout_Default	5	True	Farout Control	Routing	All	Style - Auto Direction - Alternating In and Out Via Grid = 0.025mm

Figure 7. 10: Manufacturing rules and constraints used for design and development of the PCB.

**Report Generated From Altium Designer**

Name	Priority	Enabled	Type	Category	Scope	Attributes
HoleSize	1	True	Hole Size	Manufacturing	All	Min = 0.025mm, Max = 2.54mm
HoleToHoleClearance	1	True	Hole To Hole Clearance	Manufacturing	All - All	Hole To Hole Clearance = 0.254mm
LayerPairs	1	True	Layer Pairs	Manufacturing	All	Layer Pairs - Enforce
MinimumSolderMaskSilver	1	True	Minimum Solder Mask Silver	Manufacturing	All - All	Minimum Solder Mask Silver = 0.254mm
NetAntennae	1	True	Net Antennae	Manufacturing	All	Net Antennae Tolerance = 0mm
SilkToSilkClearance	1	True	Silk To Silk Clearance	Manufacturing	All - All	Silk To Silk Clearance = 0.1mm
SilkToSolderMaskClearance	1	True	Silk To Solder Mask Clearance	Manufacturing	ISPad - All	Silk To Solder Mask Clearance = 0.254mm

**Figure 7. 11:** Manufacturing rules used for the design of the PCB.

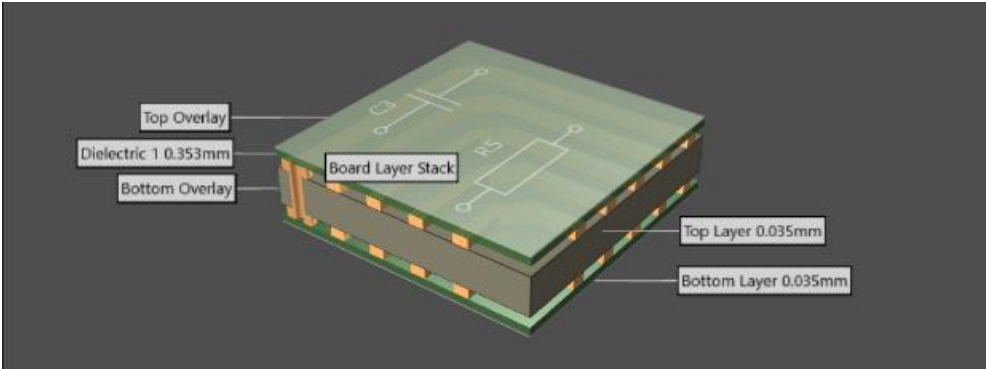


Figure 7. 12: Cross-section of the Board Layer Stack.

Finally, the design was validated by Altium® Designer to verify that all parameters and constraints for the fabrication were respected. The design rule check reported in Figure 7.13 demonstrated that the PCB was properly designed.

Summary	
Warnings	Count
Total	0
Rule Violations	Count
<a href="#">Clearance Constraint (Gap=0.15mm).(All).(All)</a>	0
<a href="#">Short-Circuit Constraint (Allowed=No).(All).(All)</a>	0
<a href="#">Un-Routed Net Constraint (.All).</a>	0
<a href="#">Modified Polygon (Allow modified: No).(Allow shelved: No)</a>	0
<a href="#">Width Constraint (Min=0.1mm).(Max=0.7mm).(Preferred=0.2mm).(All)</a>	0
<a href="#">Power Plane Connect Rule(Relief Connect).(Expansion=0.508mm).(Conductor Width=0.254mm).(Air Gap=0.254mm).(Entries=4).(All)</a>	0
<a href="#">Hole Size Constraint (Min=0.025mm).(Max=2.54mm).(All)</a>	0
<a href="#">Hole To Hole Clearance (Gap=0.254mm).(All).(All)</a>	0
<a href="#">Minimum Solder Mask Sliver (Gap=0.254mm).(All).(All)</a>	0
<a href="#">Silk To Solder Mask (Clearance=0.254mm).(IsPad).(All)</a>	0
<a href="#">Silk to Silk (Clearance=0.1mm).(All).(All)</a>	0
<a href="#">Net Antennae (Tolerance=0mm).(All)</a>	0
<a href="#">Height Constraint (Min=0mm).(Max=25.4mm).(Preferred=12.7mm).(All)</a>	0
Total	0

Figure 7. 13: Report of the rule validation generated by Altium® Designer.



The 3D rendering of the board is reported in Figure 7.14.

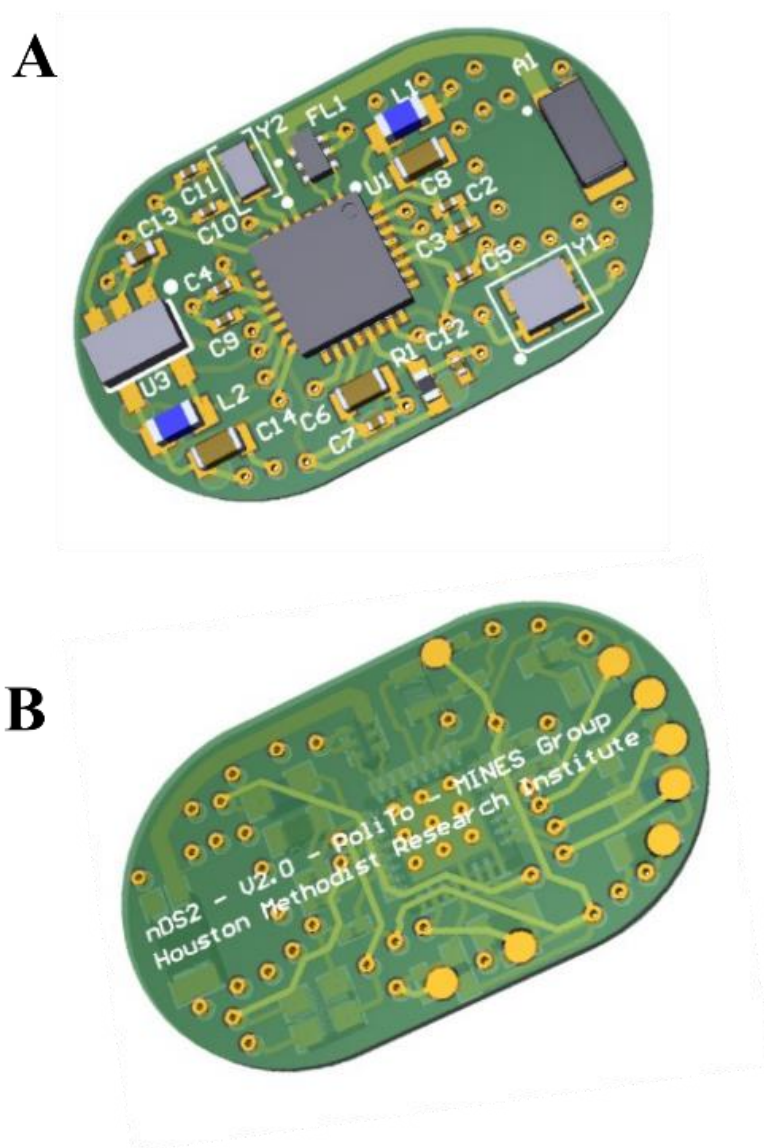


**Figure 7. 14:** 3D rendering of the Printed Circuit Board. A) Top layer, and B) Bottom layer.

## Conclusion

The realized PCB can provide a switching polarization potential from 0V to  $\pm 1.5$  V, and 3 V. To achieve a more refined control over the polarization potential, an increase in resolution to the applied potential could be achieved by implementing

\_\_\_\_\_ Design of the Printed Circuit Board for drug release control

an ADC converted on the board. Additionally, the drug delivery board could be improved by including an element for providing feedback about the chosen release rate. Feedbacks can be implemented by integrating sensors into the board. The system supplied with sensors can achieve a closed-loop control that would enhance the accuracy in delivering the proper dosage of therapeutics.



---

## Chapter 8

# Conclusion and Future Perspectives

The thesis illustrated the fabrication, characterization, and validation of the new silicon gated nanofluidic membrane to electrostatically control charged species and presented the new generation of the nanofluidic implantable device for remote control of the delivery of therapeutics.

First, the manufacturing process was described. The fabrication processes were based on standard microfabrication techniques, such as photolithography and micromachining. It allowed producing a robust nanofluidic structure with 199 round microchannels organized in hexagonal spatial configuration, each connected to 1400 identical nanochannels organized in 19 rows and 96 columns. Each 6 x 6 mm<sup>2</sup> membrane featured 278600 nanochannels, which dimensions can be tailored depending on the medical contingency. The monodispersed nanochannel dimensions represent the key aspect in the tight control of the delivery of drugs, and the large number of nanochannels can ensure molecular transport rates suitable for medical applications. Additionally, the process allowed the fabrication of a uniformly distributed phosphorus-doped polycrystalline buried electrode coated with biocompatible amorphous silicon carbide, which guaranteed the homogeneous distribution of the electric field over the length of the nanochannel.

Second, the experiment conducted in-vitro to simulate the body-fluid conditions was performed to evaluate the rate of corrosion of the amorphous silicon carbide

coating layer in comparison to SiO<sub>2</sub>. Despite the harsh environment, the amorphous silicon carbide demonstrated a negligible corrosion rate over the three experimental conditions. The results of this study demonstrated that the a-SiC coating is an ideal candidate to prevent the degradation of the nanofluidic structure, enhancing the lifetime of the device and making it suitable for long-term implantation.

Third, the gated nanofluidic membrane was electrochemically characterized in monovalent KCl solution and PBS solution. The DC gating behavior was investigated through I-V before using a concentration of the KCl solution exhibiting a Debye length  $\lambda$  comparable to the nanochannels height. Furthermore, electrostatic performances were demonstrated in the geometry dictated regime, where the  $\lambda$  was one-third of the nanochannel height. The results demonstrated that the polarity of the polarization potential is crucial to favor or hinder the ionic transport in the nanochannels and to produce negligible or noticeable leakage current. Power consumption was estimated between a few  $\mu$ W and 45  $\mu$ W. The investigation of the electrical transport phenomena at the dielectric-electrolyte interface was performed. Overall, the outcomes of this study offer significant evidence and support the utility of using the nanofluidic membrane in the reservoir-based implantable devices, where the drug molecules exhibit a  $\lambda$  smaller than the nanochannel dimensions due to the high concentration in the drug reservoirs.

Forth, an in-vitro validation of the active electrostatic control of five medical relevant molecules was illustrated. The release rate variation of the negatively charged molecules Alexa Fluor 647, poly(sodium 4-styrene sulfonate), DNA, quantum dots, and Methotrexate was proved, demonstrating a successful control over the release rate. Upon application of a polarization potential equal to -1.5V, AlexaFluor647 release rate was reduced by 60%, the quantum dots release rate was reduced by 84%, and the DNA release rate was reduced by 50%. Application of -3V the Methotrexate release rate demonstrated a reduction of 35%, while the poly(sodium 4-styrene sulfonate) 98%. Those promising results can be improved to achieve a tunable delivery release rate by shrinking the dimension of the nanochannels and introducing higher resolution for the used polarization potential range.

Fifth, the design of an electronic board to provide remote control via Bluetooth communication was illustrated. The designed board features 400  $\mu\text{m}$  thickness, 12 mm width, and 20 mm length. Those small dimensions allow the development of an implantable reservoir-based capsule suitable for *in-vivo* experiments in small-size animals.

The extension of this project comprises the implantation of the designed board for *in-vivo* tests on remote communication and controlled release of medical relevant molecules previously described. Furthermore, the research group of Professor Grattoni, in collaboration with the research group of MiNES is working on the development of an advanced implantable capsule for the implementation of a wireless network of the implantable sensor. The advanced electronic board will implement a close-loop communication system based on the monitoring of temperature to modulate the release of therapeutic.

In consideration of those encouraging results, the nanofluidic device represents a capable implantable technological platform that may offer a new approach to future medicine through a remote electrostatic active control of drugs and therapeutics. This nanofluidic platform remotely controlled would allow clinical drug administration to cure chronic and acute diseases in a chronotherapeutic regime, personalized medicine, and telemedicine.

---

## References

1. Fine, D.; Grattoni, A.; Goodall, R.; Bansal, S.S.; Chiappini, C.; Hosali, S.; van de Ven, A.L.; Srinivasan, S.; Liu, X.; Godin, B.; et al. Silicon Micro- and Nanofabrication for Medicine. *Adv Healthc Mater* **2013**, *2*, 632–666, doi:10.1002/adhm.201200214.
2. Sprintz, M.; Tasciotti, E.; Allegri, M.; Grattoni, A.; Driver, L.C.; Ferrari, M. Nanomedicine: Ushering in a New Era of Pain Management. *European Journal of Pain Supplements* **2011**, *5*, 317–322, doi:10.1016/j.eujps.2011.08.004.
3. Council, N.R.; Sciences, D. on E. and P.; Initiative, C. for the R. of the N.N. *Small Wonders, Endless Frontiers: A Review of the National Nanotechnology Initiative*; National Academies Press, 2002; ISBN 978-0-309-08454-3.
4. Grattoni, A.; Gill, J.; Zabre, E.; Fine, D.; Hussain, F.; Ferrari, M. Device for Rapid and Agile Measurement of Diffusivity in Micro- and Nanochannels. *Anal. Chem.* **2011**, *83*, 3096–3103, doi:10.1021/ac1033648.
5. Grattoni, A.; Fine, D.; Ziemys, A.; Gill, J.; Zabre, E.; Goodall, R.; Ferrari, M. Nanochannel Systems for Personalized Therapy and Laboratory Diagnostics. *Curr Pharm Biotechnol* **2010**, *11*, 343–365, doi:10.2174/138920110791233280.
6. Eigler, D.M.; Schweizer, E.K. Positioning Single Atoms with a Scanning Tunnelling Microscope. *Nature* **1990**, *344*, 524–526, doi:10.1038/344524a0.
7. Tasciotti, E.; Cabrera, F.J.; Evangelopoulos, M.; Martinez, J.O.; Thekkedath, U.R.; Kloc, M.; Ghobrial, R.M.; Li, X.C.; Grattoni, A.; Ferrari, M. The Emerging Role of Nanotechnology in Cell and Organ Transplantation. *Transplantation* **2016**, *100*, 1629–1638, doi:10.1097/TP.0000000000001100.
8. Sakamoto, J.H.; van de Ven, A.L.; Godin, B.; Blanco, E.; Serda, R.E.; Grattoni, A.; Ziemys, A.; Bouamrani, A.; Hu, T.; Ranganathan, S.I.; et al. Enabling Individualized Therapy through Nanotechnology. *Pharmacol Res* **2010**, *62*, 57–89, doi:10.1016/j.phrs.2009.12.011.

9. Pons-Faudoa, F.P.; Ballerini, A.; Sakamoto, J.; Grattoni, A. Advanced Implantable Drug Delivery Technologies: Transforming the Clinical Landscape of Therapeutics for Chronic Diseases. *Biomed Microdevices* **2019**, *21*, 47, doi:10.1007/s10544-019-0389-6.
10. Malik, N.N. Integration of Diagnostic and Communication Technologies. *J Telemed Telecare* **2009**, *15*, 323–326, doi:10.1258/jtt.2009.009001.
11. Singh, K.; Kim, K.C. Clinical Bio-Micro-Electro-Mechanical Systems: Technology and Applications. *Sensor Letters* **2009**, *7*, 1013–1024, doi:10.1166/sl.2009.1246.
12. Geninatti, T.; Bruno, G.; Barile, B.; Hood, R.L.; Farina, M.; Schmulen, J.; Canavese, G.; Grattoni, A. Impedance Characterization, Degradation, and in Vitro Biocompatibility for Platinum Electrodes on BioMEMS. *Biomed Microdevices* **2015**, *17*, 24, doi:10.1007/s10544-014-9909-6.
13. Wagner, V.; Dullaart, A.; Bock, A.-K.; Zweck, A. The Emerging Nanomedicine Landscape. *Nat Biotechnol* **2006**, *24*, 1211–1217, doi:10.1038/nbt1006-1211.
14. Wang, Y.; Ferrari, M. Surface Modification of Micromachined Silicon Filters. *Journal of Materials Science* **2000**, *35*, 4923–4930, doi:10.1023/A:1004830408749.
15. Popat, K.C.; Eltgroth, M.; LaTempa, T.J.; Grimes, C.A.; Desai, T.A. Decreased Staphylococcus Epidermis Adhesion and Increased Osteoblast Functionality on Antibiotic-Loaded Titania Nanotubes. *Biomaterials* **2007**, *28*, 4880–4888, doi:10.1016/j.biomaterials.2007.07.037.
16. Zhang, M.; Desai, T.; Ferrari, M. Proteins and Cells on PEG Immobilized Silicon Surfaces. *Biomaterials* **1998**, *19*, 953–960, doi:10.1016/S0142-9612(98)00026-X.
17. Desai, T.A.; Hansford, D.J.; Kulinsky, L.; Nashat, A.H.; Rasi, G.; Tu, J.; Wang, Y.; Zhang, M.; Ferrari, M. Nanopore Technology for Biomedical Applications. *Biomedical Microdevices* **1999**, *2*, 11–40, doi:10.1023/A:1009903215959.
18. Sekhar, P.K.; Uwizye, V. Review of sensor and actuator mechanisms for bioMEMS. In *MEMS for Biomedical Applications*; 2012; pp. 46–77 ISBN 978-0-85709-129-1.

19. Ferrati, S.; Fine, D.; You, J.; De Rosa, E.; Hudson, L.; Zabre, E.; Hosali, S.; Zhang, L.; Hickman, C.; Sunder Bansal, S.; et al. Leveraging Nanochannels for Universal, Zero-Order Drug Delivery in Vivo. *Journal of Controlled Release* **2013**, *172*, 1011–1019, doi:10.1016/j.jconrel.2013.09.028.
20. Zhang, C.; Xing, D.; Li, Y. Micropumps, Microvalves, and Micromixers within PCR Microfluidic Chips: Advances and Trends. *Biotechnology Advances* **2007**, *25*, 483–514, doi:10.1016/j.biotechadv.2007.05.003.
21. Chiappini, C.; Martinez, J.O.; De Rosa, E.; Almeida, C.S.; Tasciotti, E.; Stevens, M.M. Biodegradable Nanoneedles for Localized Delivery of Nanoparticles in Vivo: Exploring the Biointerface. *ACS Nano* **2015**, *9*, 5500–5509, doi:10.1021/acs.nano.5b01490.
22. Fine, D.; Grattoni, A.; Hosali, S.; Ziemys, A.; Rosa, E.D.; Gill, J.; Medema, R.; Hudson, L.; Kojic, M.; Milosevic, M.; et al. A Robust Nanofluidic Membrane with Tunable Zero-Order Release for Implantable Dose Specific Drug Delivery. *Lab Chip* **2010**, *10*, 3074–3083, doi:10.1039/C0LC00013B.
23. Scorrano, G.; Bruno, G.; Di Trani, N.; Ferrari, M.; Pimpinelli, A.; Grattoni, A. Gas Flow at the Ultra-Nanoscale: Universal Predictive Model and Validation in Nanochannels of Ångstrom-Level Resolution. *ACS Appl. Mater. Interfaces* **2018**, *10*, 32233–32238, doi:10.1021/acsami.8b11455.
24. Bruno, G.; Di Trani, N.; Hood, R.L.; Zabre, E.; Filgueira, C.S.; Canavese, G.; Jain, P.; Smith, Z.; Demarchi, D.; Hosali, S.; et al. Unexpected Behaviors in Molecular Transport through Size-Controlled Nanochannels down to the Ultra-Nanoscale. *Nature Communications* **2018**, *9*, 1682, doi:10.1038/s41467-018-04133-8.
25. Ahmad, A.; Garnett, W.R. Simulated Fluctuations in Plasma Drug Concentrations for Patients Receiving Oxcarbazepine or Carbamazepine Extended-Release Capsules. *Clin Drug Investig* **2005**, *25*, 669–673, doi:10.2165/00044011-200525100-00006.
26. Ferrati, S.; Nicolov, E.; Bansal, S.; Zabre, E.; Geninatti, T.; Ziemys, A.; Hudson, L.; Ferrari, M.; Goodall, R.; Khera, M.; et al. Delivering Enhanced Testosterone Replacement Therapy through Nanochannels. *Adv Healthc Mater* **2015**, *4*, 446–451, doi:10.1002/adhm.201400348.

27. Pons-Faudoa, F.P.; Sizovs, A.; Di Trani, N.; Paez-Mayorga, J.; Bruno, G.; Rhudy, J.; Manohar, M.; Gwenden, K.; Martini, C.; Chua, C.Y.X.; et al. 2-Hydroxypropyl- $\beta$ -Cyclodextrin-Enhanced Pharmacokinetics of Cabotegravir from a Nanofluidic Implant for HIV Pre-Exposure Prophylaxis. *J Control Release* **2019**, *306*, 89–96, doi:10.1016/j.jconrel.2019.05.037.
28. Chua, C.Y.X.; Jain, P.; Ballerini, A.; Bruno, G.; Hood, R.L.; Gupte, M.; Gao, S.; Di Trani, N.; Susnjar, A.; Shelton, K.; et al. Transcutaneously Refillable Nanofluidic Implant Achieves Sustained Level of Tenofovir Diphosphate for HIV Pre-Exposure Prophylaxis. *J Control Release* **2018**, *286*, 315–325, doi:10.1016/j.jconrel.2018.08.010.
29. Celia, C.; Ferrati, S.; Bansal, S.; van de Ven, A.L.; Ruozi, B.; Zabre, E.; Hosali, S.; Paolino, D.; Sarpietro, M.G.; Fine, D.; et al. Sustained Zero-Order Release of Intact Ultra-Stable Drug-Loaded Liposomes from an Implantable Nanochannel Delivery System. *Adv Healthc Mater* **2014**, *3*, 230–238, doi:10.1002/adhm.201300188.
30. Ballerini, A.; Chua, C.Y.X.; Rhudy, J.; Susnjar, A.; Trani, N.D.; Jain, P.R.; Laue, G.; Lubicka, D.; Shirazi-Fard, Y.; Ferrari, M.; et al. Counteracting Muscle Atrophy on Earth and in Space via Nanofluidics Delivery of Formoterol. *Advanced Therapeutics* **2020**, *3*, 2000014, doi:https://doi.org/10.1002/adtp.202000014.
31. Geninatti, T.; Hood, R.L.; Bruno, G.; Jain, P.; Nicolov, E.; Ziemys, A.; Grattoni, A. Sustained Administration of Hormones Exploiting Nanoconfined Diffusion through Nanochannel Membranes. *Materials (Basel)* **2015**, *8*, 5276–5288, doi:10.3390/ma8085241.
32. Ferrati, S.; Nicolov, E.; Zabre, E.; Geninatti, T.; Shirkey, B.A.; Hudson, L.; Hosali, S.; Crawley, M.; Khera, M.; Palapattu, G.; et al. The Nanochannel Delivery System for Constant Testosterone Replacement Therapy. *J Sex Med* **2015**, *12*, 1375–1380, doi:10.1111/jsm.12897.
33. Filgueira, C.S.; Bruno, G.; Smith, Z.W.; Chua, C.Y.X.; Ballerini, A.; Folci, M.; Gilbert, A.L.; Jain, P.; Sastry, J.K.; Nehete, P.N.; et al. Efficacy of Sustained Delivery of GC-1 from a Nanofluidic System in a Spontaneously Obese Non-Human Primate: A Case Study. *Biomed Microdevices* **2018**, *20*, 49, doi:10.1007/s10544-018-0296-2.

- 
34. Filgueira, C.S.; Nicolov, E.; Hood, R.L.; Ballerini, A.; Garcia-Huidobro, J.; Lin, J.Z.; Fraga, D.; Webb, P.; Sabek, O.M.; Gaber, A.O.; et al. Sustained Zero-Order Delivery of GC-1 from a Nanochannel Membrane Device Alleviates Metabolic Syndrome. *Int J Obes* **2016**, *40*, 1776–1783, doi:10.1038/ijo.2016.129.
35. Liu, H.-C.; Viswanath, D.I.; Pesaresi, F.; Xu, Y.; Zhang, L.; Di Trani, N.; Paez-Mayorga, J.; Hernandez, N.; Wang, Y.; Erm, D.R.; et al. Potentiating Antitumor Efficacy Through Radiation and Sustained Intratumoral Delivery of Anti-CD40 and Anti-PDL1. *Int J Radiat Oncol Biol Phys* **2021**, *110*, 492–506, doi:10.1016/j.ijrobp.2020.07.2326.
36. Chua, C.Y.X.; Jain, P.; Susnjar, A.; Rhudy, J.; Folci, M.; Ballerini, A.; Gilbert, A.; Singh, S.; Bruno, G.; Filgueira, C.S.; et al. Nanofluidic Drug-Eluting Seed for Sustained Intratumoral Immunotherapy in Triple Negative Breast Cancer. *J Control Release* **2018**, *285*, 23–34, doi:10.1016/j.jconrel.2018.06.035.
37. Pons-Faudoa, F.P.; Trani, N.D.; Sizovs, A.; Shelton, K.A.; Momin, Z.; Bushman, L.R.; Xu, J.; Lewis, D.E.; Demaria, S.; Hawkins, T.; et al. Viral Load Reduction in SHIV-Positive Nonhuman Primates via Long-Acting Subcutaneous Tenofovir Alafenamide Fumarate Release from a Nanofluidic Implant. *Pharmaceutics* **2020**, *12*, doi:10.3390/pharmaceutics12100981.
38. Pons-Faudoa, F.P.; Sizovs, A.; Shelton, K.A.; Momin, Z.; Niles, J.A.; Bushman, L.R.; Xu, J.; Chua, C.Y.X.; Nichols, J.E.; Demaria, S.; et al. Preventive Efficacy of a Tenofovir Alafenamide Fumarate Nanofluidic Implant in SHIV-Challenged Nonhuman Primates. *Advanced Therapeutics* **2021**, *4*, 2000163, doi:https://doi.org/10.1002/adtp.202000163.
39. Kittilsland, G.; Stemme, G.; Nordén, B. A Sub-Micron Particle Filter in Silicon. *Sensors and Actuators A: Physical* **1990**, *23*, 904–907, doi:10.1016/0924-4247(90)87056-O.
40. Lesinski, G.B.; Sharma, S.; Varker, K.A.; Sinha, P.; Ferrari, M.; Carson, W.E. Release of Biologically Functional Interferon-Alpha from a Nanochannel Delivery System. *Biomed Microdevices* **2005**, *7*, 71–79, doi:10.1007/s10544-005-6174-8.
41. Paez-Mayorga, J.; Capuani, S.; Hernandez, N.; Farina, M.; Chua, C.Y.X.; Blanchard, R.; Sizovs, A.; Liu, H.-C.; Fraga, D.W.; Niles, J.A.; et al.



- Neovascularized Implantable Cell Homing Encapsulation Platform with Tunable Local Immunosuppressant Delivery for Allogeneic Cell Transplantation. *Biomaterials* **2020**, 257, 120232, doi:10.1016/j.biomaterials.2020.120232.
42. Sabek, O.M.; Ferrati, S.; Fraga, D.W.; Sih, J.; Zabre, E.V.; Fine, D.H.; Ferrari, M.; Gaber, A.O.; Grattoni, A. Characterization of a Nanogland for the Autotransplantation of Human Pancreatic Islets. *Lab Chip* **2013**, 13, 3675–3688, doi:10.1039/C3LC50601K.
43. Sharma, S.; Nijdam, A.J.; Sinha, P.M.; Walczak, R.J.; Liu, X.; Cheng, M.M.-C.; Ferrari, M. Controlled-Release Microchips. *Expert Opinion on Drug Delivery* **2006**, 3, 379–394, doi:10.1517/17425247.3.3.379.
44. Di Trani, N.; Jain, P.; Chua, C.Y.X.; Ho, J.S.; Bruno, G.; Susnjar, A.; Pons-Faudoa, F.P.; Sizovs, A.; Hood, R.L.; Smith, Z.W.; et al. Nanofluidic Microsystem for Sustained Intraocular Delivery of Therapeutics. *Nanomedicine: Nanotechnology, Biology and Medicine* **2019**, 16, 1–9, doi:10.1016/j.nano.2018.11.002.
45. Bruno, G.; Geninatti, T.; Hood, R.L.; Fine, D.; Scorrano, G.; Schmulen, J.; Hosali, S.; Ferrari, M.; Grattoni, A. Leveraging Electrokinetics for the Active Control of Dendritic Fullerene-1 Release across a Nanochannel Membrane. *Nanoscale* **2015**, 7, 5240–5248, doi:10.1039/C4NR06209D.
46. Fine, D.; Grattoni, A.; Zabre, E.; Hussein, F.; Ferrari, M.; Liu, X. A Low-Voltage Electrokinetic Nanochannel Drug Delivery System. *Lab Chip* **2011**, 11, 2526–2534, doi:10.1039/C1LC00001B.
47. Lopez-Olivo, M.A.; Siddhanamatha, H.R.; Shea, B.; Tugwell, P.; Wells, G.A.; Suarez-Almazor, M.E. Methotrexate for Treating Rheumatoid Arthritis. *Cochrane Database Syst Rev* **2014**, CD000957, doi:10.1002/14651858.CD000957.pub2.
48. Bruno, G.; Canavese, G.; Liu, X.; Filgueira, C.S.; Sacco, A.; Demarchi, D.; Ferrari, M.; Grattoni, A. The Active Modulation of Drug Release by an Ionic Field Effect Transistor for an Ultra-Low Power Implantable Nanofluidic System. *Nanoscale* **2016**, 8, 18718–18725, doi:10.1039/C6NR06235K.
49. Grattoni, A.; Tasciotti, E.; Fine, D.; Fernandez-Moure, J.S.; Sakamoto, J.; Hu, Y.; Weiner, B.; Ferrari, M.; Parazynski, S. Nanotechnologies and

- Regenerative Medical Approaches for Space and Terrestrial Medicine. *Aviat Space Environ Med* **2012**, *83*, 1025–1036, doi:10.3357/asem.3307.2012.
50. Di Trani, N.; Silvestri, A.; Bruno, G.; Geninatti, T.; Chua, C.Y.X.; Gilbert, A.; Rizzo, G.; Filgueira, C.S.; Demarchi, D.; Grattoni, A. Remotely Controlled Nanofluidic Implantable Platform for Tunable Drug Delivery. *Lab Chip* **2019**, 10.1039/C9LC00394K, doi:10.1039/C9LC00394K.
51. Darwish, A.; Hassanien, A.E. Wearable and Implantable Wireless Sensor Network Solutions for Healthcare Monitoring. *Sensors (Basel)* **2011**, *11*, 5561–5595, doi:10.3390/s110605561.
52. Merchant Faisal M.; Dec G. William; Singh Jagmeet P. Implantable Sensors for Heart Failure. *Circulation: Arrhythmia and Electrophysiology* **2010**, *3*, 657–667, doi:10.1161/CIRCEP.110.959502.
53. Scholten, K.; Meng, E. A Review of Implantable Biosensors for Closed-Loop Glucose Control and Other Drug Delivery Applications. *Int J Pharm* **2018**, *544*, 319–334, doi:10.1016/j.ijpharm.2018.02.022.
54. Di Trani, N.; Pimpinelli, A.; Grattoni, A. Finite-Size Charged Species Diffusion and PH Change in Nanochannels. *ACS Appl. Mater. Interfaces* **2020**, *12*, 12246–12255, doi:10.1021/acsami.9b19182.
55. Grattoni, A.; Fine, D.; Zabre, E.; Ziemys, A.; Gill, J.; Mackeyev, Y.; Cheney, M.A.; Danila, D.C.; Hosali, S.; Wilson, L.J.; et al. Gated and Near-Surface Diffusion of Charged Fullerenes in Nanochannels. *ACS Nano* **2011**, *5*, 9382–9391, doi:10.1021/nn2037863.
56. Ziemys, A.; Grattoni, A.; Fine, D.; Hussain, F.; Ferrari, M. Confinement Effects on Monosaccharide Transport in Nanochannels. *J. Phys. Chem. B* **2010**, *114*, 11117–11126, doi:10.1021/jp103519d.
57. Israelachvili, J. *Intermolecular and Surface Forces, 3rd Edition*; 2011;
58. Ban, H.; Lin, B.; Song, Z. Effect of Electrical Double Layer on Electric Conductivity and Pressure Drop in a Pressure-Driven Microchannel Flow. *Biomicrofluidics* **2010**, *4*, 014104, doi:10.1063/1.3328091.
59. Grahame, D.C. The Electrical Double Layer and the Theory of Electrocapillarity. *Chem. Rev.* **1947**, *41*, 441–501, doi:10.1021/cr60130a002.
60. Plecis, A.; Schoch, R.B.; Renaud, P. Ionic Transport Phenomena in Nanofluidics: Experimental and Theoretical Study of the Exclusion-

- Enrichment Effect on a Chip. *Nano Lett* **2005**, *5*, 1147–1155, doi:10.1021/nl050265h.
61. Yossifon, G.; Mushenheim, P.; Chang, Y.-C.; Chang, H.-C. Nonlinear Current-Voltage Characteristics of Nanochannels. *Phys. Rev. E* **2009**, *79*, 046305, doi:10.1103/PhysRevE.79.046305.
62. Yossifon, G.; Mushenheim, P.; Chang, H.-C. Controlling Nanoslot Overlimiting Current with the Depth of a Connecting Microchamber. *Europhys Lett* **90**, 64004, doi:10.1209/0295-5075/90/64004.
63. Chang, H.-C.; Yossifon, G.; Demekhin, E.A. Nanoscale Electrokinetics and Microvortices: How Microhydrodynamics Affects Nanofluidic Ion Flux. *Annual Review of Fluid Mechanics* **2012**, *44*, 401–426, doi:10.1146/annurev-fluid-120710-101046.
64. Chang, H.-C.; Yossifon, G. Understanding Electrokinetics at the Nanoscale: A Perspective. *Biomicrofluidics* **2009**, *3*, 012001, doi:10.1063/1.3056045.
65. Sparreboom, W.; van den Berg, A.; Eijkel, J.C.T. Principles and Applications of Nanofluidic Transport. *Nature Nanotech* **2009**, *4*, 713–720, doi:10.1038/nnano.2009.332.
66. Wright, J.C.; Tao Leonard, S.; Stevenson, C.L.; Beck, J.C.; Chen, G.; Jao, R.M.; Johnson, P.A.; Leonard, J.; Skowronski, R.J. An in Vivo/in Vitro Comparison with a Leuprolide Osmotic Implant for the Treatment of Prostate Cancer. *J Control Release* **2001**, *75*, 1–10, doi:10.1016/s0168-3659(01)00358-3.
67. Mani, A.; Zangle, T.A.; Santiago, J.G. On the Propagation of Concentration Polarization from Microchannel–Nanochannel Interfaces Part I: Analytical Model and Characteristic Analysis. *Langmuir* **2009**, *25*, 3898–3908, doi:10.1021/la803317p.
68. Kim, S.J.; Wang, Y.-C.; Lee, J.H.; Jang, H.; Han, J. Concentration Polarization and Nonlinear Electrokinetic Flow near Nanofluidic Channel. *Phys Rev Lett* **2007**, *99*, 044501.
69. Jönsson, A.-S.; Jönsson, B. Ultrafiltration of Colloidal Dispersions—A Theoretical Model of the Concentration Polarization Phenomena. *Journal of Colloid and Interface Science* **1996**, *180*, 504–518, doi:10.1006/jcis.1996.0331.

- 
70. Fan, R.; Yue, M.; Karnik, R.; Majumdar, A.; Yang, P. Polarity Switching and Transient Responses in Single Nanotube Nanofluidic Transistors. *Phys. Rev. Lett.* **2005**, *95*, 086607, doi:10.1103/PhysRevLett.95.086607.
  71. Daiguji, H. Ion Transport in Nanofluidic Channels. *Chem. Soc. Rev.* **2010**, *39*, 901–911, doi:10.1039/B820556F.
  72. G, V.; Rs, S.; Pa, H.; Jm, A.; Mj, C.; R, L. In Vivo Inflammatory and Wound Healing Effects of Gold Electrode Voltammetry for MEMS Micro-Reservoir Drug Delivery Device. *IEEE Trans Biomed Eng* **2004**, *51*, 627–635, doi:10.1109/tbme.2003.821034.
  73. Ke, L.F.; Kc, P.; L, L.; E, M.; Tj, L.T.; Bb, R.; Ca, G.; Ta, D. Biocompatibility of Nanoporous Alumina Membranes for Immunoisolation. *Biomaterials* **2007**, *28*, 2638–2645, doi:10.1016/j.biomaterials.2007.02.010.
  74. Kotzar, G.; Freas, M.; Abel, P.; Fleischman, A.; Roy, S.; Zorman, C.; Moran, J.M.; Melzak, J. Evaluation of MEMS Materials of Construction for Implantable Medical Devices. *Biomaterials* **2002**, *23*, 2737–2750, doi:10.1016/s0142-9612(02)00007-8.
  75. Voskerician, G.; Shive, M.S.; Shawgo, R.S.; von Recum, H.; Anderson, J.M.; Cima, M.J.; Langer, R. Biocompatibility and Biofouling of MEMS Drug Delivery Devices. *Biomaterials* **2003**, *24*, 1959–1967, doi:10.1016/s0142-9612(02)00565-3.
  76. Abdul Rahman, N.A.A.; Zakaria, A.; Jullok, N.; Ma' Radzi, A.H. *Applications of Sensing Material on Quartz Crystal Microbalance in Detection of Volatile Organic Compounds: A Review.*; 2017;
  77. Shana, Z.A.; Radtke, D.E.; Kelkar, U.R.; Haworth, D.T.; Josse, F. Theory and Applications of Quartz Resonators as Sensors for Viscous Conductive Liquids. In Proceedings of the Proceedings., IEEE Ultrasonics Symposium,; October 1989; pp. 567–571 vol.1.
  78. Stratton, F.P.; Chang, D.T.; Kirby, D.J.; Joyce, R.J.; Hsu, T.-Y.; Kubena, R.L.; Yong, Y.-K. A MEMS-Based Quartz Resonator Technology for GHz Applications. In Proceedings of the Proceedings of the 2004 IEEE International Frequency Control Symposium and Exposition, 2004.; August 2004; pp. 27–34.

79. Nimo, A.; Grgić, D.; Ungan, T.; Reindl, L. *A New Family of Passive Wireless RF Harvesters Based on R-C-Quartz Oscillators*; 2013; p. 514;.
80. Mehregany, M.; Zorman, C.A.; Rajan, N.; Wu, C.H. Silicon Carbide MEMS for Harsh Environments. *Proceedings of the IEEE* **86**, 1594–1609.
81. Wang, R.; Young, D. Silicon-Carbide MESFET-Based 400°C MEMS Sensing and Data Telemetry. *Sensors Journal, IEEE* **2006**, *5*, 1389–1394, doi:10.1109/JSEN.2005.858927.
82. Mahmoodi, M.; Ghazanfari, L. Silicon Carbide: A Biocompatible Semiconductor Used in Advanced Biosensors and BioMEMS/NEMS. *Physics and Technology of Silicon Carbide Devices* **2012**, doi:10.5772/51811.
83. Oliveros, A.; Guiseppi-Elie, A.; Sadow, S.E. Silicon Carbide: A Versatile Material for Biosensor Applications. *Biomed Microdevices* **2013**, *15*, 353–368, doi:10.1007/s10544-013-9742-3.
84. Gao, D.; Wijesundara, M.B.J.; Carraro, C.; Howe, R.T.; Maboudian, R. Recent Progress toward a Manufacturable Polycrystalline SiC Surface Micromachining Technology. *IEEE Sensors Journal* **2004**, *4*, 441–448, doi:10.1109/JSEN.2004.828859.
85. Tagawa, N.; Kitamura, K.-I.; Mori, A. Design and Fabrication of MEMS-Based Active Slider Using Double-Layered Composite PZT Thin Film in Hard Disk Drives. *IEEE Transactions on Magnetics* **2003**, *39*, 926–931, doi:10.1109/TMAG.2003.808950.
86. Wang, Z.; Zhu, W.; Zhu, H.; Miao, J.; Chao, C.; Zhao, C.; Tan, O.K. Fabrication and Characterization of Piezoelectric Micromachined Ultrasonic Transducers with Thick Composite PZT Films. *IEEE Transactions on Ultrasonics, Ferroelectrics, and Frequency Control* **2005**, *52*, 2289–2297, doi:10.1109/TUFFC.2005.1563271.
87. Wang, L.-P.; Deng, K.; Zou, L.; Wolf, R.; Davis, R.J.; Trolier-McKinstry, S. Microelectromechanical Systems (MEMS) Accelerometers Using Lead Zirconate Titanate Thick Films. *IEEE Electron Device Letters* **2002**, *23*, 182–184, doi:10.1109/55.992832.
88. Trolier-McKinstry, S.; Muralt, P. Thin Film Piezoelectrics for MEMS. *Journal of Electroceramics* **2004**, *12*, 7–17, doi:10.1023/B:JECR.0000033998.72845.51.

- 
89. Yu, Y.; Ren, T.; Lai, L. High Quality Silicon-Based AlN Thin Films for MEMS Application. *Integrated Ferroelectrics - INTEGR FERROELECTRICS* **2005**, *69*, 367–374, doi:10.1080/10584580590899405.
  90. Pop, P.; Mihoc, G.; Mitu, L. THE SYSTEMIC ANALYSIS OF METALS MANUFACTURING USED IN MEMS FABRICATION. *ANNALS OF THE ORADEA UNIVERSITY. Fascicle of Management and Technological Engineering*. **2011**, *XX (X)*, 2011/2, doi:10.15660/AUOFMTE.2011-2.2275.
  91. Coutu, R.A.; Kladitis, P.E.; Leedy, K.D.; Crane, R.L. Selecting Metal Alloy Electric Contact Materials for MEMS Switches. *J. Micromech. Microeng.* **2004**, *14*, 1157–1164, doi:10.1088/0960-1317/14/8/006.
  92. Deal, B.E.; Grove, A.S. General Relationship for the Thermal Oxidation of Silicon. *Journal of Applied Physics* **1965**, *36*, 3770–3778, doi:10.1063/1.1713945.
  93. Fukuda, T.; Menz, W. *Micro Mechanical Systems: Principles and Technology*; Elsevier, 1998; ISBN 978-0-08-053654-5.
  94. Campbell, S.A.; Campbell, P. in the D. of E. and C.E.S.A. *The Science and Engineering of Microelectronic Fabrication*; Oxford University Press, 1996; ISBN 978-0-19-510508-7.
  95. Thomas, D.G. Semiconductor Integrated Circuit Technology. In *Electronic Materials*; Hannay, N.B., Colombo, U., Eds.; Springer US: Boston, MA, 1973; pp. 563–602 ISBN 978-1-4615-6890-2.
  96. May, G.S.; Sze, S.M. *Fundamentals of Semiconductor Fabrication*; Wiley: New York, 2004; ISBN 978-0-471-23279-7.
  97. Madou, M.J. *Fundamentals of Microfabrication: The Science of Miniaturization, Second Edition*; 2nd ed.; CRC Press: Boca Raton, 2017; ISBN 978-1-315-27422-5.
  98. Petersen, K.E. Silicon as a Mechanical Material. *Proceedings of the IEEE* **1982**, *70*, 420–457, doi:10.1109/PROC.1982.12331.
  99. Williams, K.R.; Gupta, K.; Wasilik, M. Etch Rates for Micromachining Processing-Part II. *Journal of Microelectromechanical Systems* **2003**, *12*, 761–778, doi:10.1109/JMEMS.2003.820936.

100. Williams, K.R.; Member, S.; Muller, R.S.; Fellow, L. Etch Rates for Micromachining Processing. *Journal Of Microelectromechanical Systems* **1996**, *5*, 256–269.
101. Jansen, H.; Gardeniers, H.; Boer, M. de; Elwenspoek, M.; Fluitman, J. A Survey on the Reactive Ion Etching of Silicon in Microtechnology. *J. Micromech. Microeng.* **1996**, *6*, 14–28, doi:10.1088/0960-1317/6/1/002.
102. Walker, M. Comparison of Bosch and Cryogenic Processes for Patterning High-Aspect-Ratio Features in Silicon. *Proceedings of SPIE - The International Society for Optical Engineering* **2001**, *4407*, doi:10.1117/12.425288.
103. Aachboun, S.; Ranson, P.; Hilbert, C.; Boufnichel, M. Cryogenic Etching of Deep Narrow Trenches in Silicon. *Journal of Vacuum Science & Technology A* **2000**, *18*, 1848–1852, doi:10.1116/1.582434.
104. Pruessner, M.W.; Rabinovich, W.S.; Stievater, T.H.; Park, D.; Baldwin, J.W. Cryogenic Etch Process Development for Profile Control of High Aspect-Ratio Submicron Silicon Trenches. *Journal of Vacuum Science & Technology B: Microelectronics and Nanometer Structures Processing, Measurement, and Phenomena* **2006**, *25*, 21–28, doi:10.1116/1.2402151.
105. Krulévitch, K.; Howe, R.T.; Johnson, G.C.; Huang, J. Stress in Undoped LPCVD Polycrystalline Silicon. In Proceedings of the TRANSDUCERS '91: 1991 International Conference on Solid-State Sensors and Actuators. Digest of Technical Papers; June 1991; pp. 949–952.
106. Fan, L.S.; Muller, R.S. As-Deposited Low-Strain LPCVD Polysilicon. In Proceedings of the IEEE Technical Digest on Solid-State Sensor and Actuator Workshop; June 1988; pp. 55–58.
107. McGuire, G. Semiconductor Materials and Process Technology Handbook : For Very Large Scale Integration (VLSI) and Ultra Large Scale Integration (ULSI).; 1988.
108. Siffert, P.; Krimmel, E. *Silicon: Evolution and Future of a Technology*; 2004; ISBN 978-3-642-07356-4.
109. Adenwalla, S.; Welsch, P.; Harken, A.; Brand, J.I.; Sezer, A.; Robertson, B.W. Boron Carbide/n-Silicon Carbide Heterojunction Diodes. *Appl. Phys. Lett.* **2001**, *79*, 4357–4359, doi:10.1063/1.1426257.

- 
110. J., R.P.; Patankar, U.S.; Koel, A.; Nitnaware, V.N. Review of - SiC Wide-Bandgap Heterostructure Properties as an Alternate Semiconductor Material. *AIP Conference Proceedings* **2018**, *1966*, 020011, doi:10.1063/1.5038690.
111. Schwarz, R.; Wang, F.; Eigenschenk, R.; Bollu, M.; Kopetzky, W.; Bernhard, N. Effect of Interface Defects on the Response Time of A-Si:Ha-SiC:H Superlattices. *Superlattices and Microstructures* **1991**, *10*, 147–152, doi:10.1016/0749-6036(91)90220-L.
112. Misaelides, P.; Noli, F.; Riviere, J.P.; Delafond, J. Surface Characterisation and Corrosion Behaviour of SiC-Coated AISI 321 Stainless Steel. *Nuclear Instruments and Methods in Physics Research Section B: Beam Interactions with Materials and Atoms* **1997**, *129*, 221–227, doi:10.1016/S0168-583X(97)00214-0.
113. Jiang, L.; Chen, X.; Wang, X.; Xu, L.; Stubhan, F.; Merkel, K.-H. A-SiC<sub>x</sub>:H Films Deposited by Plasma-Enhanced Chemical Vapor Deposition at Low Temperature Used for Moisture and Corrosion Resistant Applications. *Thin Solid Films* **1999**, *352*, 97–101, doi:10.1016/S0040-6090(99)00363-6.
114. Flannery, A.F.; Mourlas, N.J.; Storment, C.W.; Tsai, S.; Tan, S.H.; Heck, J.; Monk, D.; Kim, T.; Gogoi, B.; Kovacs, G.T.A. PECVD Silicon Carbide as a Chemically Resistant Material for Micromachined Transducers. *Sensors and Actuators A: Physical* **1998**, *70*, 48–55, doi:10.1016/S0924-4247(98)00111-3.
115. Auditore, A.; Satriano, C.; Coscia, U.; Ambrosone, G.; Parisi, V.; Marletta, G. Human Serum Albumin Adsorption onto A-SiC:H and a-C:H Thin Films Deposited by Plasma Enhanced Chemical Vapor Deposition. *Biomolecular Engineering* **2002**, *19*, 85–90, doi:10.1016/S1389-0344(02)00042-4.
116. Amon, M.; Bolt, A.; Heublein, B.; Schaldach, M. Coating of Cardiovascular Stents with Amorphous Silicon Carbide to Reduce Thrombogenicity. In Proceedings of the Proceedings of 16th Annual International Conference of the IEEE Engineering in Medicine and Biology Society; November 1994; Vol. 2, pp. 838–839 vol.2.
117. Bullo, J.; Schmidt, M.P. Physics of Amorphous Silicon–Carbon Alloys. *physica status solidi (b)* **1987**, *143*, 345–418, doi:10.1002/pssb.2221430202.



118. McCulloch, D.G.; Merchant, A.R.; Marks, N.A.; Cooper, N.C.; Fitzhenry, P.; Bilek, M.M.M.; McKenzie, D.R. Wannier Function Analysis of Tetrahedral Amorphous Networks. *Diamond and Related Materials* **2003**, *12*, 2026–2031, doi:10.1016/S0925-9635(03)00196-1.
119. Ivashchenko, V.I.; Turchi, P.E.A.; Shevchenko, V.I.; Ivashchenko, L.A.; Rusakov, G.V. Tight-Binding-Molecular-Dynamics Investigation of the Atomic and Electronic Structure Properties of a-C, a-Si and a-SiC. *Diamond and Related Materials* **2003**, *12*, 993–997, doi:10.1016/S0925-9635(02)00271-6.
120. Ivashchenko, V.; Shevchenko, V. Atomic and Electronic Structure of A-SiC. *Semiconductor Physics, Quantum Electronics and Optoelectronics* **2002**, *5*, doi:10.15407/spqeo5.01.016.
121. Grattoni, A.; Rosa, E.D.; Ferrati, S.; Wang, Z.; Giancesini, A.; Liu, X.; Hussain, F.; Goodall, R.; Ferrari, M. Analysis of a Nanochanneled Membrane Structure through Convective Gas Flow. *J. Micromech. Microeng.* **2009**, *19*, 115018, doi:10.1088/0960-1317/19/11/115018.
122. Jeon, G.; Yang, S.Y.; Byun, J.; Kim, J.K. Electrically Actuable Smart Nanoporous Membrane for Pulsatile Drug Release. *Nano Lett* **2011**, *11*, 1284–1288, doi:10.1021/nl104329y.
123. Kim, S.; Ozalp, E.I.; Darwish, M.; Weldon, J.A. Electrically Gated Nanoporous Membranes for Smart Molecular Flow Control. *Nanoscale* **2018**, *10*, 20740–20747, doi:10.1039/C8NR05906C.
124. Prakash, S.; Conlisk, A.T. Field Effect Nanofluidics. *Lab Chip* **2016**, *16*, 3855–3865, doi:10.1039/C6LC00688D.
125. Goldstein, J.; GOLDSTEIN, J.A.; Lyman, Newbury, D.E.; Joy, D.C.; Echlin, P.; Lyman, C.E.; Lifshin, E.; Sawyer, L.; Joy, O.R.N.L.D.S. and D.E.M.F.D.C.; et al. *Scanning Electron Microscopy and X-Ray Microanalysis: Third Edition*; Springer US, 2003; ISBN 978-0-306-47292-3.
126. M.A, H.G.J.M. XCIII. The High-Frequency Spectra of the Elements. *The London, Edinburgh, and Dublin Philosophical Magazine and Journal of Science* **1913**, *26*, 1024–1034, doi:10.1080/14786441308635052.
127. Zukor, L.J. Nature and Properties of Engineering Materials. Z. D. Jastrzebski. Wiley, New York-London, 1959, Xvii + 571 Pp. \$11.00. *Journal of Applied*

- 
- Polymer Science* **1960**, *4*, 372–373, doi:<https://doi.org/10.1002/app.1960.070041224>.
128. Jellison, G.E. Ellipsometry. In *Encyclopedia of Spectroscopy and Spectrometry*; Lindon, J.C., Ed.; Elsevier: Oxford, 1999; pp. 402–411 ISBN 978-0-12-226680-5.
  129. Lissberger, P.H. Ellipsometry and Polarised Light. *Nature* **1977**, *269*, 270–270, doi:10.1038/269270a0.
  130. Kanduti, D.; Sterbenk, P.; Artnik, B. FLUORIDE: A REVIEW OF USE AND EFFECTS ON HEALTH. *Mater Sociomed* **2016**, *28*, 133–137, doi:10.5455/msm.2016.28.133-137.
  131. Lee, Y.K.; Yu, K.J.; Song, E.; Barati Farimani, A.; Vitale, F.; Xie, Z.; Yoon, Y.; Kim, Y.; Richardson, A.; Luan, H.; et al. Dissolution of Monocrystalline Silicon Nanomembranes and Their Use as Encapsulation Layers and Electrical Interfaces in Water-Soluble Electronics. *ACS Nano* **2017**, *11*, 12562–12572, doi:10.1021/acsnano.7b06697.
  132. Connors, K.A. *Chemical Kinetics: The Study of Reaction Rates in Solution*; Wiley, 1990; ISBN 978-0-471-72020-1.
  133. Zhou, D.; Mech, B.; Greenberg, R. Accelerated Corrosion Tests on Silicon Wafers for Implantable Medical Devices. *Proceedings of 198th Electrochemical Society Meeting* **2000**, Vol. 363.
  134. Crundwell, F.K. On the Mechanism of the Dissolution of Quartz and Silica in Aqueous Solutions. *ACS Omega* **2017**, *2*, 1116–1127, doi:10.1021/acsomega.7b00019.
  135. Guyer, E.; Eiselstein, L.; Verghese, P. Accelerated Testing of Active Implantable Medical Devices. *NACE - International Corrosion Conference Series* **2009**.
  136. Rutili, G.; Arfors, K.-E. Protein Concentration in Interstitial and Lymphatic Fluids from the Subcutaneous Tissue. *Acta Physiologica Scandinavica* **1977**, *99*, 1–8, doi:<https://doi.org/10.1111/j.1748-1716.1977.tb10345.x>.
  137. Wiśniewska, M.; Szewczuk-Karpisz, K.; Sternik, D. Adsorption and Thermal Properties of the Bovine Serum Albumin–Silicon Dioxide System. *J Therm Anal Calorim* **2015**, *120*, 1355–1364, doi:10.1007/s10973-014-4300-7.
-

138. Wilson, A.H.; Dirac, P.A.M. The Theory of Electronic Semi-Conductors. *Proceedings of the Royal Society of London. Series A, Containing Papers of a Mathematical and Physical Character* **1931**, *133*, 458–491, doi:10.1098/rspa.1931.0162.
139. Wilson, A.H.; Fowler, R.H. The Theory of Electronic Semi-Conductors. - II. *Proceedings of the Royal Society of London. Series A, Containing Papers of a Mathematical and Physical Character* **1931**, *134*, 277–287, doi:10.1098/rspa.1931.0196.
140. Nevill, M. Conduction in Amorphous Materials. *Electronics and Power* **1973**, *19*, 321–324, doi:10.1049/ep.1973.0382.
141. Street, R.A. *Hydrogenated Amorphous Silicon*; Cambridge University Press, 2005; ISBN 978-0-521-01934-7.
142. Leidl, B.; Schmidt, G.; Pobegen, G.; Knoll, P.; Krenn, H. Conduction Mechanisms in Hydrogenated Amorphous Silicon Carbide. *Journal of Non-Crystalline Solids* **2020**, *528*, 119750, doi:10.1016/j.jnoncrysol.2019.119750.
143. Trani, N.D.; Silvestri, A.; Sizovs, A.; Wang, Y.; Erm, D.R.; Demarchi, D.; Liu, X.; Grattoni, A. Electrostatically Gated Nanofluidic Membrane for Ultra-Low Power Controlled Drug Delivery. *Lab Chip* **2020**, *20*, 1562–1576, doi:10.1039/D0LC00121J.
144. abu-Rjal, R.; Chinarian, V.; Bazant, M.Z.; Rubinstein, I.; Zaltzman, B. Effect of Concentration Polarization on Permselectivity. *Phys. Rev. E* **2014**, *89*, 012302, doi:10.1103/PhysRevE.89.012302.
145. Jin, X.; Aluru, N.R. Gated Transport in Nanofluidic Devices. *Microfluid Nanofluid* **2011**, *11*, 297–306, doi:10.1007/s10404-011-0796-3.
146. Schoch, R.B.; Renaud, P. Ion Transport through Nanoslits Dominated by the Effective Surface Charge. *Appl. Phys. Lett.* **2005**, *86*, 253111, doi:10.1063/1.1954899.
147. Grosjean, A.; Rezrazi, M.; Tachez, M. Study of the Surface Charge of Silicon Carbide (SiC) Particles for Electroless Composite Deposits: Nickel-SiC. *Surface and Coatings Technology* **1997**, *96*, 300–304, doi:10.1016/S0257-8972(97)00180-1.
148. Di Trani, N.; Silvestri, A.; Wang, Y.; Demarchi, D.; Liu, X.; Grattoni, A. Silicon Nanofluidic Membrane for Electrostatic Control of Drugs and

- Analytes Elution. *Pharmaceutics* **2020**, *12*, 679, doi:10.3390/pharmaceutics12070679.
149. Karnik, R.; Fan, R.; Yue, M.; Li, D.; Yang, P.; Majumdar, A. Electrostatic Control of Ions and Molecules in Nanofluidic Transistors. *Nano Lett.* **2005**, *5*, 943–948, doi:10.1021/nl050493b.
150. Jiang, Z.; Stein, D. Electrofluidic Gating of a Chemically Reactive Surface. *Langmuir* **2010**, *26*, 8161–8173, doi:10.1021/la9044682.
151. Fan, R.; Huh, S.; Yan, R.; Arnold, J.; Yang, P. Gated Proton Transport in Aligned Mesoporous Silica Films. *Nat Mater* **2008**, *7*, 303–307, doi:10.1038/nmat2127.
152. Schoch, R.B.; Han, J.; Renaud, P. Transport Phenomena in Nanofluidics. *Rev. Mod. Phys.* **2008**, *80*, 839–883, doi:10.1103/RevModPhys.80.839.
153. Zhu, F.; Hu, J.; Matulionis, I.; Deutsch, T.; Gaillard, N.; Kunrath, A.; Miller, E.; Madan, A. Amorphous Silicon Carbide Photoelectrode for Hydrogen Production Directly from Water Using Sunlight. *Philosophical Magazine* **2009**, *89*, 2723–2739, doi:10.1080/14786430902740729.
154. Matulionis, I.; Zhu, F.; Hu, J.; Deutsch, T.; Kunrath, A.; Miller, E.; Marsen, B.; Madan, A. Development of a Corrosion-Resistant Amorphous Silicon Carbide Photoelectrode for Solar-to-Hydrogen Photovoltaic/Photoelectrochemical Devices. *Proceedings of SPIE - The International Society for Optical Engineering* **2008**, doi:10.1117/12.794287.
155. Magafas, L.; Georgoulas, N.; Thanailakis, A. Electrical Properties of A-SiC/c-Si(p) Heterojunctions. *Semicond. Sci. Technol.* **1992**, *7*, 1363–1368, doi:10.1088/0268-1242/7/11/014.
156. Robertson, J. High Dielectric Constant Gate Oxides for Metal Oxide Si Transistors. *Rep. Prog. Phys.* **2005**, *69*, 327–396, doi:10.1088/0034-4885/69/2/R02.
157. Tang, T.-A.; Institute of Electrical and Electronics Engineers; Beijing Section; Fu dan da xue; International Conference on Solid-State and Integrated Circuit Technology; ICSICT *12th IEEE International Conference on Solid-State and Integrated Circuit Technology (ICSICT)*, 2014 28-31 Oct. 2014, Guilin, China; 2014; ISBN 978-1-4799-3284-9.

158. Padovani, A.; Gao, D.Z.; Shluger, A.L.; Larcher, L. A Microscopic Mechanism of Dielectric Breakdown in SiO<sub>2</sub> Films: An Insight from Multi-Scale Modeling. *Journal of Applied Physics* **2017**, *121*, 155101, doi:10.1063/1.4979915.
159. Yao, J.; Zhong, L.; Natelson, D.; Tour, J.M. In Situ Imaging of the Conducting Filament in a Silicon Oxide Resistive Switch. *Sci Rep* **2012**, *2*, 1–5, doi:10.1038/srep00242.
160. Tung, C.H.; Pey, K.L.; Tang, L.J.; Radhakrishnan, M.K.; Lin, W.H.; Palumbo, F.; Lombardo, S. Percolation Path and Dielectric-Breakdown-Induced-Epitaxy Evolution during Ultrathin Gate Dielectric Breakdown Transient. *Appl. Phys. Lett.* **2003**, *83*, 2223–2225, doi:10.1063/1.1611649.
161. Godet, J.; Pasquarello, A. Proton Diffusion Mechanism in Amorphous SiO<sub>2</sub>. *Phys. Rev. Lett.* **2006**, *97*, 155901, doi:10.1103/PhysRevLett.97.155901.
162. Yun, J.; Cho, Y.-B.; Jang, W.; Lee, J.G.; Shin, S.J.; Han, S.H.; Lee, Y.; Chung, T.D. Dielectric Breakdown and Post-Breakdown Dissolution of Si/SiO<sub>2</sub> Cathodes in Acidic Aqueous Electrochemical Environment. *Sci Rep* **2018**, *8*, doi:10.1038/s41598-018-20247-x.
163. Chen, X.; Wang, H.; Sun, G.; Ma, X.; Gao, J.; Wu, W. Resistive Switching Characteristic of Electrolyte-Oxide-Semiconductor Structures. *J. Semicond.* **2017**, *38*, 084003, doi:10.1088/1674-4926/38/8/084003.
164. Meng, A.C.; Tang, K.; Braun, M.R.; Zhang, L.; McIntyre, P.C. Electrochemical Impedance Spectroscopy for Quantitative Interface State Characterization of Planar and Nanostructured Semiconductor-Dielectric Interfaces. *Nanotechnology* **2017**, *28*, 415704, doi:10.1088/1361-6528/aa842b.
165. Ovshinsky, S.R. The Role of Free Radicals in the Formation of Amorphous Thin Films. In *Disordered Materials: Science and Technology*; Adler, D., Schwartz, B.B., Silver, M., Eds.; Institute for Amorphous Studies Series; Springer US: Boston, MA, 1991; pp. 114–119 ISBN 978-1-4684-8745-9.
166. Višćor, P.; Olsen, N.B. Frequency and Time Response in Relaxation Time Semiconductors. *Journal of Non-Crystalline Solids* **1987**, *90*, 25–28, doi:10.1016/S0022-3093(87)80377-0.

- 
167. Málek, J.; Shánělová, J. Structural Relaxation in Amorphous Materials. In *Properties and Applications of Amorphous Materials*; Thorpe, M.F., Tichý, L., Eds.; NATO Science Series; Springer Netherlands: Dordrecht, 2001; pp. 35–44 ISBN 978-94-010-0914-0.
168. Orton, J. *Polycrystalline and Amorphous Semiconductors*; Oxford University Press; ISBN 978-0-19-171297-5.
169. Nicollian, E.H.; Brews, J.R. *MOS (Metal Oxide Semiconductor) Physics and Technology*; Wiley–Blackwell: New York, 1982; ISBN 978-0-471-08500-3.
170. Nicollian, E.H.; Goetzberger, A. The Si-SiO<sub>2</sub> Interface — Electrical Properties as Determined by the Metal-Insulator-Silicon Conductance Technique. *Bell System Technical Journal* **1967**, *46*, 1055–1133, doi:<https://doi.org/10.1002/j.1538-7305.1967.tb01727.x>.
171. Schroder, D. *Semiconductor Material and Device Characterization*; 1990.
172. JUAN, H.L. Structural and Electrical Characterisations of Amorphous Silicon Carbide Films. Thesis, 2005.
173. Munakata, C.; Nishimatsu, S. Analysis of Ac Surface Photovoltages in a Depleted Oxidized P-Type Silicon Wafer. *Jpn. J. Appl. Phys.* **1986**, *25*, 807, doi:10.1143/JJAP.25.807.
174. Geninatti, T.; Small, E.; Grattoni, A. Robotic UV-Vis Apparatus for Long-Term Characterization of Drug Release from Nanochannels. *Meas. Sci. Technol.* **2014**, *25*, 027003, doi:10.1088/0957-0233/25/2/027003.
175. Voráčová, I.; Klepárník, K.; Lišková, M.; Foret, F. Determination of  $\zeta$ -Potential, Charge, and Number of Organic Ligands on the Surface of Water Soluble Quantum Dots by Capillary Electrophoresis. *Electrophoresis* **2015**, *36*, 867–874, doi:10.1002/elps.201400459.
176. Swain, M. Chemicalize.Org. *J. Chem. Inf. Model.* **2012**, *52*, 613–615, doi:10.1021/ci300046g.
177. Haro-González, P.; Martínez-Maestro, L.; Martín, I.R.; García-Solé, J.; Jaque, D. High-Sensitivity Fluorescence Lifetime Thermal Sensing Based on CdTe Quantum Dots. *Small* **2012**, *8*, 2652–2658, doi:<https://doi.org/10.1002/sml.201102736>.

178. Veber, D.F.; Johnson, S.R.; Cheng, H.-Y.; Smith, B.R.; Ward, K.W.; Kopple, K.D. Molecular Properties That Influence the Oral Bioavailability of Drug Candidates. *J. Med. Chem.* **2002**, *45*, 2615–2623, doi:10.1021/jm020017n.
179. Yasin, M.N.; Svirskis, D.; Seyfoddin, A.; Rupenthal, I.D. Implants for Drug Delivery to the Posterior Segment of the Eye: A Focus on Stimuli-Responsive and Tunable Release Systems. *J Control Release* **2014**, *196*, 208–221, doi:10.1016/j.jconrel.2014.09.030.
180. Charles, N.C.; Steiner, G.C. Ganciclovir Intraocular Implant. A Clinicopathologic Study. *Ophthalmology* **1996**, *103*, 416–421, doi:10.1016/s0161-6420(96)30677-5.
181. Langer, R.D. Efficacy, Safety, and Tolerability of Low-Dose Hormone Therapy in Managing Menopausal Symptoms. *J Am Board Fam Med* **2009**, *22*, 563–573, doi:10.3122/jabfm.2009.05.080134.
182. Savjani, K.T.; Gajjar, A.K.; Savjani, J.K. Drug Solubility: Importance and Enhancement Techniques. *ISRN Pharm* **2012**, *2012*, 195727, doi:10.5402/2012/195727.
183. Burton, M.J.; Voluse, A.C.; Patel, A.B.; Konkle-Parker, D. Measuring Adherence to Hepatitis C Direct-Acting Antiviral Medications: Using the VAS in an HCV Treatment Clinic. *South Med J* **2018**, *111*, 45–50, doi:10.14423/SMJ.00000000000000750.
184. Em, S.; Dg, S. LbL Coated Microcapsules for Delivering Lipid-Based Drugs. *Adv Drug Deliv Rev* **2011**, *63*, 837–846, doi:10.1016/j.addr.2011.03.009.
185. Zhang, J.; Li, C.; Wang, Y.; Zhuo, R.-X.; Zhang, X.-Z. Controllable Exploding Microcapsules as Drug Carriers. *Chem. Commun.* **2011**, *47*, 4457–4459, doi:10.1039/C1CC10337G.
186. Mashchak, C.A.; Lobo, R.A.; Dozono-Takano, R.; Eggena, P.; Nakamura, R.M.; Brenner, P.F.; Mishell, D.R. Comparison of Pharmacodynamic Properties of Various Estrogen Formulations. *Am J Obstet Gynecol* **1982**, *144*, 511–518, doi:10.1016/0002-9378(82)90218-6.
187. Lee, S.H.; Piao, H.; Cho, Y.C.; Kim, S.-N.; Choi, G.; Kim, C.R.; Ji, H.B.; Park, C.G.; Lee, C.; Shin, C.I.; et al. Implantable Multireservoir Device with Stimulus-Responsive Membrane for on-Demand and Pulsatile Delivery of

- Growth Hormone. *PNAS* **2019**, *116*, 11664–11672, doi:10.1073/pnas.1906931116.
188. Scholz, C.; Wagner, E. Therapeutic Plasmid DNA versus SiRNA Delivery: Common and Different Tasks for Synthetic Carriers. *J Control Release* **2012**, *161*, 554–565, doi:10.1016/j.jconrel.2011.11.014.
  189. Chernikov, I.V.; Vlassov, V.V.; Chernolovskaya, E.L. Current Development of SiRNA Bioconjugates: From Research to the Clinic. *Front. Pharmacol.* **2019**, *10*, doi:10.3389/fphar.2019.00444.
  190. Kumar, S.R.; Markusic, D.M.; Biswas, M.; High, K.A.; Herzog, R.W. Clinical Development of Gene Therapy: Results and Lessons from Recent Successes. *Mol Ther Methods Clin Dev* **2016**, *3*, 16034, doi:10.1038/mtm.2016.34.
  191. Liu, D.-Y.; Lon, H.-K.; Wang, Y.-L.; DuBois, D.C.; Almon, R.R.; Jusko, W.J. Pharmacokinetics, Pharmacodynamics and Toxicities of Methotrexate in Healthy and Collagen-Induced Arthritic Rats. *Biopharmaceutics & Drug Disposition* **2013**, *34*, 203–214, doi:10.1002/bdd.1838.
  192. Fine, D.; Grattoni, A.; Hosali, S.; Ziemys, A.; Rosa, E.D.; Gill, J.; Medema, R.; Hudson, L.; Kojic, M.; Milosevic, M.; et al. A Robust Nanofluidic Membrane with Tunable Zero-Order Release for Implantable Dose Specific Drug Delivery. *Lab on a Chip* **2010**, *10*, 3074–3083, doi:10.1039/C0LC00013B.
  193. Benabid, A.L.; Chabardes, S.; Mitrofanis, J.; Pollak, P. Deep Brain Stimulation of the Subthalamic Nucleus for the Treatment of Parkinson's Disease. *Lancet Neurol* **2009**, *8*, 67–81, doi:10.1016/S1474-4422(08)70291-6.
  194. Hauser, R.G.; Katsiyannis, W.T.; Gornick, C.C.; Almquist, A.K.; Kallinen, L.M. Deaths and Cardiovascular Injuries Due to Device-Assisted Implantable Cardioverter-Defibrillator and Pacemaker Lead Extraction. *Europace* **2010**, *12*, 395–401, doi:10.1093/europace/eup375.
  195. Orlov, M.V.; Szombathy, T.; Chaudhry, G.M.; Haffajee, C.I. Remote Surveillance of Implantable Cardiac Devices. *Pacing Clin Electrophysiol* **2009**, *32*, 928–939, doi:10.1111/j.1540-8159.2009.02412.x.



196. Dangi, K.; Yadav, M.; Malhotra, S. Health Care Monitoring System an Application of IOT Using WI-FI. *International Journal of Engineering & Technology* **2018**, *7*, 560, doi:10.14419/ijet.v7i4.5.21157.
197. Baker, N. ZigBee and Bluetooth: Strengths and Weaknesses for Industrial Applications. *Computing & Control Engineering Journal* **2005**, *16*, 20–25, doi:10.1049/ccej:20050204.
198. Gabriel, C.; Gabriel, S.; Corthout, E. The Dielectric Properties of Biological Tissues: I. Literature Survey. *Physics in medicine and biology* **1996**, *41*, 2231–49, doi:10.1088/0031-9155/41/11/001.
199. Yekeh, K.; Kohno, R. Wireless Communications for Body Implanted Medical Device. *2007 Asia-Pacific Microwave Conference* **2007**, doi:10.1109/APMC.2007.4554534.
200. RF Safety FAQ Available online: <https://www.fcc.gov/engineering-technology/electromagnetic-compatibility-division/radio-frequency-safety/faq/rf-safety> (accessed on 19 April 2021).
201. Bercich, R.A.; Duffy, D.R.; Irazoqui, P.P. Far-Field RF Powering of Implantable Devices: Safety Considerations. *IEEE Trans Biomed Eng* **2013**, *60*, 2107–2112, doi:10.1109/TBME.2013.2246787.
202. Radio Regulations Available online: <https://www.itu.int:443/en/publications/ITU-R/Pages/publications.aspx>
203. Ó Mathúna, S.C.; O'Donnell, T.; Martinez-Catala, R.V.; Rohan, J.F.; O'Flynn, B. Energy Scavenging for Long-Term Deployable Wireless Sensor Networks. *Talanta* **2007**, *75*, 613–623, doi:10.1016/j.talanta.2007.12.021.
204. Katz, D.; Akiyama, T. Pacemaker Longevity: The World's Longest-Lasting VVI Pacemaker. *Ann Noninvasive Electrocardiol* **2007**, *12*, 223–226, doi:10.1111/j.1542-474X.2007.00165.x.
205. Williams, D. Polyetheretherketone for Long-Term Implantable Devices. *Medical device technology* **2008**, *19*, 8, 10–1, doi:10.1049/ic:20080578.
206. Soliman, M.M.; Chowdhury, M.E.H.; Khandakar, A.; Islam, M.T.; Qiblawey, Y.; Musharavati, F.; Zal Nezhad, E. Review on Medical Implantable Antenna Technology and Imminent Research Challenges. *Sensors* **2021**, *21*, 3163, doi:10.3390/s21093163.

207. Damaj, A.W.; El Misilmani, H.M.; Chahine, S.A. Implantable Antennas for Biomedical Applications: An Overview on Alternative Antenna Design Methods and Challenges. In Proceedings of the 2018 International Conference on High Performance Computing Simulation (HPCS); July 2018; pp. 31–37.

---

## List of publications

1. **Silvestri, A.**; Di Trani, N.; Canavese, G., Motto Ros, P.; Iannucci, L.; Grassini, S.; Wang, Y.; Liu, X.; Demarchi, D.; Grattoni, A. Silicon carbide gated nanofluidic membrane for active control of electrokinetic ionic transport. *Membranes* (Submitted).
2. Trani, N. D.\*; **Silvestri, A.\***; Sizovs, A.; Wang, Y.; Erm, D. R.; Demarchi, D.; Liu, X.; Grattoni, A. Electrostatically Gated Nanofluidic Membrane for Ultra-Low Power Controlled Drug Delivery. *Lab Chip* **2020**, *20* (9), 1562–1576. <https://doi.org/10.1039/D0LC00121J>.
3. Di Trani, N.; **Silvestri, A.**; Wang, Y.; Demarchi, D.; Liu, X.; Grattoni, A. Silicon Nanofluidic Membrane for Electrostatic Control of Drugs and Analytes Elution. *Pharmaceutics* **2020**, *12* (7), 679. <https://doi.org/10.3390/pharmaceutics12070679>.
4. Di Trani, N.; **Silvestri, A.**; Bruno, G.; Geninatti, T.; Chua, C. Y. X.; Gilbert, A.; Rizzo, G.; Filgueira, C. S.; Demarchi, D.; Grattoni, A. Remotely Controlled Nanofluidic Implantable Platform for Tunable Drug Delivery. *Lab Chip* **2019**, 10.1039.C9LC00394K. <https://doi.org/10.1039/C9LC00394K>
- 5.

---

# Appendix

## Article Permission Reprinting

3/29/2021

Gmail - Re: MDPI Contact Form: Usage of images and parts of the manuscript for my final thesis document - Antonia Silvestri



Antonia Silvestri <tonia.silvestri@gmail.com>

---

### Re: MDPI Contact Form: Usage of images and parts of the manuscript for my final thesis document - Antonia Silvestri

1 messaggio

support@mdpi.com <support@mdpi.com>

22 marzo 2021 10:48

A: Antonia Silvestri <antonia.silvestri@polito.it>

Dear Antonia,

Thank you for your email.

No special permission is required to reuse all or part of an article published by MDPI, including figures and tables. For articles published under an open access Creative Common CC BY license, any part of the article may be reused without permission, provided that the original article is clearly cited. Reuse of an article does not imply endorsement by the authors or MDPI.

Important Note: Some articles (especially Reviews) may contain figures, tables or text taken from other publications, for which MDPI does not hold the copyright or the right to re-license the published material. Please note that you should speak with the original copyright holder (usually the original publisher or authors), to enquire about whether or not this material can be re-used.

Please let us know if you have any further questions.

Kind regards,  
Stacy Luo  
MDPI Support Team

On 2021/3/19 18:20, Antonia Silvestri wrote:

To Whom it may concern,

I am Antonia Silvestri, a Ph.D. student in a double degree program at Politecnico di Torino (Italy) and Houston Methodist Research Institute (Texas). I previously published my work in a paper in "Pharmaceutics" titled "Silicon nanofluidic membrane for the electrostatic flow control of drugs and analytes" (<https://doi.org/10.3390/pharmaceutics12070679>). I am finalizing my thesis to conclude my Ph.D. degree in April 2021, and I need to use images and text for my final thesis document. I would kindly ask how to request permission to use those materials and insert them at the end of my thesis in the "Article Reprinting Permissions" section.

Looking forward to your answer, I send you my best regards. Antonia Silvestri

<https://mail.google.com/mail/u/0?ik=663a457636&view=pt&search=all&permthid=thread-f%3A1694925100925243671&siml=msg-f%3A16949251009...> 1/1

3/29/2021

Gmail - RE: Permission Request Form: Antonia Silvestri



Antonia Silvestri &lt;tonia.silvestri@gmail.com&gt;

**RE: Permission Request Form: Antonia Silvestri**

1 messaggio

**CONTRACTS-COPYRIGHT (shared)** <Contracts-Copyright@rsc.org>

19 marzo 2021 12:58

A: "antonia.silvestri@polito.it" &lt;antonia.silvestri@polito.it&gt;

Dear Antonia

The Royal Society of Chemistry (RSC) hereby grants permission for the use of your paper(s) specified below in the printed and microfilm version of your thesis. You may also make available the PDF version of your paper(s) that the RSC sent to the corresponding author(s) of your paper(s) upon publication of the paper(s) in the following ways: in your thesis via any website that your university may have for the deposition of theses, via your university's Intranet or via your own personal website. We are however unable to grant you permission to include the PDF version of the paper(s) on its own in your institutional repository. The Royal Society of Chemistry is a signatory to the STM Guidelines on Permissions (available on request).

Please note that if the material specified below or any part of it appears with credit or acknowledgement to a third party then you must also secure permission from that third party before reproducing that material.

Please ensure that the thesis includes the correct acknowledgement (see <http://rsc.li/permissions> for details) and a link is included to the paper on the Royal Society of Chemistry's website.

Please also ensure that your co-authors are aware that you are including the paper in your thesis.

Regards

Gill Cockhead

Contracts &amp; Copyright Executive

Gill Cockhead

Contracts &amp; Copyright Executive

Royal Society of Chemistry,

Thomas Graham House,

Science Park, Milton Road,

Cambridge, CB4 0WF, UK

**From:** antonia.silvestri@polito.it <antonia.silvestri@polito.it>**Sent:** 19 March 2021 09:52<https://mail.google.com/mail/u/0?ik=663a457636&view=pt&search=all&permthid=thread-f%3A169466147622720329&simpl=msg-f%3A16946614762...> 1/3

3/29/2021

Gmail - RE: Permission Request Form: Antonia Silvestri

**To:** CONTRACTS-COPYRIGHT (shared) <[Contracts-Copyright@rsc.org](mailto:Contracts-Copyright@rsc.org)>  
**Subject:** Permission Request Form: Antonia Silvestri

Name: Antonia Silvestri

Institution: Politecnico di Torino

Email: [antonia.silvestri@polito.it](mailto:antonia.silvestri@polito.it)

Address:

[CORSO DUCA DEGLI ABRUZZI, 24](#)

Department of Electronics and Telecommunications DET

Torino

10129

Italy

**I am preparing the following work for publication:**

Article/chapter title: Nanochannel membrane fabrication, In vitro release of drug, Electrochemical Characterization

Journal/book title: --

Editor/author(s): Antonia Silvestri

Publisher: Politecnico di Torino

Is this request for a thesis?: Yes

**I would very much appreciate your permission to use the following material:**

Journal/book title: Lab on a Chip

Editor/author(s): Nicola Di Trani, Antonia Silvestri, Antons Sivoz, Yu Wang, Donald R. Erm, Danilo Demarchi, Xuewu Liu,

Alessandro Grattoni

ISBN/DOL: <https://doi.org/10.1039/D0LC00121J>

Year of publication: 2020

Page(s): 17

Type of material: figures/images/parts of the paper related to the chapters previously mentioned

Figure/image number (if relevant):

**Any additional comments:**

Materials are used for the final Ph.D. thesis.

**Agree to terms:** I agree

This communication is from The Royal Society of Chemistry, a company incorporated in England by Royal Charter (registered number RC000524) and a charity registered in England and Wales (charity number 207890). Registered office: Burlington House, Piccadilly, London W1J 0BA. Telephone: +44 (0) 20 7437 8656.

The content of this communication (including any attachments) is confidential, and may be privileged or contain copyright material. It may not be relied upon or disclosed to any person other than the intended recipient(s) without the consent of The Royal Society of Chemistry. If you are not the intended recipient(s), please (1) notify us immediately by replying to this email, (2) delete all copies from your system, and (3) note that disclosure, distribution, copying or use of this communication is strictly prohibited.

Any advice given by The Royal Society of Chemistry has been carefully formulated but is based on the information available to it. The Royal Society of Chemistry cannot be held responsible for accuracy or completeness of this communication or any attachment. Any views or opinions presented in this email are solely those of the author and do not represent those of The Royal Society of Chemistry. The views expressed in this communication are personal to the sender and unless specifically stated, this e-mail does not constitute any part of an offer or contract. The Royal Society of Chemistry shall not be liable for any resulting damage or loss as a result of the use of this email and/or attachments, or for the consequences of any actions taken on the basis of the information provided. The Royal Society of Chemistry does not warrant that its emails or attachments are Virus-free; The Royal Society of Chemistry has taken reasonable precautions to ensure that no viruses are contained in this email, but does not accept any responsibility once this email has been transmitted. Please rely on your own screening of electronic communication.

<https://mail.google.com/mail/u/0/?ik=663a457636&view=pt&search=all&permthid=thread-f%3A1694661476227220329&simpl=msg-f%3A16946614762...> 2/3

3/29/2021

Gmail - RE: Permission Request Form: Antonia Silvestri

More information on The Royal Society of Chemistry can be found on our website: [www.rsc.org](http://www.rsc.org)

<https://mail.google.com/mail/u/0?ik=663a457636&view=pt&search=all&permthid=thread-f%3A1694661476227220329&simpl=msg-f%3A16946614762...> 3/3